Spectrum and Conversion Efficiency Measurements of Suprathermal Electrons from Relativistic Laser Plasma Interactions

MASSACHUSETTS INSTITUTE
OF TECHNOLOGY
AUG 0 4 2009
LIBRARIES

by

Cliff D Chen

B.S., Cornell University (2001)
M.Eng., Cornell University (2002)

Submitted to the Department of Physics
in partial fulfillment of the requirements for the degree of
Doctor of Philosophy in Physics
at the
MASSACHUSETTS INSTITUTE OF TECHNOLOGY
June 2009

© Massachusetts Institute of Technology 2009. All rights reserved.

Author ....
Department of Physics
May 20, 2009

Certified by..
Miklos Porkolab
Professor of Physics
Director of the Plasma Science & Fusion Center
Thesis Supervisor

Certified by... ....
Andrew Mackinnon
Group Leader for Fast Ignition Experiements
Lawrence Livermore National Laboratory
Thesis Co-Supervisor

Accepted by... ...
Thomas Greytak
Associate Department Head for Education

ARCHIVES

Spectrum and Conversion Efficiency Measurements of Suprathermal Electrons from Relativistic Laser Plasma Interactions

by

Cliff D Chen

Submitted to the Department of Physics
on May 20, 2009, in partial fulfillment of the
requirements for the degree of
Doctor of Philosophy in Physics

Abstract

Fast Ignition is an alternative scheme for Inertial Confinement Fusion (ICF) that uses a petawatt laser to ignite a hot spot in precompressed fuel. The laser delivers its energy into relativistic electrons at the critical surface of the blowoff plasma. These electrons must propagate to the fuel core and deliver their energy to a hot spot. Electrons of energies between 1 and 3 MeV have the appropriate range for efficient energy deposition. This thesis experimentally explores the coupling efficiency and spectrum of the laser produced electrons. The experiments make use of Bremsstrahlung and K-shell emission from planar foil targets to infer the electron distribution produced in the laser-plasma interaction.

This thesis describes the development of a filter stack Bremsstrahlung spectrometer with differential sensitivity up to 500 keV. The spectrometer is used with a single photon counting camera for measuring Kα emission in experiments on the Titan laser (1.06 μm, 150 J, 0.7 ps) at Lawrence Livermore National Laboratories. The Bremsstrahlung and K-shell emission from 1 mm^3 planar targets irradiated with intensities from 3x10^{18}-8x10^{19} W/cm^2 were measured. The target emission is modeled using the Monte Carlo code `Integrated Tiger Series 3.0` in order to unfold the electron spectrum from the x-ray measurements. Conversion efficiencies into 1-3 MeV electrons of 12-28% were inferred, representing 35-60% total conversion efficiencies.

Laser diagnostics were used to characterize the laser focal spot and pulselength in order to provide proper comparisons to intensity scaling laws. Comparisons to scaling laws show that the electron spectrum is colder than the laser ponderomotive potential derived from the peak intensity. For intensities above 2×10^{19} W/cm^2, the spectrum is slightly hotter than widely used empirical scalings. More accurate comparisons to ponderomotive scaling using a synthetic energy spectra generated from the intensity distribution of the focal spot imply slope temperatures less than the ponderomotive potential, but is within the range of a correction due to the neglect of resistive transport effects. The impact of resistive transport effects were estimated using an analytic transport model and may lead to higher total conversion efficiencies but lower conversion efficiencies into 1-3 MeV electrons.

Thesis Supervisor: Miklos Porkolab
Title: Professor of Physics
Director of the Plasma Science & Fusion Center

Thesis Co-Supervisor: Andrew Mackinnon
Title: Group Leader for Fast Ignition Experiements
Lawrence Livermore National Laboratory

Acknowledgements

I would like to thank Andy Mackinnon, Mike Key, Prav Patel, and Miklos Porkolab for their direction over these past few years. Their technical guidance has been invaluable in advancing my research and their critiques have helped sharpen my physical intuition and my scientific communication skills.

I would also like to thank Roger Van Maren, who engineered the x-ray spectrometer and made all the other bits and pieces of equipment I have needed over the years. Rob Costa, Rich Combs, Gary Freeze, Chuck Cadwalader, and the other Jupiter Laser Facility staff provided excellent support during my experiments. Bill Carl and Frank Balgos of the Radiation Calorimetry Laboratory helped me set up my spectrometer calibrations and went out of their way to fit me into their schedule.

The High Energy Density Physics group at MIT supported me for the first three years of my graduate education and provided my initial training in the field. They provided me a background framework for my current research. The administrative staff at the PSFC were extremely helpful in dealing with all the subcontract issues between MIT and LLNL.

I have had many useful discussions with Scott Wilks, Max Tabak, Andreas Kemp, Tom Phillips, Andrew MacPhee, and Daniel Hey, and I appreciate their generosity in taking their time to brainstorm ideas and explain concepts.

The experimental team made research fun. Andrew MacPhee, Tammy Ma, Tony Link, Kramer Akli, Sebastien Le Pape, Dustin Offerman, Jim King, Linn Van Woerkom, Vladimir Ovchinnikov, Teresa Bartal, Sophia Chen, and all our other collaborators at UCSD, OSU, General Atomics, and the University of Alberta formed an excellent team that made our experiments successful and enjoyable.

The diligence of my carpool-mate and office-mate Tammy Ma guilted me into staying on task, and our daily discussions were instrumental in helping me formulate my thoughts on my research and future career direction. She has also saved me more than \$2000 on gas and reduced my CO_2 emissions by about 6 tons.

I would like to thank my wife Patricia for her love, patience, and encouragement over the course of my entire degree program. She has never known me as anything but a graduate student, and it is exciting to move into a new phase of life together. I would also like to acknowledge my family and friends, without whose support I would never have had the endurance to make it through these past years.

Contents

List of Figures

List of Tables

Chapter 1

1.1 Fusion Basics

When two nuclei combine to form a heavier one, the strong nuclear force binds the nucleons together into a lower potential state, releasing energy in the process. This energy comes from the mass of the original nucleons, since the mass of the heavier nucleus is smaller than the sum of its constituent parts. The energy released is calculated from Einstein's famous relationship $E = mc^2$. The binding energy determines whether nuclear reactions are endothermic or exothermic. The binding energy per nucleon is plotted in Figure 1-1. The lowest binding energies are for hydrogen and its isotopes, deuterium (D) and tritium (T), and for ^{3}He. When these nuclei fuse into heavier elements, energy equivalent to the difference in the binding energy is released. The binding energy curve peaks at iron, and drops off for the heavier elements. Splitting the heavy elements like uranium and plutonium into moderate Z elements also releases energy through nuclear fission. Nuclear fission is the energy mechanism in all nuclear reactors today.

Since the isotopes of hydrogen and ^{3}He have the lowest binding energies per nucleon, fusion efforts in the laboratory concentrate on reactions involving these elements. These reactions are shown in Table 1.1. The energy from the reactions is released in the kinetic energy of the resultant particles. While the fusion reactions are strongly exothermic, there is a significant amount of activation energy involved. The strong nuclear force is a short range force acting with a range on order of the two nuclear radii, which can be approximated by $r_n \approx 1.44 \times 10^{-13} \left(A_1^{1/3} + A_2^{1/3}\right)$ cm

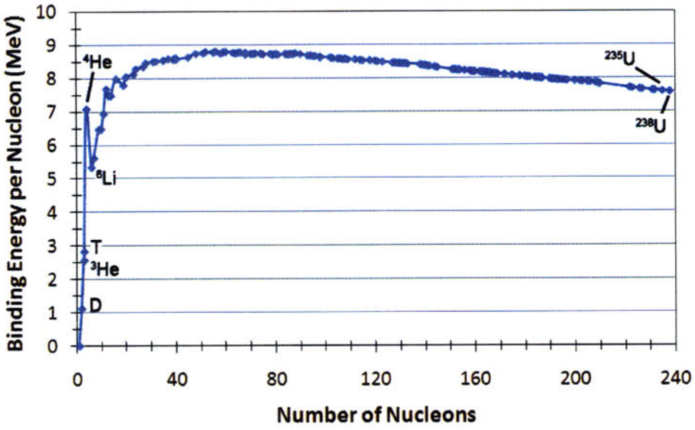

Figure 1-1: Binding Energy per nucleon.

$$
\begin{array}{llcccccl}
\mathrm{D+T} & \longrightarrow & \alpha & + & \mathrm{n} & + & 17.6\ \mathrm{MeV} \\
\mathrm{D+D} & \longrightarrow\left\{\begin{array}{l} \\ \\ \end{array}\right. & \begin{array}{c}\mathrm{T} \\ {}^3\mathrm{He}\end{array} & \begin{array}{c}+ \\ +\end{array} & \begin{array}{c}\mathrm{p} \\ \mathrm{n}\end{array} & \begin{array}{c}+ \\ +\end{array} & \begin{array}{r}4.1\ \mathrm{MeV} \\ 3.2\ \mathrm{MeV}\end{array} \\
\mathrm{D+{}^3He} & \longrightarrow & \alpha & + & \mathrm{p} & + & 18.3\ \mathrm{MeV}
\end{array}
$$

Table 1.1: Common reactions for laboratory fusion

where A_1 and A_2 are the atomic masses of the two nuclei in atomic mass units. Since the two nuclei are positively charged, they must have sufficient kinetic energy to overcome the coulomb repulsion. For the deuterium-tritium reaction, the repulsion energy is approximately 370 keV. Fortunately, quantum tunneling allows appreciable fusion reactions to occur at lower energies. The total cross section can be written as

$$\sigma\left(\epsilon\right) = \frac{S\left(\epsilon\right)}{\epsilon} exp\left(-\sqrt{\epsilon_G/\epsilon}\right), \tag{1.1}$$

where ϵ is the center of mass kinetic energy, $S\left(\epsilon\right)$ is the astrophysical S factor which is a weak function of energy, and ϵ_G is the Gamow energy [9] given by $\epsilon_G = \left(\pi\alpha_f Z_1 Z_2\right)^2 2m_r c^2$ where α_f is the fine structure constant and m_r is the reduced mass. For the DT reaction, the Gamow energy is about 1.2 MeV. The total reaction rate is calculated from the cross section by integrating over distribution functions for the ion energies. The reaction rate is given by

$$RR = \int_{\mathbf{v}_a} \int_{\mathbf{v}_b} \sigma\left(|\mathbf{v}_a - \mathbf{v}_b|\right) |\mathbf{v}_a - \mathbf{v}_b| \, N_a F_a\left(\mathbf{v}_a\right) N_b F_b\left(\mathbf{v}_b\right) \, d^3 v_a \, d^3 v_b. \tag{1.2}$$

This equation is just the average of σv over a distribution function, usually taken to be thermal Maxwellian distribution. The reaction rate can then be written as

$$RR = N_a N_b \langle \sigma v \rangle, \tag{1.3}$$

where σv is a function of the ion temperature, taken as equivalent for the two ion species. The fusion cross section is commonly tabulated for σv as a function of temperature for the different fusion reactions. The σv parameter is plotted for D-T, D-D, and D-^{3}He in Figure 1-2 and is taken from *Principles of Fusion Energy* [10] and originally tabulated by J. Rand McNally, Jr. [11]. The reactivity of the

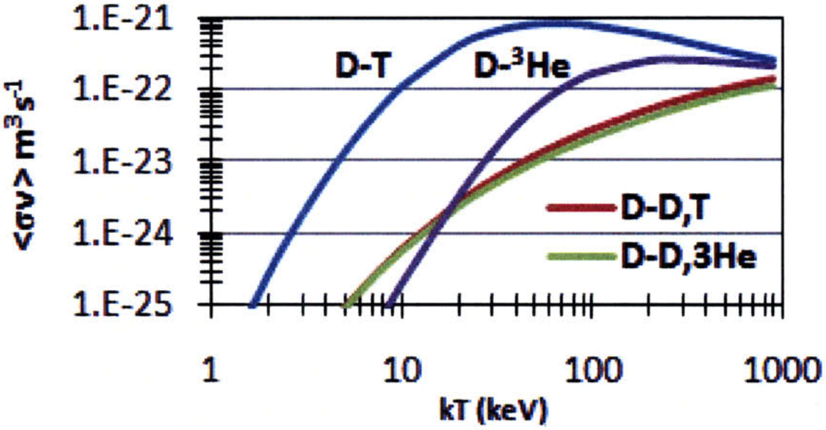

Figure 1-2: $\langle \sigma v \rangle$ parameter for different fusion reactions. The onset temperature is the lowest and cross section the highest for D-T, making it the reaction of choice for first generation fusion reactors.

D-T reaction is about an order of magnitude higher than the other reactions. The threshold temperature for D-T is also roughly 5-10 keV, compared to 10's of keV for the other reactions. These factors make D-T the reaction of choice for first generation fusion reactors.

1.2 Confinement and Energy Balance

Heating the fuel to keV temperatures requires novel ways of confining the fuel for sufficient time for fusion reactions to take place. There are two primary techniques for fusion plasma confinement, magnetic and inertial. In the Magnetic Confinement Fusion (MCF) scheme, charged particles are constrained to travel along magnetic field lines. Current designs for magnetic confinement fusion demonstration reactors such as the ITER tokamak use a closed field geometry, in this case a toroidal field where the magnetic field lines form rings around a donut-shaped reactor. In such a field structure the particles make orbits around the reactor and remain confined. As the particles undergo collisions, however, they scatter across the field lines and eventually escape, resulting in a finite confinement time for the plasma.

The minimum confinement time required for a fusion plasma is defined by the reactor energetics and power balance. The confinement time must be long enough that enough fusion reactions occur to replace the input heating energy and energy lost through other loss channels. These power balance equations were originally published by Lawson [12], and the constraints are known as Lawson or Lawson-type criteria. A requirement on the confinement time can be derived from the steady state power balance of a burning plasma, without accounting for the technology of energy delivery and energy capture. A steady state burning fusion plasma is heated by α-particle energy deposition from the D-T reaction as well as any auxiliary input power. It cools due to radiative Bremsstrahlung losses and diffusive losses from the finite confinement time of the plasma. The power balance is represented by

$$P_{aux} + P_{\alpha} = P_{brems} + P_{diffusion}. \tag{1.4}$$

The α deposition is given by the fusion reaction rate times the energy in the α particle, with P_{α}=20% $\left(\frac{N_i}{2}\right)^2 \langle \sigma v \rangle Q_{DT} V$ since the α particle contains about 20% of the reaction energy (Q_{DT} is the 17.6 MeV released in the reaction). The diffusive loss is expressed as the energy contained in the plasma divided by the confinement time, $P_{dif} = \frac{3N_i k_b T}{\tau_E} V$. The Bremsstrahlung power loss can be estimated by integrating over the Bremsstrahlung cross section and can be approximated as [13] $P_B = C_b N_e^2 T^{1/2} V$, where $C_b = 5.34 \times 10^{-24}$ erg cm^3 s^{-1} keV$^{-1/2}$. In addition, writing the reactor Q as $Q = \frac{P_{fusion}}{P_{aux}}$, the power balance can cast in the form

$$n\tau_E = \frac{3k_bT}{\frac{1}{4}\left[(1/Q) + (1/5)\right] Q_{DT}\langle\sigma v\rangle - C_b T^{1/2}}. \tag{1.5}$$

This equation is known as the nτ condition and sets the minimum requirement on the confinement time of the reactor. For steady-state operation the auxiliary input power is zero and Q=inf. A 20 keV temperature then sets the nτ_E requirement at $n\tau_E \approx 2 \times 10^{14}$ cm^{-3} s.

1.3 ICF Overview

MCF relies on the relatively long confinement ($\approx 1sec$) of a low density plasma ($\approx 10^{14}$ cm^{-3}). In contrast, Inertial Confinement Fusion (ICF) involves high densities and short confinement times to achieve energy gain. In the ICF scheme, a D-T fuel capsule spherically compressed to high density is confined for only as long as it takes for the compression to stagnate and the mass to accelerate outwards, on the order of a few ns. The density must be sufficiently high that for ns confinement times, the number of fusion reactions burns a significant fraction of the D-T fuel. A Lawson-like criteria can also be derived for the energy balance of the ICF fuel capsule. The reaction rate is a function of the fuel density and reactivity

$$\frac{dn}{dt} = -\frac{n^2}{2}\langle\sigma v\rangle, \tag{1.6}$$

assuming an initial 50-50 DT mixture. Integrating out to a confinement time T_c, the burn fraction of the fuel is given by

$$f_b = \frac{\frac{T_c}{2\tau_R}}{1 + \frac{T_c}{2\tau_R}}, \tag{1.7}$$

where $\tau_R = \frac{1}{N\langle\sigma v\rangle}$ is the initial mean time between fusion reactions. The effective confinement time T_c is about 1/4 the radius of the capsule divided by the sound speed $c_s = \sqrt{2k_BT/m_{avg}}$. Equation 1.7 can then be written as

$$f_b = \frac{\rho R}{H_B + \rho R}, \tag{1.8}$$

where $H_B = 8c_s m_{avg}/\langle\sigma v\rangle$ is the burn parameter which is between 6 and 9 g/cm^2 for fusion temperatures. For a reasonable fuel burn fraction of 1/3, the requirement on ρR is about 3 g/cm^2.

The energy released in the burn of a fusion capsule is substantial. The 30% burnup of a solid density D-T capsule with ρR=3 g/cm^2 results in the release of energy equivalent to 500 tons of TNT from 18 g of fuel. In order to maintain a functioning reactor, the total fuel mass must be limited to 10 mg. With the ρR constraint, this sets the required fuel density at 300-1000× solid density. These high densities can be achieved through spherical implosions. This idea was first published by Nuckolls et al. in 1972 [14] although it was studied a decade earlier in the classified realm. The spherical implosion design uses a driver, typically a laser, to ablate a surface layer on the fuel capsule. The ablative material blows off and the inner fuel is imploded via the rocket reaction.

The coupling of the driver to the fuel is expected to be on the order of 10%. The energy required for volumetric heating of the fuel to 10 keV limits energy gain to about 10, too low for energy breakeven. To achieve higher energy gain, only a portion of fuel is directly heated, while the rest is heated through α particle energy deposition from the fusion reactions.

The conventional design for ICF is called "Hot Spot Ignition." This scheme is shown schematically in Figure 1-3. The fuel capsule is irradiated with a driver, which can be a laser, x-rays, or ion beams. The outer surface is ablated by the driver and the shell is launched inward via the rocket reaction. Compression via a single shock is limited to 4-6×, with stronger shocks serving only to raise the isentrope (preheating the fuel), thereby making it harder to compress. A series of shocks launched by shaping the driver pulse is therefore used to achieve high compression while keeping the fuel at a lower isentrope. The shocks are also carefully timed to converge simultaneously on the inner DT gas. The gas heats up from the compression, the shock coalescence, and the deposition of fusion α particle energy. The internal pressure increases, causing the shell implosion to stagnate. At stagnation the capsule is in pressure equilibrium (isobaric compression), and has a stagnation time on the order of a few hundred ps. The inner DT gas reaches ignition temperatures and fusion α particles deposit their energy in the high density DT shell, resulting in a propagating burn wave that consumes the fuel capsule.

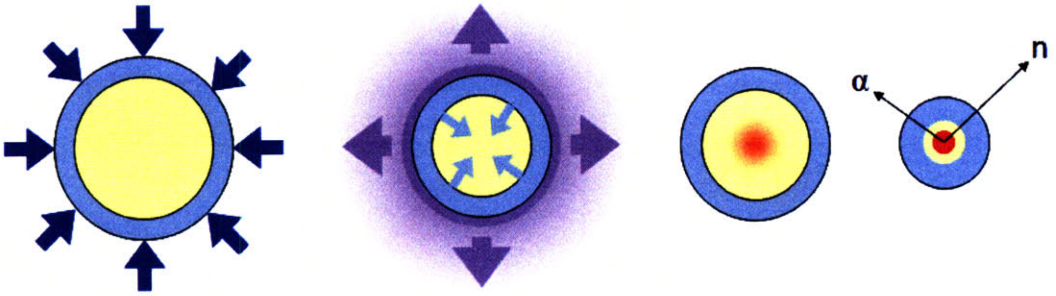

Figure 1-3: The fuel capsule is irradiated with a driver. The outer surface material ablates, launching the shell inwards via the rocket reaction. A series of shocks converges on the inner DT gas, heating it up and raising the pressure inside the capsule. The shell is decelerated by the internal pressure and eventually stagnates as the DT gas reaches ignition temperatures. The resulting fusion α particles deposit their energy in the shell, triggering a chain reaction that burns up the fuel.

The main challenge in hot spot ignition is the hydrodynamic stability of the implosion. As the shell implodes, the low density plasma at the outer surface is accelerated against the high density shell, triggering the Rayleigh-Taylor instability on the external surface which can lead to shell breakup. The instability is seeded by the capsule surface roughness and by imprinting of the driver nonuniformity on the shell. As the shell is decelerated by the internal pressure buildup, it experiences the Rayleigh Taylor instability on the interior surface, this time seeded by the inner D-T ice roughness. There are two dangers in the deceleration phase. The shell can again break up.

In addition, the instability can result in mixing of the cold DT ice with the heated gas, quenching the fusion burn. These instabilities are depicted in Figure 1-4, taken from graphic artists at the Laboratory for Laser Energetics (LLE) in Rochester, NY. Significant hydrodynamic simulation work has gone into setting constraints on the surface roughness and beam uniformity. Current target designs use "indirect-drive," which contain the fuel capsule in a gold can called a "hohlraum." The hohlraum is illuminated by intense lasers, producing a uniform bath of x-rays which ablate the shell surface. The reduced coupling efficiency of the driver to the target is traded for increased implosion uniformity which leads to better hydrodynamic stability.

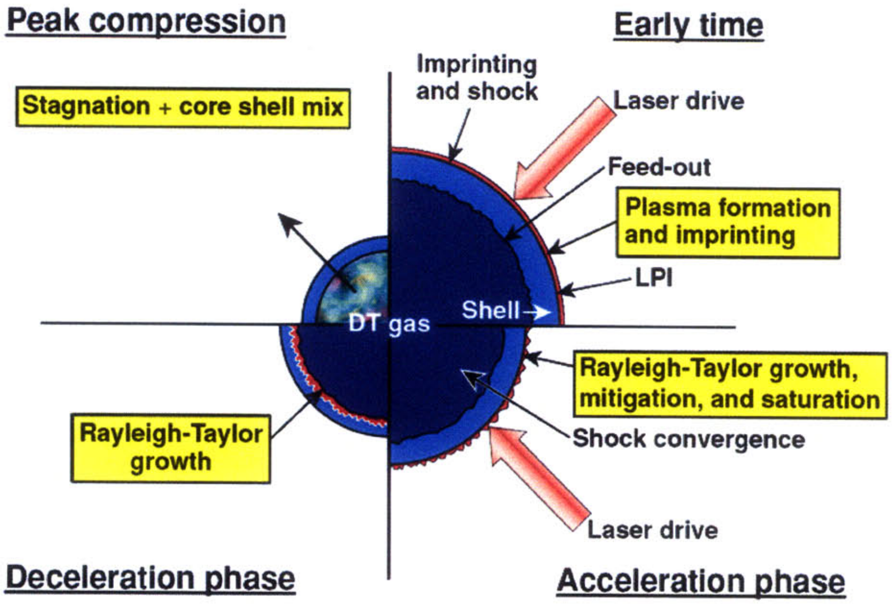

Figure 1-4: The Rayleigh-Taylor instability occurs at the outer shell surface in the acceleration phase and at the inner surface in the deceleration phase. The instability can lead to shell breakup and quenching of the fusion burn via mixing of the cold shell material and the heated DT gas.

The recent completion of the National Ignition Facility [15] will allow these targets to be tested at ignition scale conditions. It is hoped that ICF will be able to demonstrate ignition on the National Ignition Facility in the next couple of years.

1.4 Fast Ignition

Fast Ignition is an alternative scheme for ICF that decouples the fuel compression and ignition phases by using a secondary beam to spark a hot spot in the precompressed fuel. It was first proposed by Tabak et al. [16] in 1994, a few years after the development of Chirped Pulse Amplification lasers [17] that made possible the delivery of large amounts of energy in timescales short enough for fusion confinement. The Fast Ignition concept promises higher gains, lower sensitivity to hydrodynamic instabilities, and reduced driver energy when compared to conventional hot spot ICF. This is achieved by using a short-pulse laser to ignite a hot spot in a pre-compressed fusion capsule. The laser interacts with the plasma near the critical density surface, generating hot electrons that propagate into the core to heat the hot spot.

The main challenge in fast ignition is how to get the short pulse laser as close to the dense plasma as possible in order to maximize coupling. The original concept is known as "hole-boring," which delivers energy to the core using two picosecond-scale petawatt lasers: the ponderomotive force of the first laser creates a channel through the plasma around the compressed fuel, and the second laser propagates through the channel and deposits its energy into hot electrons near the core, igniting a hot spot. While the hole-boring concept is still being studied, the current mainline approach to fast ignition instead uses a high Z cone to keep open a channel through the blowoff plasma. In this "cone-guided" fast ignition concept [18], [19], [20], a single petawatt laser deposits its energy at the cone tip. The high Z cone then reduces the distance the electrons have to travel to reach the core. The work in this thesis is primarily focused on the cone-guided fast ignition concept. Other designs involving conversion of the petawatt energy into protons [21] that transport ballistically to heat the core are also being studied.

The conventional ICF and Fast Ignition concepts are shown schematically in Figure 1-5. In Conventional ICF, a cold, high density outer shell surrounds a hot, low density plasma which ignites and heats the shell. In Fast Ignition, the fuel is uniformly compressed to moderate densities (isochoric compression) and ignition separately trig-

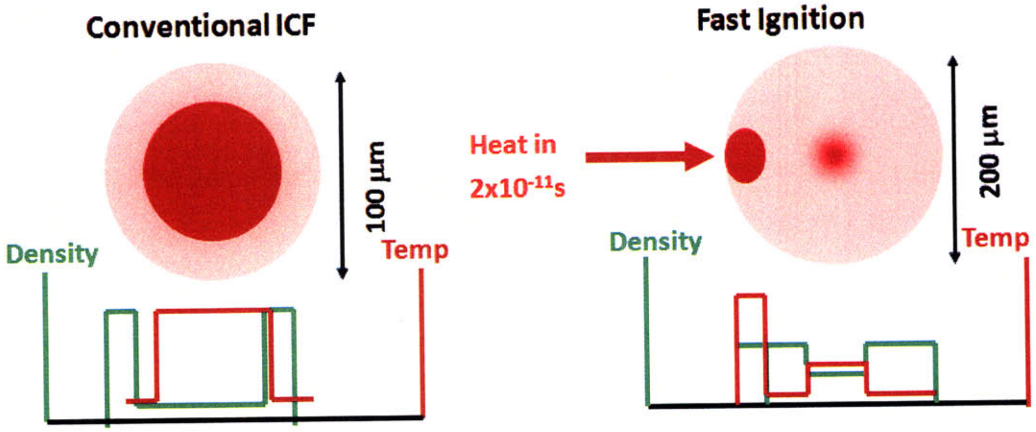

Figure 1-5: The compressed target in Conventional ICF consists of a cold, high density outer shell surroundeing a hot, low density plasma which triggers ignition. In Fast Ignition, the fuel is isochorically compressed to moderately high density with no hot spot. The hot spot is generated by a picosecond-scale secondary driver beam that ignites the target.

gered by a picosecond-scale petawatt laser. Since the compression and ignition phases are decoupled, the requirements on the compression driver are relaxed. The compression uniformity is less important since no hydrodynamic hot spot is required, and the lower density fuel allows for lower driver energies, which also reduces the acceleration that drives the hydrodynamic instabilities.

Alternatively, the success of Fast Ignition is primarily dependent on the coupling of the short-pulse laser energy to the hot spot. Simulations [22] have found that to achieve ignition at 300 g/cc, 18 kJ of energy must be deposited in a 40 μm diameter hot spot in 20 ps, requiring laser intensities of 2-3x10^{20} W/cm^2. This energy requirement is higher than the 3 kJ required to heat a 40 μm, 300 g/cc hot spot because of pdV losses during the heating phase in this isochoric configuration.

The coupling of the laser to the hot spot can be broken down into 3 components: the coupling of the laser into relativistic electrons ($\eta_{L \to e^-}$), the transport efficiency of the electrons to the core, which depends on the divergence angle and collimation effects (η_{trans}), and the deposition of the electron energy in the hot spot, which is a function of the electron energy spectrum ($\eta_{deposition}$). This is shown schematically for the cone guided approach in Figure 1-6. For a 40 μm diameter hot spot, electrons of 1-

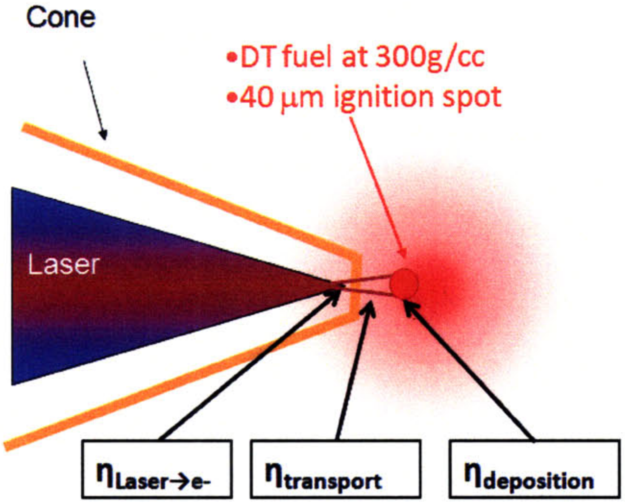

Figure 1-6: The success of fast ignition depends on the coupling of the laser to the hot spot, which can be broken down into the conversion efficiency to relativistic electrons, the transport coupling to the core, and the deposition rate of electron energy in the hot spot.

3 MeV have the ideal range to couple efficiently, making the conversion efficiency to 1-3 MeV electrons a critical parameter for fast ignition. For Fast Ignition laser intensities, the primary acceleration mechanism for the electrons is via the jxB force, which will be discussed in Chapter 2. The temperature of the electron spectrum generated via the jxB acceleration mechanism is usually taken to scale with the ponderomotive potential of the laser [23]. For intensities of 2-3x10^{20} W/cm^2, however, this results in temperatures of 6-8 MeV, reducing the deposition efficiency because stopping in the hot spot is less efficient, and driving up the driver requirements. Recent modeling suggests that the mean energy may be colder than ponderomotive scaling due to steepening of the plasma density profile within the cone [24], [8], [25].

All three aspects of the coupling efficiency are active areas of research within the fast ignition community. Significant theoretical and experimental work has been done on evaluating the electron source, although large uncertainties still remain. These efforts will be discussed further in the following chapter. The transport efficiency to the core has been studied computationally [26], [27] and is starting to be examined experimentally [28] with the advent of high energy short-pulse lasers such as OMEGA

EP that allow electron transport to be studied in the appropriate physical regime. Electron stopping powers in fast ignition plasmas have been studied analytically by a number of different groups [29], [30], [31] to better understand the deposition efficiency. The deposition efficiency is dependent on the spectrum of the electron source, thereby linking this efficiency to the driver conversion efficiency in a coupled way.

1.5 Thesis Overview

This thesis describes a series of experiments that study the electron source produced at the cone tip, specifically the conversion efficiency of the laser into fast ignition relevant electrons in the 1-3 MeV range. These experiments involve measurements of Bremsstrahlung and k-shell emission from planar foils irradiated with intensities from 3×10^{18} to 9×10^{19} W/cm^2. The experiments were performed with the TITAN laser [32] at the Jupiter Laser Facility at Lawrence Livermore National Laboratory (LLNL).

Chapter 2 of the thesis describes the physics of the absorption mechanisms and the prior work done on conversion efficiency and spectral measurements. It also provides a background of the physics relevant to the diagnostics and computational models used in the analysis. Chapter 3 provides an overview of the TITAN laser system, laser diagnostics, and Bremsstrahlung and single photon counting spectrometers for measurements of the Bremsstrahlung and k-shell emission. The calibration procedure and calibration data for the x-ray diagnostics is also presented. Chapter 4 gives an overview of the experiment, presents the data, and describes the analysis and modeling procedures used in the interpretation of the data. The results are compared to analytic scaling models and discussed in the context of fast ignition. Chapter 5 summarizes the conclusions and presents ideas for future diagnostics and experiments that evolve from this work.

1.6 Role of the Author

Short-pulse laser experiments require a collaborative team effort for successful execution. This section details the specific role of the author in the work described in this thesis.

The design of the Bremsstrahlung spectrometer described in Chapter 3 was developed by the author over a series of three experimental campaigns on the Titan laser in April 2007, August 2007, and January 2008 and one campaign on the Callisto laser in May-June 2007. The CAD drawings and construction of spectrometer was done by Roger Van Maren of the Jupiter Laser Facility at LLNL. The final assembly of the filters and and dosimeters required nearly 100 man-hours and was done by the author with generous assistance from the other graduate students on the experimental team. The spectrometer calibration shown in Chapter 3 was by the author at the HEX facility at NSTec (Livermore, CA) and at the Radiation Calorimetry Laboratory at LLNL (Livermore, CA) with assistance from the staff of the respective facilities.

The single photon counting cameras described in this thesis was borrowed from the High Energy Radiography group at LLNL. The calibration for this camera was done by Brian Maddox of the radiography group. The author also fielded other cameras for single photon counting on other experiments. The author worked with Brian Maddox in calibrating these other cameras and to verify the calibration of the one discussed in this work. The author also calibrated these cameras at the MANSEN facility at NSTec, with assistance from the facility staff. The single photon counting analysis algorithms are from preexisting literature. These algorithms were studied and evaluated both independently and collaboratively with Brian Maddox. The author developed a general use software package for analyzing the single hit data.

On the experiments the author was responsible for setting up and fielding the Bremsstrahlung spectrometer and single photon counting cameras, as well as for target alignment and positioning. The author also assisted with the laser alignment focusing and focal spot imaging on a some of the Titan experiments. The equivalent plane monitor described in Chapter 3 was fielded and analyzed by Daniel Hey of

LLNL. The prepulse measurements were done by Sebastien Le Pape from LLNL and Ying Tsui from the University of Alberta. Ying Tsui also performed the autocorrelator measurements of the laser pulselength.

The `Integrated Tiger Series 3.0` simulations described in Chapters 3 and 4 were done by the author using the code package. All of the post-processing and analysis development was also performed by the author. The resistive transport calculations described in Chapter 4 were developed by the author based on models in the literature. The higher energy Bremsstrahlung spectrometer alluded to in Chapter 5 was also designed by the author and Roger Van Maren. The author also fielded the higher energy Bremsstrahlung spectrometer on a June-August 2008 Titan experimental campaign. The Compton spectrometer discussed in Chapter 5 was conceptualized together with Max Tabak of LLNL and the feasibility study was performed by the author. The electron spectrometer used in the Compton spectrometer belongs to Hui Chen (LLNL) and she provided the energy resolution data based on the field map trajectory calculations.

Chapter 2

The physics of laser plasma interactions define the electron source generated at the tip of a fast ignition cone. Under real experimental conditions, there is a mixture of absorption mechanisms which depends on the local laser intensity, the plasma interaction region, and the laser incidence angle. These parameters are complicated by self-focusing of the laser in the subcritical plasma, steepening of the preformed plasma through the ponderomotive pressure of the laser, and a 3-D plasma profile which obscures the definition of the incidence angle. The exact physical mechanisms of absorption for various laser conditions are still a matter of ongoing research. The primary mechanism relevant under fast ignition conditions is the *Relativistic Ponderomotive (jxB)* force. This is described in detail in this chapter. Other mechanisms, including *Resonance Absorption* and *Vacuum Heating* are also briefly discussed.

Once the electrons are generated at the surface, they lose energy in the target through collisional, resistive, and radiative mechanisms. In this work, collisional and radiative energy losses are modeled with the cold matter Monte Carlo transport code `Integrated Tiger Series 3.0 (ITS 3.0)` [33], under the assumption that for large targets, cold matter is a reasonable approximation to the heated material during the hot electron transport time. The electron energy loss mechanisms contained in `ITS 3.0` are described in this chapter. The electrons also produce k-shell line emission and Bremsstrahlung through collisions with inner shell electrons and scattering off nuclei, respectively. The x-ray products are measured in these experiments and used to infer details of the electron source. The physics of k-shell emission and Bremsstrahlung production are described in this chapter. Additionally, since the x-ray detectors depend on various x-ray absorption mechanisms, the photoelectric effect, Compton scattering, and pair production interaction mechanisms are also briefly discussed.

The large electron currents in these experiments lead to electric and magnetic fields that affect the interparticle interactions. These collective effects cannot be modeled using Monte Carlo techniques and in this thesis are treated as a perturbation to the analysis and simulations presented. Discussion of collective effects are deferred to chapter 4, after the presentation of the experimental data.

The last part of this chapter provides a backdrop to this thesis by describing the techniques and key experiments that shape current understanding of the hot electron spectra and conversion efficiencies in fast ignition regimes.

2.1 Laser plasma interactions

The propagation of a high frequency electromagnetic wave in a plasma is modified from its vacuum propagation by the presence of the free electrons. The plasma electrons have a characteristic frequency called the *plasma frequency*, which is the oscillation frequency of the electrons when they are displaced from the background ions and restored by the resultant electric field. The plasma frequency is solely a function of electron density and is given by $\omega_{pe} = \left(\frac{4\pi ne^2}{m_e}\right)^{1/2}$.

In a plasma, the light wave propagates with the well known dispersion relation

$$k^2c^2 = \omega_0^2 - \omega_{pe}^2. \tag{2.1}$$

The dispersion relation is altered from its free space value by the presence of the ω_{pe} term. For frequencies much greater than the plasma frequency, the light wave propagates as if in free space. As the wave reaches densities where the plasma frequency approaches the laser frequency, the plasma electrons begin to screen out the wave, reducing the wave number. When these two frequencies are equal the wave number drops to zero and the wave can no longer propagate. The electron density at which this occurs is called the *critical density (n_c)* and the density contour is called the *critical surface.* For densities beyond n_c the wave vector is imaginary and the wave is exponentially attenuated. The skin depth is then given by

$$\delta = \left[Im\,(k)\right]^{-1} = \frac{c}{\left(\omega_{pe}^2 - \omega^2\right)^{1/2}}, \tag{2.2}$$

and depends on the density profile of the plasma. At the critical surface the electrons can respond quickly enough to screen out and reflect the light wave. For 1.06 μm laser light the critical density is 1.1×10^{21} cm^{-3}, about 1/1000 solid density. If the laser light is intense enough for the electron motion to be relativistic, the light wave can propagate up to γn_c due to the increased inertia of the electrons. This density contour is called the *relativistic critical surface.*

The majority of the laser light is absorbed at the relativistic critical surface. This is for two reasons. First, the densities are higher at the critical surface so more electrons are accelerated. Second, most of the absorption mechanisms involve oscillations of electrons in the laser field. In order for acceleration to occur, electrons must gain energy and then dephase from the wave. This occurs when the electrons are pushed across the critical surface. Beyond the critical surface the wave field is dampened and the electrons are launched in the forward direction.

For normal incidence or s-polarized laser intensities $> 10^{18}$ W/cm^2, the primary absorption mechanism is the relativistic ponderomotive force [23], [34], also called $j \times B$ force because of the importance of the laser B field at relativistic intensities for redirecting the electron currents. A simple picture the motion of an electron in a laser field is first described, followed by a discussion of the actual physical mechanism for the $j \times B$ force. In the field of an EM wave, the electrons oscillate transversely along the direction of the electric field vector at the frequency of the field. This motion is called the quiver velocity of the electrons and is given by [34]

$$\frac{p_{osc}}{m_e c} = \frac{\gamma v_{osc}}{c} = \frac{eE_0}{m_e c \omega_0} = \sqrt{\frac{I \lambda_{\mu m}^2}{1.37 \times 10^{18}}}, \tag{2.3}$$

where p_{osc}, v_{osc}, and E_0 are peak values and I is in units of W/cm^2. The B field of the wave gives the motion a longitudinal component, which is small if the motion is non-relativistic. The electrons end up making a figure eight motion, superimposed on drifts in the forward and transverse directions, depending on the initial phase of the wave. The electrons thus oscillate transversely at 1ω and longitudinally at 2ω. If the wave is intense and the electron motion is relativistic, this forward push from the B field is significant and the electrons gain a longitudinal velocity on order of the speed of light.

The energy of these electrons can be derived in the following way [35]. Starting from the relativistic equation of motion for a fluid element

$$\frac{\partial \vec{p}}{\partial t} + \vec{v} \cdot \nabla \vec{p} = -e \left[\vec{E} + \frac{\vec{v} \times \vec{B}}{c} \right]. \tag{2.4}$$

The field components can be replaced by their vector potential definitions. Additionally, substituting the momentum vector for the velocity we obtain

$$\frac{\partial \vec{p}}{\partial t} + \frac{\vec{p} \cdot \nabla \vec{p}}{\gamma m} = -e \left[-\frac{1}{c} \frac{\partial \vec{A}}{\partial t} - \nabla \phi + \frac{\vec{p} \times \nabla \times \vec{A}}{\gamma m c} \right]. \tag{2.5}$$

For a 1-D plane wave propagating in the $\hat{z}$ direction, the momentum can be decomposed into a longitudinal and a transverse component $\vec{p} = \vec{p}_t + \vec{p}_\ell$. $\vec{A}$ is taken to have only a transverse component and vary only in the $\hat{z}$ direction. The transverse components of Eq 2.5 decompose into

$$\frac{\partial}{\partial t} \left(\vec{p}_t - \frac{e}{c} \vec{A} \right) + \frac{p_\ell}{\gamma m} \frac{\partial}{\partial z} \left(\vec{p}_t - \frac{e}{c} \vec{A} \right) = 0, \tag{2.6}$$

where $p_\ell = p_z$. The transverse momentum is then

$$\vec{p}_t = \frac{e}{c} \vec{A}. \tag{2.7}$$

The longitudinal component of the fluid equation is given by

$$\frac{\partial p_\ell}{\partial t}+\frac{\vec{p}\cdot\nabla\vec{p}}{\gamma m}=-e\left[-\nabla\phi+\frac{\vec{p}\times\nabla\times\vec{A}}{\gamma mc}\right]. \tag{2.8}$$

The vector potential can be substituted by taking the curl of Equation 2.7. The curl of the longitudinal component can also be added since $\nabla\times\vec{p_\ell}=0$. Additionally, since $\vec{p}=\gamma m\vec{v}$, γ can be rewritten as $\gamma=\sqrt{1+\frac{p^2}{m^2c^2}}$. Equation 2.8 then becomes

$$\frac{\partial p_\ell}{\partial t}+\frac{\vec{p}\cdot\nabla\vec{p}}{m\sqrt{1+\frac{p^2}{m^2c^2}}}=e\nabla\phi-\frac{\vec{p}\times\nabla\times\vec{p}}{m\sqrt{1+\frac{p^2}{m^2c^2}}}. \tag{2.9}$$

The basic vector identity

$$\nabla\left(\vec{A}\cdot\vec{B}\right)=\vec{A}\times\left(\nabla\times\vec{B}\right)+\vec{B}\times\left(\nabla\times\vec{A}\right)+\left(\vec{A}\cdot\nabla\right)\vec{B}+\left(\vec{B}\cdot\nabla\right)\vec{A}, \tag{2.10}$$

can be transformed into

$$\frac{\vec{A}\cdot\nabla\vec{A}}{\sqrt{1+A^2}}+\frac{\vec{A}\times\nabla\times\vec{A}}{\sqrt{1+A^2}}=\nabla\sqrt{1+A^2}. \tag{2.11}$$

The longitudinal component of the fluid equation can now be written as

$$\frac{\partial p_\ell}{\partial t}=e\nabla\phi-m_0c^2\nabla\left(\gamma-1\right) \tag{2.12}$$

. This is the relativistic version of the ponderomotive force. In the non-relativistic limit, this can be shown to reduce to the standard ponderomotive force. The term in the gradient, along with the m_0c^2 coefficient, is called the *ponderomotive potential.* Numerically this is given by

$$U_p=m_0c^2\left(\sqrt{1+\frac{I\lambda_{\mu m}^2}{1.37\times10^{18}}}-1\right), \tag{2.13}$$

for linear polarization and

$$U_p = m_0c^2 \left(\sqrt{1 + \frac{I\lambda_{\mu m}^2}{2.8 \times 10^{18}}} - 1\right), \tag{2.14}$$

for circular polarization. There is often some confusion over factors of 2 in the intensity relations. The ponderomotive potential is the maximum energy that can be transferred to the electrons in the acceleration. For a laser intensity defined in terms of time averaged fields, the time averaged γ is the same for linear and circular polarization since the maximum γ is $2\times$ higher for linear polarization but the time averaging introduces a factor of $\frac{1}{2}$. The maximum energy transferred via jxB is related to the peak field. For a given intensity the peak field is $\sqrt{2}$ higher for linear polarization, hence the factor of 2 difference in the denominators.

The physical mechanism for the jxB acceleration can now be discussed in more detail. A single relativistic electron in an EM wave will remain in phase with the wave until it detunes (since v is always < c). The electron gains energy on the order of the ponderomotive potential. For a temporally finite wave, however, the electron gives back its energy to the wave as it passes. The electron is then again at rest but with a net forward displacement. The only way for the electron to gain energy from the wave is for it to dephase after it has gained energy. This happens at the critical surface where the laser is reflected. If the electrons have the appropriate phase to launch across the critical surface, they can escape from the wave with a forward directed energy up to the ponderomotive potential.

The electron energy spectrum is commonly taken to scale with the ponderomotive potential. This scaling usually takes the electron distribution as an exponential with the ponderomotive potential as the mean energy of the distribution. This is seem in both computational and experimental results [23], [1], [36]. In order for the electrons to gain energy greater than the ponderomotive potential, they must dephase from the laser field before the critical surface and receive multiple ponderomotive kicks. The stochastic nature of receiving multiple ponderomotive kicks from dephasing in the underdense plasma lends itself to a temperature distribution with a ponderomotive mean energy. The exact nature of the dephasing is still a subject of active computational research [37].

Steepening of the density gradient can also reduce the temperature of the relativistic electrons [34]. If the density profile is long (which is the case for a large preformed plasma), the skin depth is approximately the electron excursion distance and the electrons can be fully accelerated in the ponderomotive potential. This density profile can be shortened through either a small initial preplasma or through ponderomotive acceleration of the ions from an intense laser. If the density profile is steepened to the point where the skin depth is shorter than the acceleration length, the electrons can no longer be fully accelerated by the ponderomotive potential and the electron temperature drops. Since the skin depth is proportional to $\frac{1}{\omega_p}$, or rather, the density at the critical surface, the temperature drops by a factor of $\sqrt{\frac{\gamma n_c}{n_p}}$ where n_p is the electron density of the plasma slab. This is seen in PIC simulations by Chrisman, Sentoku, and Kemp [8] where the absorbed electrons are parameterized in two components each containing half the energy, one with $T_h = m_e c^2 \sqrt{\gamma - 1}$ and one with $T_c = m_e c^2 \sqrt{\gamma - 1} \sqrt{\frac{\gamma n_c}{n_p}}$.

Recent particle-in-cell (PIC) simulations propose a more complicated story [37]. As electrons from the critical surface are launched into the target from the jxB force, a potential well is set up at the front surface by the electrostatic field from the charge imbalance. This coulomb barrier is on the order of tens of MV. On the laser side the plasma is hot so the electrons have a long debye length and cannot effectively shield out the potential. Electrons launched forward into the barrier bounce back and have their phase randomized. They can then be accelerated again by the jxB force, gaining additional energy until they have sufficient energy to penetrate the barrier. Since the electrons receive multiple stochastic kicks from the jxB acceleration, the ponderomotive potential can be treated like a temperature of the accelerated electrons. Only a small high energy tail of electrons of these electrons cross the coulomb barrier and enter the target. In 2-D, however, the laser spot is tightly focused and the electrons might go around the coulomb barrier. On the other side of the coulomb barrier, the colder material has a short debye length that screens out the electrostatic potential. The skin depth is longer than the debye length so the laser fields extend past the coulomb barrier. Electron on this side can enter the field region and get hit by the jxB acceleration. They are then launched forward into the target with a maximum energy up to the ponderomotive potential. The net electron spectrum from a steepened density gradient thus consists of two components, the bulk with an energy up to the ponderomotive potential, and a hot tail with a temperature on the order of the ponderomotive potential.

Other factors can affect the electron acceleration and laser absorption. The laser can self-focus in the underdense plasma, leading to fields larger than those calculated from the vacuum laser intensity. Additionally, when the wave is reflected from the critical surface, a standing wave is set up, resulting in field amplitudes up to 2× the incoming field amplitude. These effects are discussed in much greater detail elsewhere [37].

For oblique incidence p-polarized light, other absorption mechanisms come into play. If the preformed plasma has a long scale length, the normal component of the electric field can resonantly drive electron plasma waves in a mechanism called resonance absorption [35]. For laser intensities of interest to fast ignition, however, the ponderomotive force of the laser is sufficient to steepen the density gradient such that the electrons are actually pulled out into vacuum, breaking the resonance. In this limit, the electrons are pulled out and launched back into the target with the oscillation of the electric field in a process called vacuum heating [35]. This absorption mechanism is then very similar to the jxB mechanism except that the electrons are accelerated by the longitudinal E field at 1ω rather than by the transverse E field at 2ω.

The classical ejection angle of an electron in a laser field can also be derived from the relativistic equations of motion by calculating the ratio of the transverse to longitudinal momentum. Following Meyer-ter-Vehn [38], the Lagrangian of a relativistic particle with charge q in an electromagnetic potential is given by

$$L(\mathbf{r}, \mathbf{v}, t) = -mc^2\sqrt{1 - \frac{v^2}{c^2}} + \frac{q}{c}\mathbf{v} \cdot \mathbf{A} - q\phi. \tag{2.15}$$

The Euler-Lagrange equation is

$$\frac{d}{dt}\frac{\partial L}{\partial \mathbf{v}} - \frac{\partial L}{\partial \mathbf{r}} = 0. \tag{2.16}$$

For a plane wave the Lagrangian has no gradient in the transverse direction (A,ϕ are only functions of z and t). $\partial L/\partial \mathbf{r}_\perp = 0$ so the transverse canonical momentum $\partial L/\partial \mathbf{v}_\perp$ is a constant of the motion. This is given by

$$\mathbf{p}_\perp + \frac{q}{c}\mathbf{A}_\perp = \text{constant}, \tag{2.17}$$

as in Equation 2.7 since for a transverse plane wave $\mathbf{A}_\parallel = 0$. Another constant of the motion can be derived from the functional dependence of the vector potential, since $A = A\left(t - \frac{z}{c}\right)$. Therefore, $\frac{\partial}{\partial t} = c\frac{\partial}{\partial z}$. From the Hamiltonian

$$\frac{dH}{dt} = \frac{dE}{dt} = -\frac{\partial L}{\partial t} = c\frac{\partial L}{\partial z} = c\frac{d}{dt}\frac{\partial L}{\partial v_z} = c\frac{dp_z^{can}}{dt} = c\frac{dp_z}{dt}, \tag{2.18}$$

since $A_z = 0$ for a plane wave. Therefore

$$E - cp_z = \text{constant}. \tag{2.19}$$

If the initial velocity of the particle is small, we can consider it at rest. Then

$$E - cp_z = mc^2. \tag{2.20}$$

The kinetic energy is given by

$$E_{kin} = E - mc^2 = p_z c = (\gamma = 1)\, mc^2 \Rightarrow \gamma = 1 + \frac{p_z}{mc}. \tag{2.21}$$

From the total energy of the particle

$$E^2 = p^2c^2 + m^2c^4 = \gamma^2 m^2 c^4 \Rightarrow \gamma = \sqrt{1 + \frac{p_{total}^2}{m^2c^2}}. \tag{2.22}$$

Equating the γ's and expanding in terms of the components $p_{total}^2 = p_\perp^2 + p_z^2$,

$$p_z = \frac{p_\perp^2}{2mc}. \tag{2.23}$$

Using $\gamma = 1 + \frac{p_z}{mc}$, after some algebra the ratio $\frac{p_\perp}{p_z}$ can be written as

$$tan\theta = \frac{p_\perp}{p_z} = \sqrt{\frac{2}{\gamma - 1}}. \tag{2.24}$$

This is the classical ejection angle of a charged particle in the field of an electromagnetic wave. For a 1 MeV electron, this ejection angle is 45°, narrowing with increasing energy. This angle can be taken as the ejection angle of an electron out of the laser focal spot. This has been demonstrated experimentally by Moore et al. [39] using magnetic electron spectrometers.

2.2 Cold Matter Electron Transport

As fast electrons travel through a material they interact with the electrons and nuclei of the medium through elastic and inelastic scattering processes. In this way, they lose energy due to collisions and radiation, scatter from their initial trajectory, and generate secondary electrons that undergo the same processes. Photons are also generated due to Bremsstrahlung, impact ionization and fluorescence, and annihilation radiation. These photons also interact with the medium through photoelectric, Compton, and pair production processes to generate secondary electrons and positrons. This entire process is thus a coupled electron-photon transport problem, and involves tracking the shower of particles generated to some energy endpoint.

This coupled transport in cold matter is modeled using the Monte Carlo code `Integrated Tiger Series 3.0`. `ITS 3.0` is based off the original `ETRAN` code developed by Berger and Seltzer [40] in the late 1960's. Since then the code has been modified to incorporate 2-D and 3-D geometries, broadened to lower energy photon transport down to 1 keV, and extended to include static electric and magnetic fields. `Integrated Tiger Series 3.0` now comprises a set of 8 codes for the different combinations of geometry, fields, and low energy physics.

The physical model in `ITS 3.0` includes the following electron and photon transport effects [33]:

1. Electron/Positron Interactions
   - Energy loss straggling
   - Elastic scattering
   - Production of knock-on electrons
   - Impact ionization and production of fluorescence photons and Auger electrons
   - Bremsstrahlung production
   - Annihilation radiation
2. Photon Interactions
   - Photoelectric absorption: production of photoelectrons, Auger electrons, fluorescence photons
   - Incoherent scattering with the production of scattered electrons
   - Coherent scattering
   - Pair production

The physics models and cross sections for the different processes of the `ETRAN` core are described in a paper by Seltzer [41]. A few of the key physical processes for this thesis are described here, including the electron energy loss, Bremsstrahlung production, and inner shell ionization.

2.2.1 Collisional Stopping Power

The electron stopping powers are described in the authoritative report by the International Commission on Radiation Units and Measurements (ICRU Report 37) entitled "Stopping Powers of Electrons and Positrons" [42]. The electron energy loss is described by two components: losses due to collisions with atomic electrons and radiative losses due to Bremsstrahlung emission

$$\left(\frac{dE}{ds}\right)_{total} = \left(\frac{dE}{ds}\right)_{collisional} + \left(\frac{dE}{ds}\right)_{radiative} . \tag{2.25}$$

The collisional stopping power is due to inelastic electron-electron scattering. Current formulations are based on the Bethe model [43], [44]. The description here follows a combination of derivations and summaries by Rohrlich and Carlson [45], Bethe [43], [44], [46], Sakurai [47], and the ICRU [42]. The mass collisional stopping power is described by integrating over the cross section for inelastic scattering

$$\frac{1}{\rho}S_{col} = \frac{N}{\rho}Z\int W\frac{d\sigma}{dW}\,dW, \tag{2.26}$$

where S_{col}/ρ is in units of MeV cm^2g^{-1}, N is the number of atoms/volume, Z is the atomic number, and W the energy transferred in a collision. This stopping power is broken down into two regimes based on the energy transfer. A cutoff value for the energy transfer W_c is defined, where W_c is large relative to the binding energies of the electrons, and impact parameters associated with $W < W_c$ are large relative to the atomic dimensions. This is described by

$$\frac{1}{\rho}S_{col} = \frac{1}{\rho}S_{col}\left(W < W_c\right) + \frac{1}{\rho}S_{col}\left(W > W_c\right). \tag{2.27}$$

Physically, the two components break down into inelastic collisions where the atomic electron remains bound to the nucleus, and where the atomic electron is ionized.

The cross section for large impact parameter inelastic scattering is derived from time-dependent perturbation theory. Following Sakurai [47], the cross section for scattering of an electron off an atomic system in the first Born approximation is given by

$$\frac{d\sigma}{d\Omega}\left(0 \to n\right) = \left(\frac{k'}{k}\right)L^6\left|\frac{1}{4\pi}\frac{2m}{\hbar^2}\langle\mathbf{k}', n|V|\mathbf{k}, 0\rangle\right|^2, \tag{2.28}$$

where $|\mathbf{k}, 0>$ represents $\mathbf{k}$ momentum state of the incident electron and the ground state of the atom and $|\mathbf{k}', n>$ represents the momentum of the outgoing electron and the n excited state of the atom. L represents the dimension of a box in the box normalization scheme for the momentum state. The incident electron can interact with the nucleus and each of the atomic electrons. The potential is then given by

$$V = -\frac{Ze^2}{r} + \sum_i \frac{e^2}{|\mathbf{x} - \mathbf{x}_i|}. \tag{2.29}$$

This potential is substituted into Equation 2.28. In evaluating the matrix elements, the first term of the potential can be removed from the atomic integration because the r coordinate depends on the location of the incident electron and the nucleus, not the atomic electrons. $< n|0 >$ is just $\delta_{n,0}$ which is 0 if the atomic state is excited. This term is thus only important in elastic scattering. The second term is evaluated using a change of variables from $\mathbf{x} \rightarrow \mathbf{x} + \mathbf{x}_i$ and performing a Fourier transform of $\frac{1}{|\mathbf{x}-\mathbf{x}_i|}$. The inelastic cross section can now be rewritten as

$$\frac{d\sigma}{d\Omega}(0 \rightarrow n) = 4Z^2 a_0^2 \left(\frac{k'}{k}\right) \frac{1}{(qa_0)^4} \left| \frac{1}{Z} \langle n | \sum_i e^{i\mathbf{q}\cdot\mathbf{x}_i} |0\rangle \right|^2, \tag{2.30}$$

where $a_0 = \frac{\hbar^2}{e^2 m_e}$. The cross section is rewritten in terms of the momentum transfer using

$$q^2 = |\mathbf{k} - \mathbf{k}'|^2 = k^2 + k'^2 - 2kk'cos\theta. \tag{2.31}$$

The cross section then becomes

$$\frac{d\sigma}{dq} = \frac{2\pi q}{kk'} \frac{d\sigma}{d\Omega}. \tag{2.32}$$

The energy loss rate per unit length is Nσ. The total cross section is computed by integrating the differential cross section over all $\mathbf{q}$ and summing over the energy states. This is given by

$$\frac{dE}{dx} = \frac{8\pi N}{k^2 a_0^2} \sum_n (E_n = E_0) \int_{q_{min}}^{q_{max}} \left| \langle n | \sum_i e^{i\mathbf{q}\cdot\mathbf{x}_i} |0\rangle \right|^2 \frac{dq}{q^3}. \tag{2.33}$$

This summation was first performed by Bethe and can be evaluated exactly [43]. With a few pages of algebra detailed by Bethe and Jackiw [46] the stopping power becomes

$$\frac{dE}{dx} = \frac{4\pi Z^2 e^4}{m_e v_o^2} NZln\frac{\bar{q}_{max}}{\bar{q}_{min}}. \tag{2.34}$$

This energy loss equation is accurate for both incident electrons and ions. For ions, the maximum momentum transfer is $\hbar q_{max} = 2m_e v_0$. The minimum momentum transfer is taken as some average ionization potential, $q_{min} = \langle I \rangle / \hbar v_0$. For electrons, the maximum momentum transfer is based on the W_c energy cutoff described above so $q_m ax = \sqrt{2mW_c/\hbar^2}$. The minimum energy transfer can still be taken as $q_{min} = \langle I \rangle / \hbar v_0$. The stopping power for nonrelativistic electrons is then given by

$$\frac{dE}{dx} = \frac{2\pi r_e^2 mc^2}{\beta^2} NZln\frac{2m_e v_0^2 W_c}{\langle I \rangle^2}. \tag{2.35}$$

The relativistic description was first given by Bethe in 1932 and is quoted here as

$$\frac{dE}{dx} = \frac{2\pi r_e^2 mc^2}{\beta^2} NZ\left(ln\frac{2m_e v_0^2 W_c}{\langle I \rangle^2 (1-\beta^2)} - \beta^2\right). \tag{2.36}$$

The mean ionization potential is a free parameter in this model. *Ab initio* calculations must take into the account the specific electronic structure of the material. Typically, however, this parameter is experimentally determined using proton and alpha-particle stopping data. Most cold matter Monte Carlo codes in use today use values tabulated in ICRU Report 37.

The stopping power due to large energy transfers can be evaluated assuming the atomic electrons are free and at rest. The free-free electron scattering cross section is given by Møller [48] where relativity, spin effects, and indistinguishability of the electrons is taken into account.

$$\sigma\, dW = \frac{2\pi e^4\, dW}{mv^2 W^2 (1-A)^2}\left[1 - \left[3 - \left(\frac{\gamma-1}{\gamma}\right)^2\right] A(1-A) + \left(\frac{\gamma-1}{\gamma}\right)^2 A^2 (1-A)^2\right], \tag{2.37}$$

where $A = \frac{W}{T}$ (the ratio of the energy transfer to the initial kinetic energy), and v is the velocity of the incident electron. With a little algebra the cross section can be rewritten as

$$\frac{d\sigma}{dA} = \frac{\chi}{T}\left[\frac{1}{A^2} + \frac{1}{(1-A)^2} + \left(\frac{\gamma-1}{\gamma}\right)^2 - \frac{(2\gamma-1)}{\gamma^2}\frac{1}{A(1-A)}\right], \tag{2.38}$$

where $\chi = 2\pi r_e^2 mc^2/\beta^2$. The average energy loss per unit path length of Z electrons is given by

$$\frac{dE}{dx} = ZNT\int_{W_c/T}^{1/2} A\left(\frac{d\sigma}{dA}\right) dA, \tag{2.39}$$

where the minimum energy transfer is the cutoff energy W_c and the maximum energy transfer is half the initial kinetic energy due to indistinguishability of the particles. This is a simple integration, and with the approximation that W_c/T is small, the result is

$$\frac{dE}{dx} = ZN\chi\left[ln\frac{1}{4W_c/T} + 1 - \frac{2\gamma-1}{\gamma^2}ln2 + \frac{1}{8}\left(\frac{\gamma-1}{\gamma}\right)^2\right]. \tag{2.40}$$

Both the free-free inelastic stopping power and the free-bound inelastic stopping power contain the cutoff energy W_c. When these two stopping powers are combined, the cutoff energy cancels. The total collisional stopping power for electrons in cold matter is then given by

$$\left(\frac{dE}{dx}\right)_{col} = \frac{2\pi r_e^2 mc^2}{\beta^2}NZ\left[ln\frac{m_e v^2 T}{2I^2(1-\beta^2)} + ln(1+\tau/2) + F^-(\tau) - \delta\right], \tag{2.41}$$

where $F^-(\tau) = (1-\beta^2)\left[1+\tau^2/8-(2\tau+1)\,ln2\right]$ and $\tau = \frac{T}{m_e c^2} = \gamma - 1$. The parameter δ has been added into the collisional stopping power derived above and represents the density-effect correction present at large densities. For electrons passing through high density materials the stopping power is reduced by the polarization of the medium. Current models primarily rely on calculations by Sternheimer [49] and are important for large densities or high energies, where the Lorenz contraction is significant. A summary of current density effect correction models can be found in ICRU Report 37. Shell corrections (corrections when the $v_{incident} \not\gg v_{bound}$) are usually neglected in the calculation of electron stopping powers and result in errors at low energies. The errors in the collisional stopping powers are estimated at 1-2% above 100 keV, 2-3% in low-Z materials between 10-100 keV, and 5-10% in high-Z materials between 10-100 keV [42].

2.2.2 Bremsstrahlung and Radiative Stopping Power

Electrons also lose energy through radiation as they scatter through the target. This radiative energy loss is called Bremsstrahlung, or braking radiation, since it was first observed during charged particle stopping in a target. Bremsstrahlung is an important source of energy loss for relativistic particles. In the non-relativistic regime, collisional losses dominate. Some qualitative aspects of Bremsstrahlung emission can be derived from elementary E&M and will be shown here. A fully correct evaluation of the cross sections must be done quantum mechanically and can be calculated with various approximations or numerically evaluated using different techniques. The qualitative calculation of the Bremsstrahlung cross sections here loosely follows Jackson [50].

Radiation occurs whenever a charged particle undergoes acceleration. The radiation intensity emitted by a particle of charge ze undergoing arbitrary acceleration is calculated from the Liénard-Wiechert potentials and is given by

$$\frac{d^2I}{d\omega d\Omega} = \frac{z^2e^2}{4\pi^2 c}\left|\int \frac{d}{dt}\left[\frac{\mathbf{n}\times(\mathbf{n}\times\boldsymbol{\beta})}{1-\mathbf{n}\cdot\boldsymbol{\beta}}\right]e^{i\omega(t-\mathbf{n}\cdot\mathbf{r}(t)/c)}\,dt\right|^2, \tag{2.42}$$

where the vector potential has been expanded in Fourier components. To estimate the angular distribution of the radiation, we can take the low frequency limit $\omega \rightarrow 0$. The exponential equals one and the integrand becomes a perfect differential. The spectrum then becomes

$$\lim_{\omega\rightarrow 0}\frac{d^2I}{d\omega d\Omega} = \frac{z^2e^2}{4\pi^2 c}\left|\boldsymbol{\epsilon}^*\cdot\left(\frac{\boldsymbol{\beta}'}{1-\mathbf{n}\cdot\boldsymbol{\beta}'}-\frac{\boldsymbol{\beta}}{1-\mathbf{n}\cdot\boldsymbol{\beta}}\right)\right|^2, \tag{2.43}$$

where c$\boldsymbol{\beta}$ and c$\boldsymbol{\beta}$' are the initial and final particle velocities, respectively. In the non-relativistic limit, the radiation pattern is just that of a dipole, given by

$$\lim_{\omega\to 0}\frac{d^2 I}{d\omega d\Omega}=\frac{z^2e^2}{4\pi^2 c}\left|\boldsymbol{\epsilon}^*\cdot\boldsymbol{\Delta\beta}\right|^2. \tag{2.44}$$

In the relativistic limit and with the small angle approximation, the total radiation in both polarizations reduces to

$$\lim_{\omega\to 0}\frac{d^2 I}{d\omega d\Omega}=\frac{z^2e^2\gamma^4\left|\boldsymbol{\Delta\beta}\right|^2}{\pi^2 c}\frac{(1+\gamma^4\theta^4)}{(1+\gamma^2\theta^2)^4}. \tag{2.45}$$

The radiation pattern in the relativistic limit has a narrow cone angle given by $\theta = 1/\gamma$. The angular distribution is shown in Figure 2-1.

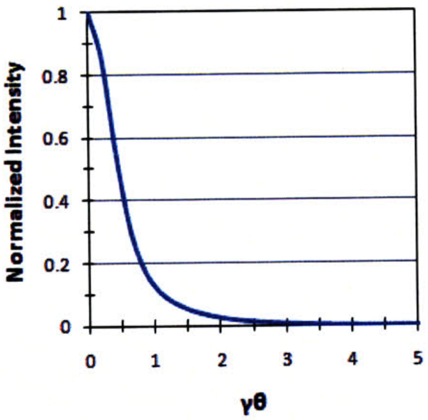

Figure 2-1: Angular distribution of Bremsstrahlung in the relativistic limit. The emission is in a narrow cone angle given by $\theta = 1/\gamma$.

The photon spectrum can also be estimated in a semiclassical way in the low frequency limit for small changes in velocity. The double differential cross section can be integrated over angle to

$$\lim_{\omega\to 0}\frac{dI}{d\omega}=\frac{2}{3\pi}\frac{z^2e^2}{M^2c^3}Q^2, \tag{2.46}$$

where z and M are the charge and mass of the incident particle and Q is the momentum transfer in the collision ($Q = |\mathbf{p}' - \mathbf{p}|$ and $\mathbf{p} = \gamma Mc\boldsymbol{\beta}$).

The double differential cross section over frequency and momentum transfer is given by

$$\frac{d^2\chi}{d\omega dQ} = \frac{dI\left(\omega, Q\right)}{d\omega} \cdot \frac{d\sigma_s}{dQ}\left(Q\right), \tag{2.47}$$

where $\frac{d\sigma_s}{dQ}$ depends on the elastic scattering cross section. The Rutherford cross section can be rewritten in terms of momentum transfer as

$$\frac{d\sigma_s}{dQ} = 8\pi\left(\frac{zZe^2}{\beta c}\right)^2 \cdot \frac{1}{Q^3}. \tag{2.48}$$

Equation 2.47 is now

$$\frac{d\chi^2}{d\omega dQ} = \frac{16}{3}\frac{Z^2e^2}{c}\left(\frac{z^2e^2}{Mc^2}\right)^2 \frac{1}{\beta^2} \cdot \frac{1}{Q}. \tag{2.49}$$

which can be integrated over all momentum transfers to give

$$\frac{d\chi}{d\omega} = \frac{16}{3}\frac{Z^2e^2}{c}\left(\frac{z^2e^2}{Mc^2}\right)^2 \frac{1}{\beta^2} ln\left(\frac{Q_{max}}{Q_{min}}\right). \tag{2.50}$$

In the relativistic limit, the maximum momentum transfer is not set kinematically, but rather by the small momentum transfer limit, given by $Q_{max} = 2Mc$. The minimum momentum transfer occurs at $Q_{min} = p - p' - k$, where p and p' are the momenta of the incident and scattered particles and k is the momentum of the photon. This can be written as $Q_{min} = \frac{M^2c^3\hbar\omega}{2EE'}$. For an elastic collision off the nucleus, the energy loss is only carried away by the photon so $E' = E - \hbar\omega$. The radiation cross section for photon emission can be written as

$$\frac{d\chi}{d\omega} = \frac{16}{3}\frac{Z^2e^2}{c}\left(\frac{z^2e^2}{Mc^2}\right)^2 \frac{1}{\beta^2} ln\left(\frac{\lambda'' EE'}{Mc^2\hbar\omega}\right). \tag{2.51}$$

This formula is only valid in the low frequency limit for photon energies of $< \frac{1}{10}T_0$. More accurate calculations of the Bremsstrahlung cross section rely solutions of the Dirac wave equation for either a coulomb field or a screened, nuclear field. The baseline calculations were done by Bethe and Heitler [51], who solved the scattering cross section in the Born approximation for the coulomb potential. There are a number of different calculations of the cross section using nonrelativistic coulomb, relativistic coulomb wave, and free particle Born approximation wave functions, and for screened and unscreened coulomb potentials. These are summarized in an exhaustive paper by Koch and Motz [52], which classifies the cross sections based on their approximations and for single, double, and triply differential cross sections.

`ITS 3.0` uses an amalgam of Bremsstrahlung differential cross sections including results of numerical phase-shift calculations by Tseng [53] and Pratt [54], [55] for nuclear Bremsstrahlung for electrons < 2 MeV, analytic high-energy nuclear field Bremsstrahlung by Davies et al. [56] and Olsen [57] with coulomb and screening corrections, and analytic electron-electron Bremsstrahlung calculations by Haug [58]. Nuclear Bremsstrahlung cross sections between the low and high energy limits are spline interpolated. The `ITS 3.0` cross section selection follow recommendations by the ICRU [42].

The differential cross section for Bremsstrahlung production as a function of photon energy is shown in Figure 2-2 for Al at three different energies. These cross sections are from tabulations by Seltzer and Berger in Atomic Data and Nuclear Data Tables [59], [60] and include both nuclear and electron-electron Bremsstrahlung. The cross sections show a continuous energy distribution scaling with 1/k up to a

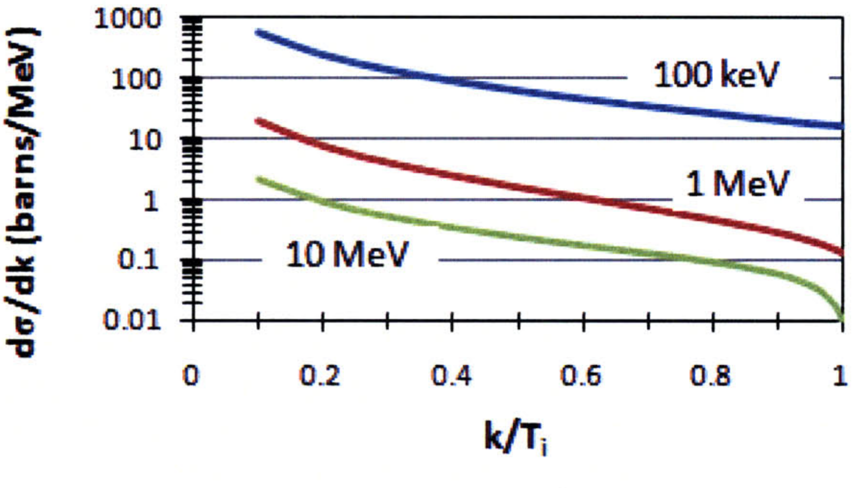

Figure 2-2: The differential cross section for Bremsstrahlung production in Al for 100 keV, 1 MeV, and 10 MeV incident electron energies. The photon energy is normalized to the initial electron kinetic energy. The cross sections include both nuclear and electron-electron Bremsstrahlung.

cutoff at the maximum energy. These cross sections are integrated over emission angle and secondary electron energy. This differential cross section in energy can be combined with the angular distribution from Equation 2.44 to obtain the double differential cross section.

The radiative energy loss can be calculated from the Bremsstrahlung cross sections by taking the moment of the differential cross section in energy. This is given by [42]

$$\frac{1}{\rho}\left(\frac{dE}{dx}\right)_{rad} = \frac{1}{uA}\left[\int_0^T k\frac{d\sigma_n}{dk}\,dk + Z\int_0^{T'} k\frac{d\sigma_e}{dk}\,dk\right], \tag{2.52}$$

where u is the atomic mass unit and T' is the photon cutoff in electron-electron Bremsstrahlung given by $T' = mc^2T\left[T + 2mc^2 - \beta\left(T + mc^2\right)\right]^{-1}$. The relative importance of radiative energy loss is shown in Figure 2-3. Figure 2-3 shows the collisional and radiative energy loss components as a function of incident electron energy for solid density aluminum. Radiative losses start to dominate collisional losses at electron energies of a few MeV. The importance of radiative effects scales

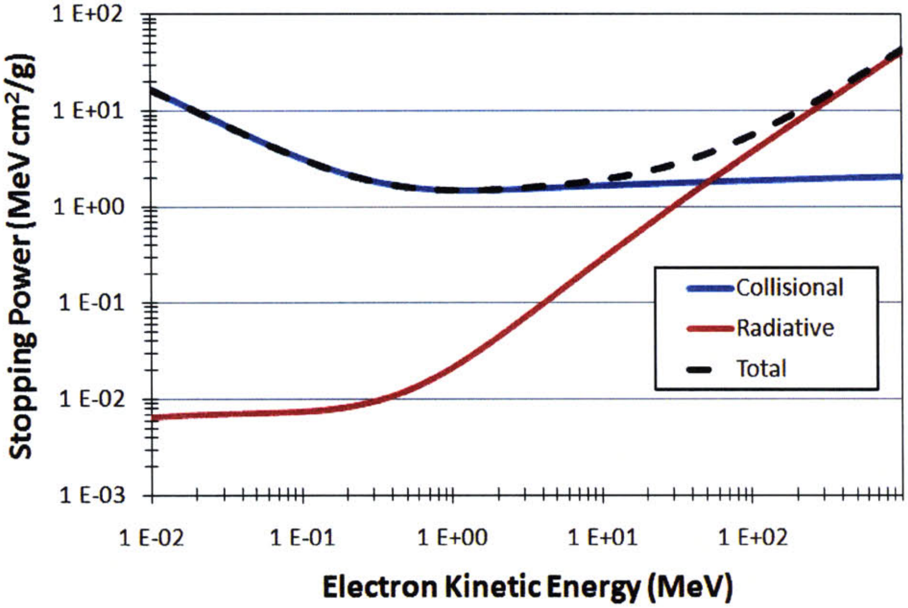

Figure 2-3: The collisional and radiative energy loss components are plotted as a function of energy in solid density aluminum. Radiative losses start to dominate collisional losses at electron energies of a few MeV.

roughly with $Z^{1.5}$ when nuclear screening effects are taken into account, and is thus more significant at lower energies for higher Z materials.

The discussion of Bremsstrahlung so far has been for what is termed "thin target Bremsstrahlung," representing single electrons scattering off single atoms. The radiation distribution in a real target is much more complex, and must account for issues such as the difference between path length and penetration into a target due to scattering, the generation of secondary electrons, and straggling of the energy distribution. The Bremsstrahlung emission from a real target of finite thickness is known as "thick target Bremsstrahlung." A useful discussion of thick target Bremsstrahlung is given by Evans [61]. The differential cross section in energy for thick target Bremsstrahlung can be approximated as the sum of multiple thin target cross sections as the electrons lose energy. The total radiated power scales with the Z of the material, and there is no simple formulation for the angular distribution of radiation. In this work calculation of the Bremsstrahlung emission in a full target is handled by `ITS 3.0`, which accounts for the effects of scattering and secondary particle generation. Thick target Bremsstrahlung effects are thus automatically accounted for in the simulation.

2.2.3 Inner Shell Emission

Energetic electrons propagating through a target collide with atomic electrons, occasionally imparting enough energy to eject them from the atom. When this occurs, a vacancy is generated at one of the energy levels, and is filled by a transition of an electron from a higher energy state. This transition results in the radiation of a photon whose energy is given by the difference in energy levels of the vacancy and the higher energy state. The energy diagram of non-ionized copper is shown in Figure 2-4.

$K\alpha 1$, $K\alpha 2$, and $K\beta$ line emission results from transitions from the L and M shells to vacancies in the K shell. For cold matter, the line energies are just given by the difference in the energy states. A sample spectrum is shown in Figure 2-5 This spectrum was generated by the collisional radiative code FLYCHK [62] and is

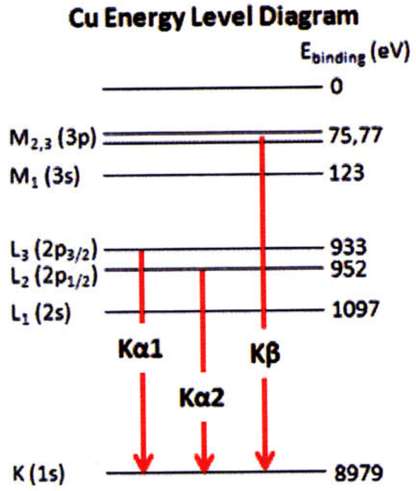

Figure 2-4: Energy diagram of non-ionized copper. Kα1, Kα2, and Kβ line emission results from transitions from the L and M shells to vacancies in the K shell. The line energies are given by the difference in the energy states.

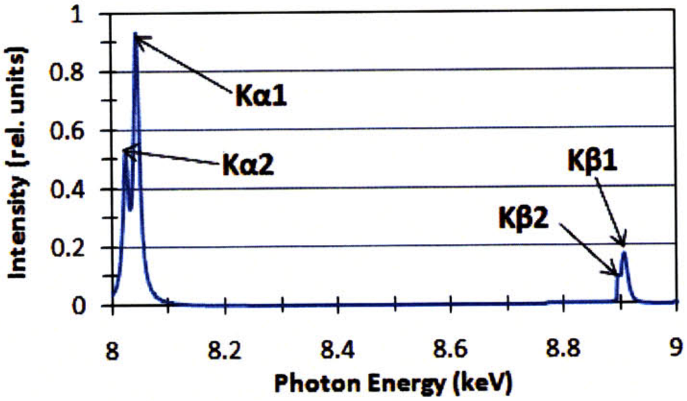

Figure 2-5: Sample Cu line emission from the collisional radiative code FLYCHK. Spectrum courtesy of Sophia Chen.

courtesy of a run by Sophia Chen for a 1 MeV Maxwellian beam of 10^{21} cm^{-3} hot electrons incident on a 10 eV cold Cu slab. This spectrum is similar to those seen in experiments presented in this work. The Cu Kα1 and Kα2 lines have energies of 8.05 keV and 8.03 keV, respectively, and the Cu Kβ line has an energy of 8.9 keV. The relative intensities of the Kα and Kβ lines depend on the transition probability and the relative population of the states, the latter of which is sensitive to the temperature of the material. The ratio of the Kα and Kβ lines has been used to diagnose plasma temperatures in previous laser-plasma experiments [5]. In this work, the absolute intensity of the Kα emission is measured to determine the number of relativistic electrons incident on a Cu fluorescor layer. The emission is calculated using the `ITS 3.0` Monte Carlo code, which uses impact ionization cross sections from Kolbenstvedt [63] and fluorescence yield calculations by Bambynek [64]. Secondary electrons generated in the target also stimulate Kα emission and are included in the simulation. A plot of the Cu Kα cross section as a function of incident electron energy is shown in Figure 2-6

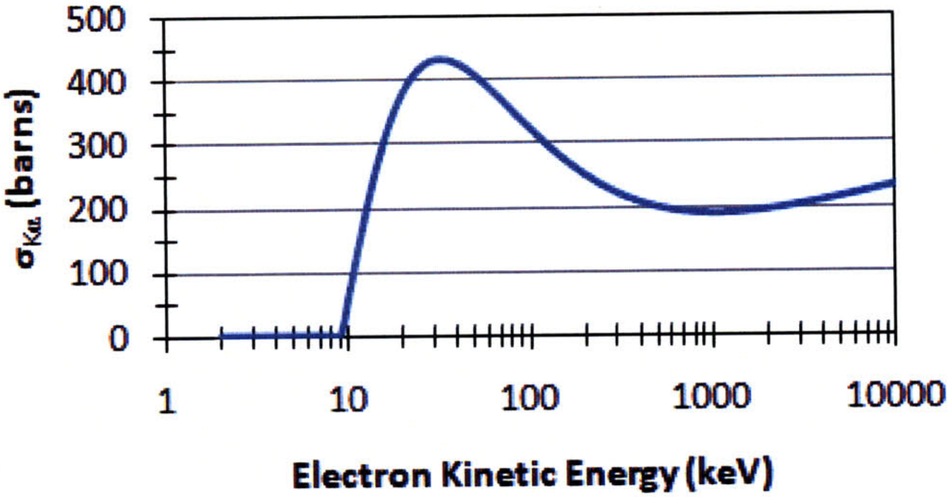

Figure 2-6: The Cu Kα cross section. The cross section peaks at 3-4× the K-shell binding energy.

These cross sections are taken from Deutsch et al. [65], [66], [67]. The cross section peaks at 3-4× the K-shell binding energy and is relatively flat at higher energies. Emission is also isotropic, since it involves relaxation of the atomic electrons rather than a scattering process. This allows measurements to be made without sensitivity to angular distribution, making the Kα emission a useful counter of electrons passing through the fluor.

2.3 Photon Interactions

Photon interactions with matter in energy regimes from a few keV up to a hundred MeV primarily involve three processes: the photoelectric effect, Compton scattering, and pair production. These interactions are discussed in detail by Evans [61] and the physical mechanisms are briefly descried here.

The photoelectric effect involves the complete absorption of an incident photon by a bound atomic electron. From the energy and momentum conservation laws, a free electron cannot completely absorb an incident photon. A bound electron, however, can transfer momentum to the nucleus, allowing for complete absorption. The energy of the ejected electron is then equivalent to the incident photon energy minus the binding energy, given by

$$T = h\nu - E_B. \tag{2.53}$$

In actuality it is slightly less since there will be some recoil of the nucleus. The large mass difference between the electron and nucleus makes this a very small effect.

Compton scattering is very similar to the photoelectric effect in that it also involves the interaction of the photon with an atomic electron. In this case the photon is not completely absorbed, but incoherently scatters off the electron, losing energy and shifting wavelength. This energy is transferred to the atomic electron. The energy regime where Compton scattering is important is much higher than the binding energy of the electrons, and calculation of the cross section treats the electrons as free particles. The relationships between scattering angle, energy, and momentum can be deterministically calculated from a 2-body scattering problem. The Compton differential cross section for scattered unpolarized photons is given by the Klein-Nishina cross section [68]. This effect will be discussed further in Chapter 5, where it is the basis for a proposal for a new diagnostic.

Pair production involves generation of an electron-positron pair from the interaction of the incident photon with the field of a charged particle, primarily the nucleus but also from atomic electrons. The threshold energy for this is $2mc^2$, twice the rest mass of the electron. The pair production process involves complete absorption of the photon. The nuclear (or electron) field is required for momentum conservation. The quantum mechanical description of the pair production process involves treating the energy space as consisting of negative and positive energy states, with an energy barrier of $2mc^2$ surrounding the zero energy. The negative energy states are completely filled. If an incident photon has sufficient energy to excite the electron into a positive energy state, a hole is left in the negative energy space. This hole represents the created positron and the positive energy electron represents the created electron. The cross sections have been calculated by Bethe and Heitler in the first Born approximation [51]. Screening corrections were also included in the original derivations.

Each of these processes dominate in different energy regimes. The total cross sections for the three interactions is shown for Al in Figure 2-7. The photoelectric effect is dominant up to 100 keV. From 100 keV to 10 MeV, the Compton scattering effect is dominant. Pair production has a threshold energy of 1.02 MeV and is the dominant interaction mechanism above 10 MeV.

2.4 History of Electron Spectrum and Conversion Efficiency Measurements

The spectrum and conversion efficiency of laser produced relativistic electrons are important parameters for fast ignition and of great interest in the physics of laser-plasma interactions. As such, there have been a variety of efforts to experimentally measure these parameters. Measurements to infer the electron spectrum have used techniques such as vacuum electron spectrometers [1], [69], nuclear activation [70], Bremsstrahlung [36], buried fluorescent foils [71], proton

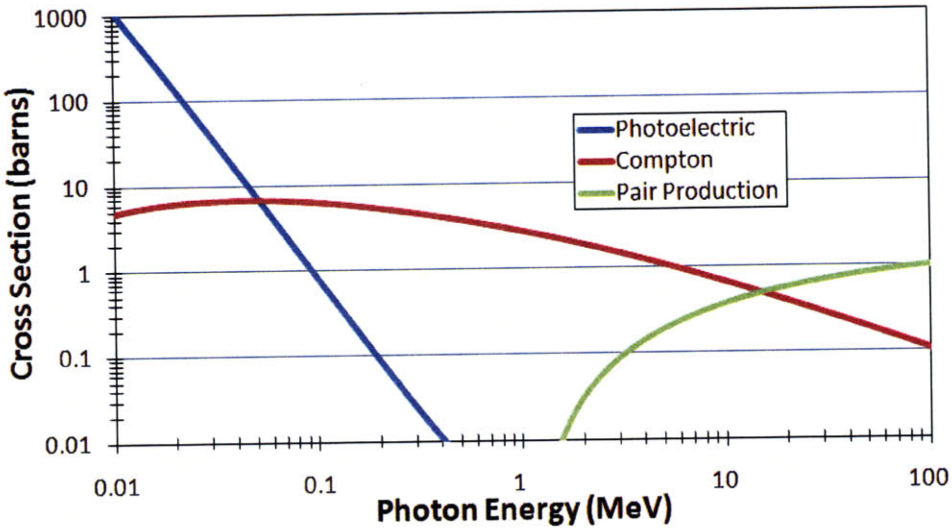

Figure 2-7: Photon interaction cross sections for the photoelectric, Compton scattering, and pair production processes in aluminum. The photoelectric effect is dominant up to 100 keV. Compton scattering dominates from 100 keV to 10 MeV, above which pair production is the dominant process.

emission [2], and coherent transition radiation [72]. The primary results are summarized in this section.

The two principal references for conversion efficiencies both involve measurements of the K-shell yield produced in a target by relativistic electrons. K-shell emission tends to be isotropic, making it useful for quantifying total conversion efficiency without a full angular distribution of instruments. Yasuike [4] used fluorescence yields from buried layer Kα emitters in thick, non-refluxing targets to infer both the slope temperature and conversion efficiency, estimating conversion efficiencies scaling from 10-50% for I=10^{18} to 10^{20} W/cm^2 from Monte Carlo modeling. Theobald et al. [73], Myatt [74], and Nilson [5] measured and modeled the Kα yield in very thin foils with strong refluxing. They found coupling efficiencies of 20%±10%, independent of the laser intensity for I=10^{17} to 10^{20} W/cm^2 using a hybrid particle in cell model. Both of these experiments are described in this section.

2.4.1 Electron Spectral Measurements

The first measurements of ponderomotive scaling were done by Malka and Miquel using vacuum electron spectrometers at the P102 laser at CEA (France) [1]. A 40 J, 300-500 fs beam was used to irradiate thin, 30 μm CH targets at normal incidence for intensities up to 2×10^{19} W/cm^2. Using rear surface electron spectrometer measurements, they found that along the laser axis, the electron spectrum scales with the ponderomotive potential. This is shown in Figure 2-8, taken from the original Phys. Rev. Lett. article [1], where the solid line represents the ponderomotive potential and the data points represent single temperature Boltzmann fits to the spectrometer data.

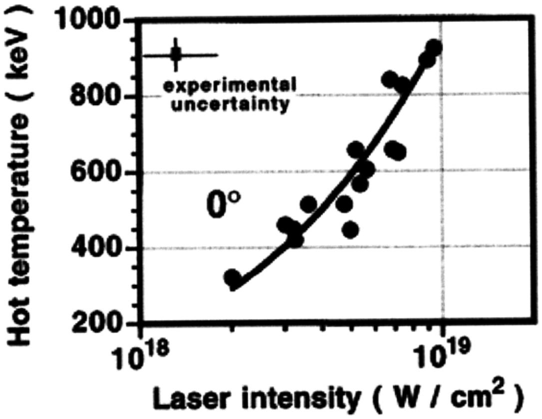

Figure 2-8: The escaping electron spectra along the laser axis are consistent with the ponderomotive potential of the laser. The solid line represents the ponderomotive potential and the data points represent single temperature Boltzmann fits to the spectrometer data. Reprinted with permission from [1]. Copyright (1996) by the American Physical Society.

Comprehensive measurements of Bremsstrahlung, K-shell emission from buried tracer layers, and maximum ion energies by Beg et al. [2] found that the hot electron temperature scales with $I^{1/3}$, lower than the $I^{1/2}$ of the ponderomotive potential. These experiments were performed on the CPA beamline of the VULCAN laser facility. Laser energies were up to 30 J in 700 fs to 1.3 ps for intensities between 10^{17} and 10^{19} W/cm^2. Targets were irradiated at 30° to target normal with p-polarized light. Proton emission off of CH coated glass and Cu targets was measured using CR-39 nuclear track detectors [75], [76]. Using an isothermal rarefaction model acceleration model [77], the maximum proton cutoff energy is related to the debye length at the rear surface. The hot electron temperature is thus proportional to the proton cutoff energy. The maximum proton energy is given by $E_{max} = 1.2 \pm (0.3) \times 10^{-2} \left[I/\left(Wcm^{-2}\right)\right]^{0.313 \pm 0.03}$. Bremsstrahlung emission was also measured using an array of filtered pin diodes and a pair of photomultiplier/scintillator detectors. The photomultipliers were filtered with 2-5 mm of lead, with 1 cm thick Al blocks behind the lead filters to eliminate fluorescence. A sample of the Bremsstrahlung data is shown in Figure 2-9, integrated over a number of shots on a plastic CD target with a intensity of 5 × 10^{18} W/cm^2. A fit through the latter three points gives a temperature of 390 keV.

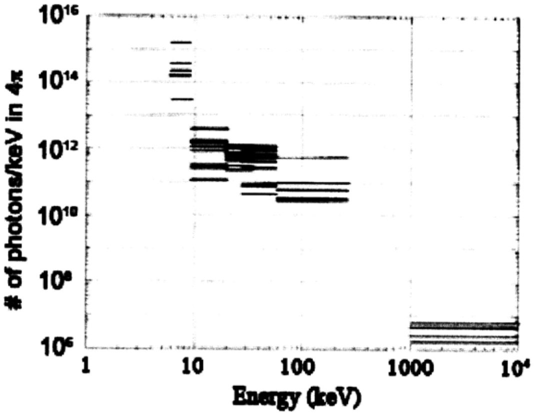

Figure 2-9: Bremsstrahlung data from Beg, et. al.[2], integrated over a number of shots. There are two slope temperatures seen in the photon distribution. Reprinted with permission. Copyright (1997) by the American Institute of Physics.

From the Bremsstrahlung data, the temperature scaling was found to be

$$T_h = 215 I_{18}^{1/3}, \tag{2.54}$$

where the laser intensity is in units of 10^{18} W/cm^2. This is commonly known as Beg scaling, and is currently one of the primary alternative temperature scalings to ponderomotive scaling. Beg attributes the $I^{1/3}$ temperature scaling to a resonance absorption process rather than a jxB process. Recent theoretical work [25] suggests that the $I^{1/3}$ scaling may be due to the reduction of the hot electron temperature due to steepening of the density gradient.

K-shell emission measurements were also performed by Beg using layered Pd and Sn targets of varying thicknesses from 12-72 μm. The K-shell yield was measured using a Single Hit Spectrometer and temperatures inferred from the ratios of the yields based on calculations accounting for electron energy loss, K-shell ionization cross sections, and x-ray mass attenuation coefficients. The temperatures inferred from this technique ranged from 70-200 keV, somewhat lower than from the Bremsstrahlung measurements. This was attributed to an overestimate of the intensity on those shots.

Photonuclear activation measurements for inferring the hot electron spectrum were performed by Stoyer [3] on the NOVA Petawatt laser at Lawrence Livermore. Photons of energies greater than 8 MeV were used to excite the giant resonance oscillation in Au and Ni targets. The ^{197}Au and ^{58}Ni nuclei are excited by the photons and decay into unstable isotopes via (γ, xn) reactions. The gamma emission from the decay of these states were measured using high-purity Ge detectors. Information about the incident photon spectrum was inferred from Monte Carlo simulations with activation cross sections for the various (γ, xn) reactions. Figure 2-10 shows a sample photon spectrum with a best fit hot electron temperature. The inferred temperatures ranged from 3 to 7 MeV for laser intensities up to 3×10^{20} W/cm^2. The inferred temperatures were consistent with the 7 MeV ponderomotive potential, although sometimes colder. These temperature measurements were significantly hotter than those derived from Beg scaling, which predicts a 1.4 MeV slope. Bremsstrahlung and electron spectrometer measurements by Key et al. [78] on NOVA in conjunction with the nuclear activation measurements found two components of the hot electron spectrum, a smaller component with a temperature hotter than the ponderomotive potential, and a larger, colder component. The authors proposed that the hot component may be due to acceleration in the subcritical plasma and the colder component from acceleration at the critical surface.

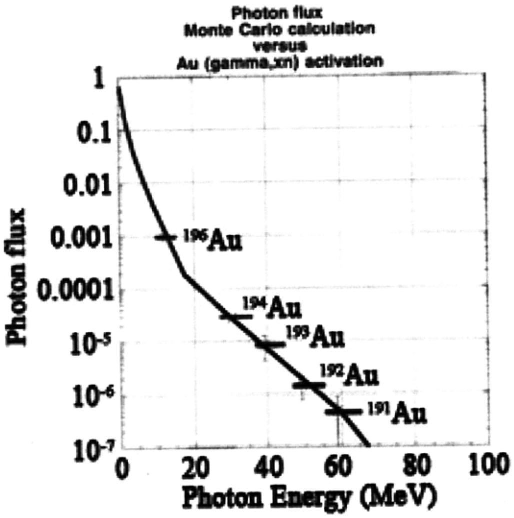

Figure 2-10: A sample photon spectrum with a best fit hot electron temperature. The inferred temperatures varied from 3 to 7 MeV for laser intensities up to $3\times10^{20}W/cm^2$. Taken from Stoyer et al.[3]. Reprinted with permission. Copyright (2001) by the American Institute of Physics.

Norreys et al. [36] performed an experiment on the CPA beamline of the VULCAN laser to measure the hot electron temperature using an electron spectrometer, a Bremsstrahlung spectrometer, and photonuclear activation of Cu foils in order to try and resolve the differences between ponderomotive scaling and Beg scaling. CH, Al, and Pb targets were irradiated at at 45 ° incidence with p-polarized light for intensities up to 10^{19} W/cm^2. The Bremsstrahlung spectrometer consisted of an array of eight filtered plastic scintillators coupled to photomultipliers. They were filtered with 0.1 to 15 cm of Pb to measure the spectrum from 100 keV to 10 MeV. Exponential slope temperatures of the Bremsstrahlung varied between 750 keV to 1.2 MeV, depending on the target material. The authors emphasize, however, that since the measurements are far off axis, these slope temperatures are not indicative of the temperature of the input electron beam. An array of Cu foils was also placed behind the target to measure the activation in the foils. From the activation, the authors inferred temperatures of 1-2 MeV, consistent with ponderomotive temperatures of 1-1.5 MeV for $I\lambda^2 = 5 \times 10^{18}$ to 1×10^{19} Wμm^2/cm^2. The Bremsstrahlung cone angle was measured at 35 ° FWHM. The authors suggest that while their measurements are consistent with the ponderomotive potential, the lower spectral measurements by Beg are perhaps due to a time dependent process where jxB initially dominates until the interaction surface becomes non-planer, after which resonance absorption and vacuum heating start to become important.

In summary, there have been many measurements of the electron spectrum using a wide variety of techniques. Many of the results are inconsistent, with different temperature scalings. The electron spectrum may also scale with other parameters such as the preformed plasma scale length, the focal spot intensity distribution, laser energy, pulselength, the target material, and the angle of incidence. It is also likely that the electron spectrum does not have a single or even dual temperature, and the slope temperatures may depend on the part of the spectrum that is measured. Experiments described in this thesis will seek to carefully address the spectral dependencies.

2.4.2 Conversion Efficiency Measurements

In contrast to the multitude of electron spectral measurements, there are currently only two key experiments that systematically address the question of the electron conversion efficiency in Fast Ignition regimes. Both experiments involve measurements of the K-shell yield, although in different target physics limits. Electrons escaping a small target cause an electrostatic sheath to build up on the surfaces of the target. This electrostatic field pulls escaping electrons back into the target, resulting in the electrons making multiple passes through the target as they are confined by the fields. This process is known as electron refluxing.

Experiments by Wharton [71] and Yasuike [4] used 50 μm buried Mo tracer layers with variable front layer thicknesses of (0.2 to 0.45 g/cm^2 of CH, Al, and Cu) to infer the electron spectrum and conversion efficiency. The electrons lose energy in the front surface layer before reaching the Mo tracer and exciting K-shell emission. The variable thickness of the front layer allows the Mo fluor to sample different parts of the electron spectrum. On the rear surface of the target, a 1 mm CH layer is used to range out electrons to prevent multiple passes through the fluorescor, establishing the non-refluxing limit. Experiments were performed on the NOVA laser with energies up to 400 J in 0.5 ps for intensities up to 3×10^{20} W/cm^2. The K-shell emission was measured using a charged coupled device (CCD) operating in single photon counting mode and the emission modeled using Monte Carlo simulations of the electron transport in the target. Various single temperature distributions were fit to the emission data to estimate a hot electron temperature. The absolute intensity of the K-shell yield, along with the estimated spectrum, were used to calculate a total conversion efficiency. Figure 2-11 is taken from Yasuike [4] and shows the predicted conversion efficiencies for three different intensities. The absorption is intensity dependent, and ranges from 10% at 10^{18} W/cm^2 to 50% at 10^{20} W/cm^2.

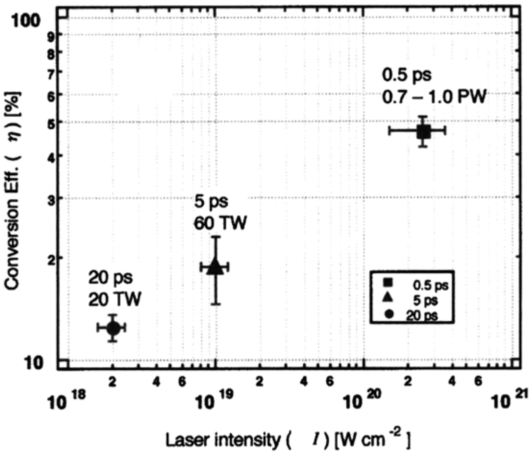

Figure 2-11: Conversion efficiencies inferred using buried fluor techniques range from 10-50% for intensities from $10^{18} - 10^{20} W/cm^2$. Taken from Yasuike et al.[4]. Reprinted with permission. Copyright (2001) by the American Institute of Physics.

Unfolding of the electron spectra and conversion efficiency using Monte Carlo techniques is complicated by the Ohmic and magnetic fields that build up in the target due to the large electron currents. Davies performed a computational "experiment" [79] to study the errors associated with Monte Carlo interpretations. Davies developed a resistive transport model where the fast electron current is opposed by a background return current in order to maintain charge neutrality. This return current then generates a field according to Ohm's law $\vec{E} = \eta \vec{j}_b$. Electric and magnetic fields are due to the fast electron current and the return current. Apart from the fields, the electrons scatter and lose energy due to collisions. The collisional energy loss is assumed to be proportional to the K-shell emission. Using this model Davies injected an exponential distribution of electrons with a 212 keV mean energy into an infinite Al target with a 30% absorption for a laser intensity of 2×10^{18} W/cm^2. The K-shell emission produced by the resistive transport model is then interpreted with a standard cold matter Monte Carlo model. An apparent two temperature distribution was found when using the Monte carlo model, with a colder component in the first few tens of microns and a hotter component at larger depths. The mean energy and absorption calculated for the cold component was 50 keV and 14.3%. The hot component gave a mean energy of 185 keV and 10.9% absorption. Davies argues that interpreting temperatures and conversion efficiencies from buried layer fluorescence underestimates both the mean energy and the conversion efficiency.

Theobald et al. [73], Myatt [74], and Nilson [5] measured the K-shell yield from thin, low mass foils with strong refluxing. Experiments were performed at the Rutherford Appleton Laboratory Petawatt (1.06 μm, 400 J, 0.4 ps, $I_{max} = 4 \times 10^{20}$ W/cm^2) and at the MTW laser at the Laboratory for Laser Energetics (1.06 μm, 5 J, 1 ps, $I_{max} = 2 \times 10^{19}$ W/cm^2). The targets were Cu foils from 1-75 μm thick and 0.01 to 8 mm^2 in area. The K-shell emission was measured using a Single Hit Spectrometer. In the full refluxing regime, the electrons are assumed to deposit all of their energy in the target, so that the total K-shell yield is proportional to the conversion efficiency. The target interaction was estimated using a model where the hot electrons traverse an infinite medium and lose energy due to cold matter collisional losses. The K-shell emission was then calculated from the cross sections. The electrons are assumed to have a exponential distribution with a temperature equivalent to the ponderomotive potential for intensities $> 10^{18}$ W/cm^2. For lower intensities, a $I^{1/3}$ temperature scaling was used. Since the target is in a full refluxing regime, resistive losses are small because the refluxing electrons act as a return current, shorting out the Ohmic potential. The refluxing efficiency of the target was estimated at > 90% using a capacitance model. The estimated conversion efficiencies are shown in Figure 2-12.

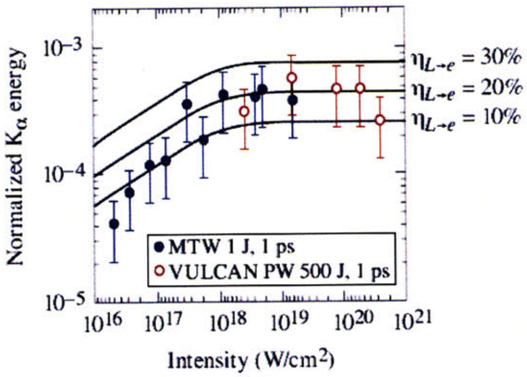

Figure 2-12: Conversion efficiencies inferred from Kα emission in low mass targets were 20% ± 10%, independent of the laser intensity. Taken from Nilson et al.[5]. Reprinted with permission. Copyright (2008) by the American Institute of Physics.

The calculated conversion efficiencies are 20% ± 10%, independent of the laser intensity. Estimates of the target heating using a hybrid particle-in-cell code calculated temperatures of around a few hundred eV, and were consistent with ratios of the Kβ to Kα yields.

One major component neglected in this conversion efficiency analysis is the energy loss to ion acceleration. As the electrons bounce off the sheath fields, they transfer energy to the ions, resulting in acceleration of collimated proton beams off the surface. These proton beams have been seen in previous experimental work [80]. This energy loss channel can be significant, and as such, Nilson states [81] that the measured conversion efficiencies are to be taken as lower bounds.

So far experimental work on the electron conversion efficiency has been limited and current measurements are largely inconsistent. Conversion efficiency measurements thus remain a wide open area of research. The goal of this thesis is to narrow the uncertainties in the conversion efficiency measurements. Additionally, this thesis seeks to measure the conversion efficiency and electron spectrum in a coupled way, providing better measurements of the number of electrons useful for fast ignition.

Chapter 3

Experimental Facilities and Diagnostic Descriptions

This chapter describes the laser system and the diagnostics used in this thesis. An overview of the Titan laser is first presented, along with the laser diagnostics that characterize the focal spot, pulse length, and prepulse level. This is followed by a description of the Hard X-ray Bremsstrahlung Spectrometer (HXBS), including details of the implementation and design history, a description of the dosimeters, Monte Carlo modeling of the response, and calibration of the instrument. Finally, the Single Hit Spectrometer for measuring k-shell emission is summarized with details of its setup and calibration, associated analysis algorithms, and sample data analysis.

3.1 The Titan Laser System

The Titan laser is a petawatt class laser that uses Optical Parametric Chirped Pulse Amplification (OPCPA) to achieve laser intensities of up to 9×10^{19} W/cm^2 on target [32]. OPCPA is a technique that involves both Chirped Pulse Amplification (CPA) and Optical Parametric Amplification (OPA). Chirped Pulse Amplification is a technique for achieving high laser power that is currently used in almost all of the high power lasers in the world. Before the development of CPA, laser powers had been limited by the onset of nonlinear effects; laser intensities above a threshold of GW/cm^2 would self-focus and damage the laser optics. Mitigation efforts involve reducing the beam intensity either by spreading out the beam in space or stretching the pulse in time. Larger beam optics, however, quickly become cost prohibitive. CPA was developed by Strickland and Mourou [17] in the mid 1980s and overcame these limitations by stretching out the laser pulse temporally and spectrally prior to amplification. The pulse is stretched by a pair of gratings that "chirp" the pulse, arranged such that the higher frequency part of the spectrum travels a longer path length than the lower frequency part. The pulse is typically stretched in time by a factor of 10^3-10^5 and safely amplified through the amplifier chain. After amplification, the pulse is recompressed by a second pair of gratings before final focusing on target.

Optical Parametric Amplification substitutes the laser gain medium for a nonlinear crystal pumped by shorter wavelength pump laser [82]. The signal beam passes through the crystal which is separately pumped by the higher frequency pump beam. Photons from the pump beam are downconverted to photons of the signal beam, with an idler beam carrying away the leftover energy. OPA provides higher gain per unit volume than a standard laser medium. More importantly, however, the pulselength of the pump laser can be matched to the pulselength of the signal beam such that the gain medium is only "on" when the signal beam is being amplified, thus reducing spontaneous emission and increasing the intensity contrast of the laser relative to the prepulse.

The Titan laser makes use of both of these techniques to achieve high laser intensities. A schematic of the Titan laser is shown in Figure 3-1. The seed pulse originates in a commercial Time Bandwith Products GLX-200 master oscillator which generates pulses of 100-200 fs at 1053 nm. The seed pulse then passes through an Offner Pulse Stretcher [83], which stretches the pulse to 1.6 ns while minimizing beam abberations. The stretched pulse then passes into the OPCPA preamplifier, which consists of a set of BBO crystals (BaB_2O_4) pumped by a 1.06 μm beam amplified through a YLF amplifier and frequency doubled to 532 nm. The

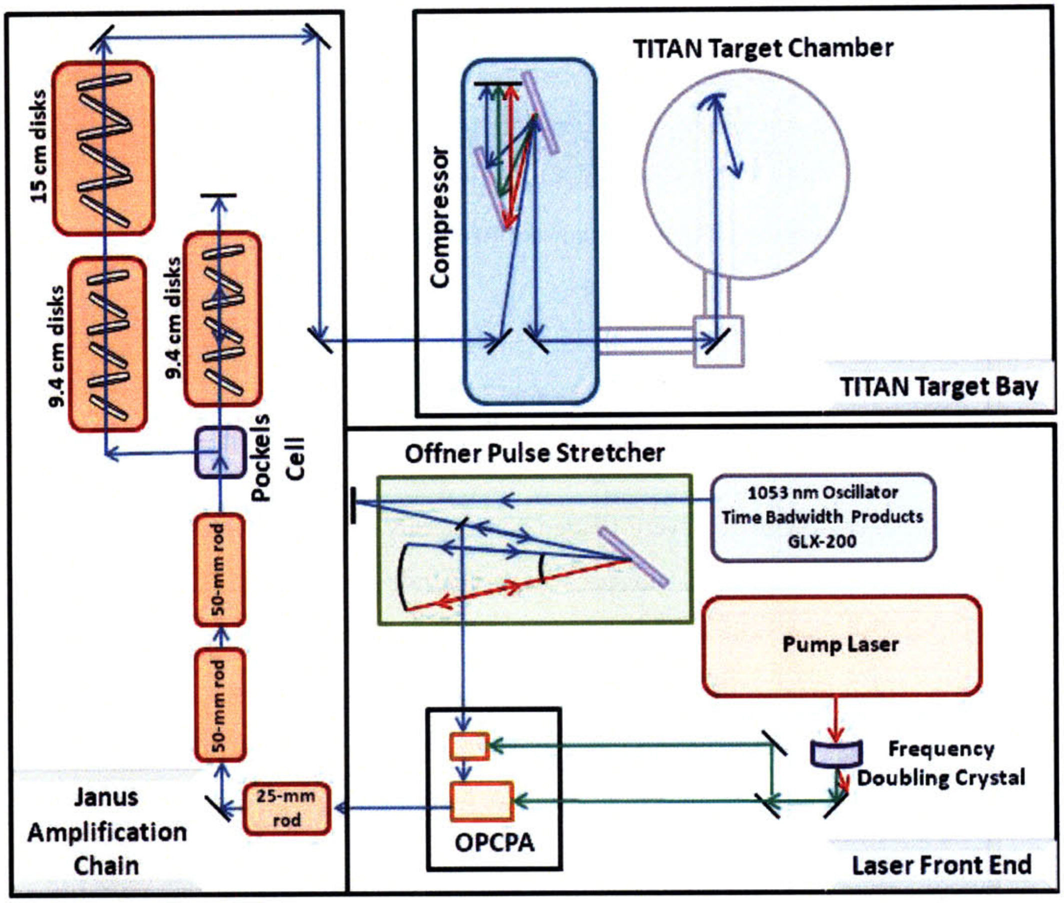

Figure 3-1: The Titan laser system.

seed pulse is amplified up to a few mJ in the OPCPA. It then passes through 25 and 50 mm flashlamp pumped rod amplifiers where it is amplified up to ≈5 J. The beam then takes a dual pass through a series of 9.4 cm disk amplifiers, is switched by a pockels cell, and then passes through a set of 9.4 and 15 cm disk amplifiers where it is amplified to its full energy (≈150J at shortest pulse). From here the beam passes into the Titan compressor where it is recompressed back to about 0.7 ps by a pair of 40x80 cm Multilayer Dielectric (MLD) diffraction gratings. The short pulse beam is then redirected by two turning mirrors before being focused with an f/3 off-axis dielectric parabola down to about a 7 μm full width half-maximum (FWHM) spot on target. Leakage light through the last two turning mirrors is directed into a number of laser diagnostics, including an equivalent plane monitor, an autocorrelator, and a prepulse monitor.

3.2 Laser Diagnostics

A number of laser diagnostics were fielded to carefully characterize laser conditions that may affect the interaction physics. These include the laser focal spot and pulse length, which together determine the laser intensity, and the preformed plasma scalelength, which defines the interaction plasma. The focal spot was measured with a 16-bit CCD camera with the laser at low power. A 2nd order autocorrelator was used to determine the pulse length, which was measured at 0.7±0.3 ps at shortest pulse. The preplasma was inferred by comparing the prepulse level determined with a fast photodiode to the plasma scalelength measured from interferometry using a 532 nm probe beam tangential to the target surface. Hydrodynamic simulations using the temporal profile of the prepulse trace were found to be consistent with the measured preplasma scalelength [84].

The laser interaction is affected by a prepulse that always precedes the main laser pulse, originating in the OPCPA due to Amplified Optical Parametric Fluorescence (AOPF). This prepulse is intense enough to ionize the target surface, causing the main pulse to interact with a preformed plasma instead of a solid surface. A typical trace from the monitor is shown in Figure 3-2. The prepulse levels on these experiments ranged from 5-80 mJ in a 3 ns pedestal from the AOPF and 1-30 mJ in a spike 1.4 ns ahead of the main pulse caused by stray reflections in the beamline. Simulations predict preplasma scalengths of up to 10 μm for the critical surface and 50 μm for $\frac{1}{10}$ critical.

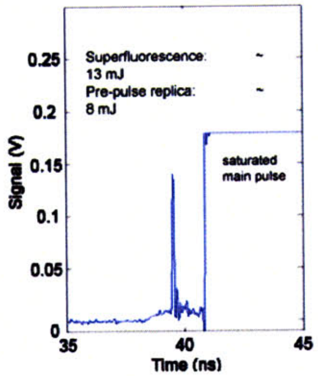

Figure 3-2: Prepulse trace from Titan. Typical prepulse levels ranged from 5-80 mJ in a 3 ns pedastal from spontaneous fluorescence and a 1-30 mJ parasitic short pulse 1.4 ns ahead of the main pulse. This figure is taken from MacPhee, RSI 2008[6]

3.2.1 Focal Spot & Pulselength Measurements

The initial laser alignment and focusing was done with an 8-bit camera focused on a wire that defines the target chamber center. With the laser at low power the parabola was adjusted such that the laser was focused on the camera focal plane. The laser spot was positioned at the tip of the wire, and the astigmatism in the beam was minimized. Once the laser was optimized, the focal spot was imaged with a 16-bit Apogee Alta U2000 camera through an anti-reflection (AR) coated fused silica window of the target chamber. The camera has a 1600x1200 array with 7.4x7.4 μm pixels and imaged the focal spot with a 66× magnification. The focal spot image is shown in Figure 3-3. If the elliptical FWHM of the focal spot is mapped onto a circular distribution of equal area, the focal spot diameter is 7 μm and contains 15% of the laser energy.

One concern in the focal spot measurement was that the low power focal spot was

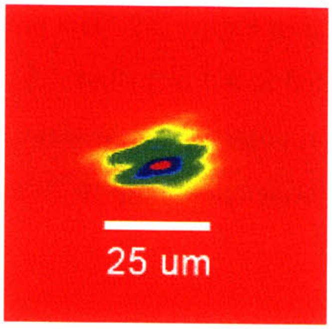

Figure 3-3: The Titan focal spot measured with the 16-bit camera. The mapping of the elliptical FWHM into a circle results in a diameter of 7 μm.

not representative of the on-shot focal spot, since the beam profile may be affected by the laser amplifiers at full energy. An Equivalent Plane Monitor (EPM) was set up to monitor the laser wavefront by focusing the leakage light through the final turning mirror before the target chamber. In these experiments, an f/3 diamond-turned gold parabola nominally equivalent to Titan's dielectric parabola was used to focus the beam. The focusing properties of the gold parabola were not as good as those of the dielectric parabola, however, and the inferred intensities from the focal spot were lower by an order of magnitude. In an experiment a few months after the ones described in this text the gold parabola was replaced with a 6.3 m f/22 focal length lens. The intensity distribution from this EPM on a full energy shot was compared to one at low energy (scaled to full energy). This is shown in Figure 3-4. Since the intensity distribution is the same at low and high energy, the focal spot imaged with the 16-bit camera at low power is representative of the focal spot on a full energy shot.

One additional issue in the focal spot determination is that the focal spot degrades over the course of a day due to thermal effects changing the index of refraction in the amplifier chain. The quantitative extent of the degradation is uncertain because this was measured with the gold parabola but is on order of a factor of 2-3 reduction in the peak intensity. Thus the focal spot distribution measured by the 16-bit camera is only reliable for the first shot of each day. In future experiments the EPM will monitor shot to shot variations in the focal spot and a deformable

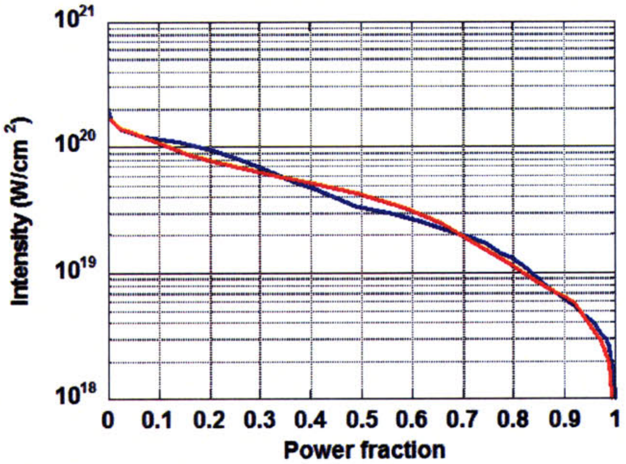

Figure 3-4: Comparison of the EPM intensity distribution for a full energy and low energy shot. The intensity distribution is generated from the focal spot distribution using 150 J total laser energy and a 0.5 ps pulselength. The blue line is the distribution at full energy and the red line is the distribution at low power using only the OPCPA.

mirror installed after these experiments will help correct the wavefront and reduce thermal degradation.

3.3 Hard X-Ray Bremsstrahlung Spectrometer

3.3.1 Spectrometer Description

The Hard X-ray Bremsstrahlung Spectrometer (HXBS) uses k-edge and differential filtering to discriminate the x-ray spectrum (up to 500 keV in the current filter configuration). The spectrometer consists of nine filters of increasing Z, from Al to Au, then four filters of 1 mm to 4 mm of Pb for differential filtering. A model of the spectrometer hardware and a diagram of the setup are shown in Figure 3-5.

The filters are 1 in^2 with a 250 μm sheet of Mylar taped to both faces to minimize the contribution of secondary electrons < 150 keV. Fuji BAS-MS image plates [85] are used as dosimeters. Image plates have high sensitivity and their spatial resolution allows for verification of diagnostic alignment. Image plates, however, are light sensitive and fade with time. Good procedural controls are thus extremely

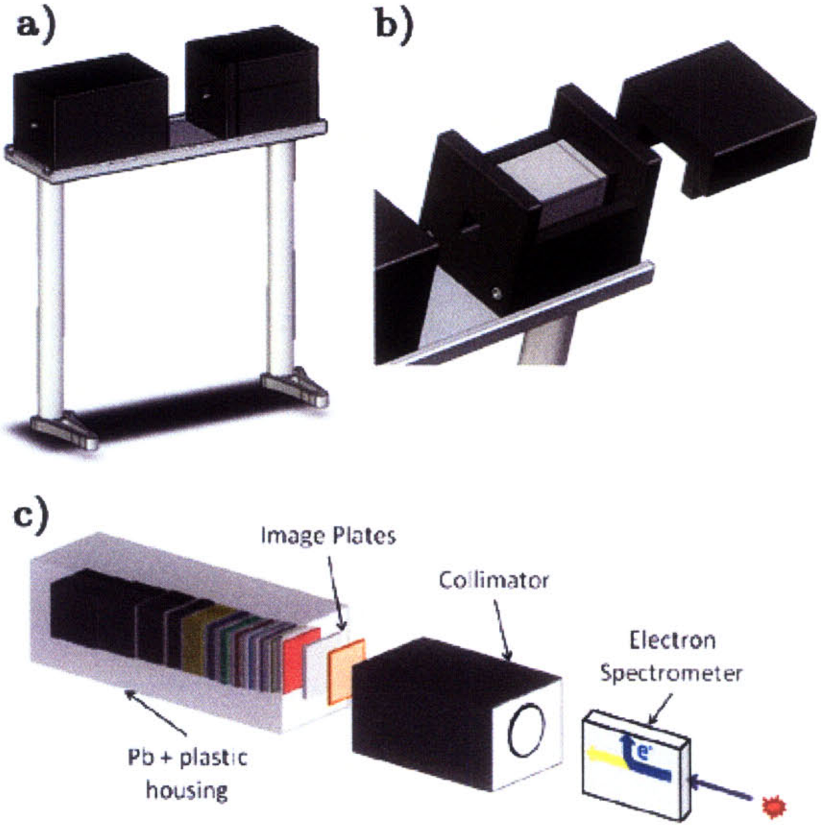

Figure 3-5: a) Spectrometer Overview. b) A black Delrin cartridge is contained in a Pb housing. c) Cartoon of the filters and spectrometer setup.

important for proper dosimetry. The image plate dosimeters are described in the following subsection.

The Titan target chamber is a high noise environment, with electrons and x-ray fluorescence coming from other diagnostics and the target chamber wall. Spectrometer shielding, collimation, and magnetic deflection are all necessary to prevent background contribution to the dosimeter signals. The image plates and filters are stacked in a 6 mm thick interlocking black Delrin cartridge loaded into a 1.8 cm thick Pb box, which shields up to 2 MeV photons. The Delrin cartridge allows for rapid loading and unloading of the spectrometers, is light-tight to preserve the image plate data, and reduces noise from scattered secondary electrons in the Pb shielding. A 12.5 cm long Pb collimator with a 1/2 in. diameter hole is also used to reduce noise from fluorescence off the vacuum chamber walls and diagnostics around the target by limiting the field of view at tcc to 5 cm. Additionally, an electron spectrometer was placed in front of the Bremsstrahlung spectrometer to deflect electrons escaping from the target.

A description of the HXBS and its use has been published by C.D. Chen, et. al. in *Review of Scientific Instruments*[86].

3.3.2 Implementation and Design History

The initial spectrometer design was adapted from R. Nolte[87], where thermoluminescent detectors (TLDs) held in PVC trays were used as dosimeters. TLDs are LiF chips which absorb radiation and emit photons proportional to the deposited dose when heated to a few hundred degrees centigrade. TLDs are commonly used in badge dosimeters around the world due to their durability, stability, and linearity across several decades of dose. A prototype design was initially fielded on Titan in April 2007, mostly copied from the Nolte design. The prototype used 3.2 mm x 3.2 mm x 0.089 mm TLD-700 chips made by ThermoFischer Scientific embedded in a Mylar spacer. During the experimental campaign, a failure of the TLD reader resulted in a switch to image plate dosimeters. Experience with both dosimeter configurations showed that image plates held some distinct advantages over the TLDs. First, since the image plates could be cut to the same size as the filters, they alleviated concerns over 3-D effects. In the first few channels of the spectrometer where the primary deposition is due to absorption of filtered x-rays by the TLD, this is not a significant concern. However, in the later channels where Compton scattered electrons contribute significant signal to the dosimeters, vacuum zones, air pockets, and the difference in electron transport properties of Mylar and LiF complicate the modeling of the spectrometer, especially if the spectrometer is not precisely aligned. The image plates also provide spatial resolution, allowing for verification of alignment and diagnosing of background noise issues.

A number of adaptations to the Nolte design were required for use in a petawatt environment. As discussed above, shielding, collimation, and magnetic deflection using an electron spectrometer were added to prevent contamination of the measured spectrum from x-ray fluorescence in the chamber and high energy electrons escaping the target. The original Nolte design includes a PVC/PMMA plastic absorber to stop electrons up to 1.5 MeV. In Titan, however, electrons up to several tens of MeV have been seen on vacuum electron spectrometers under these experimental conditions. During April 2007 and August 2007 Titan campaigns, an electron spectrometer was placed in front of the Bremsstrahlung spectrometer in order to measure the escaping electron spectrum along the same line of sight as the Bremsstrahlung signal. The electron spectrometer also served to deflect electrons from the Bremsstrahlung spectrometer.

Figure 3-6 shows the image plate scans of some of these effects. In Fig. 3-6a the electron contamination is evidenced by the "glow" around the dosimeter signals. There is no magnetic deflection, and the electron signal scatters more than the photon signal, resulting in rounder edges for the collimator throughhole. The electron spectrometer used in April 2007 and August 2007 had a very narrow slit for good energy resolution, along with a small alignment hole in the back. This limited the signal area on the Bremsstrahlung spectrometer as seen in Fig. 3-6b.

In the January 2008 Titan campaign a 6 mm square entrance slit was machined into

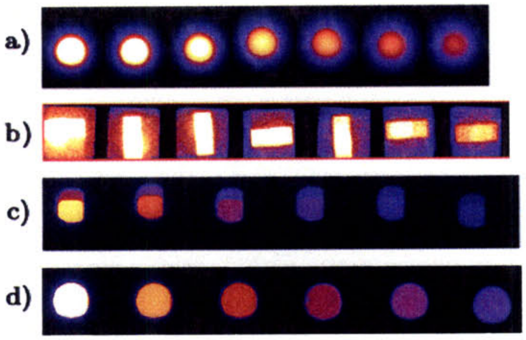

Figure 3-6: a) Electron contamination is evidenced by the "glow" around the dosimeter signals. b) The electron spectrometer's small front slit and rear alignment hole limit the signal statistics. c) The electrons are not fully deflected by the magnet, resulting in spatially separated electron and photon signals. d) A clean signal with no electron contamination has a sharp edge from the collimator.

the front plate of the electron spectrometer and the rear plate was removed. This larger slit degraded the energy resolution of the electron spectrum but increased the signal statistics of the HXBS. These signals are seen in Fig. 3-6c. Here, the electron spectrometer was at an insufficient distance to fully deflect the electron beam when the electron energies were up to 50-80 MeV. There are two distinct images of the front slit of the electron spectrometer, one from the displaced electrons and one from the straight through Bremsstrahlung. In Fig. 3-6d the electron spectrometer was swapped with a magnet with a large throughhole, allowing the full projection of the collimator to serve as usable signal. While the electron spectrometer's magnetic field was sufficient for deflecting electrons when placed at least 12" in front of the collimator, later a simpler magnet was used when the vacuum electron spectrum was unnecessary.

3.3.3 Image Plate Dosimeters

Image Plates [88] are reusable x-ray imaging detectors developed 25 years ago by *Fuji Photo Film Co.* for medical imaging. While designed as a substitute for medical x-ray film, they have been used in many scientific applications for their spatial resolution, linearity and dynamic range (over 5-6 decades), resistance to electromagnetic pulse, and reusability. The physical mechanism and operational methodology of the image plates are described by Thoms [89] and summarized here. The active layer of the image plate consists of a photostimulable BaFX:Eu^{2+} (X = Cl, Br, I) phosphor embedded in an organic binding. The phosphor is surrounded by a thin (10 μm) plastic protective coat and a ferrite/plastic base for support and magnetic adhesion. When the phosphor is exposed to ionizing radiation, electron hole pairs are generated. The holes migrate to the Eu^{2+} ions, forming Eu^{3+}. The electrons are trapped in F-centers (halide vacancies) in a metastable state. The image plates are then scanned using an image plate scanner, which uses a focused HeNe laser to excite the trapped electrons, causing them to emit blue light as they recombine with the holes. The blue photons are collected by a photomultiplier tube in the image plate scanner. This emission is digitized by the scanner in linear dose units called PSLs (PhotoStimulated Luminescence). After readout, any latent signal in the image plate is erased by a 20-30 minute exposure to an intense light source.

Two common types of image plates used in this work are the BAS-MS and BAS-SR plates, part of Fuji's Biological Analysis System (BAS) series. The BAS-MS is a white plate, where MS stands for maximum sensitivity, and are the ones used in experiments described here. The BAS-SR (super resolution) has a blue dye in the phosphor layer which increases resolution by reducing the scattering of the scanner laser light and the emitted blue photons. The tradeoff is a factor of three lower sensitivity, which can be useful in higher fluence environments such as OMEGA-EP or NIF.

The chemical composition of the image plate is important in modeling the response of the spectrometer. Since the image plates and filters are used in series, both the absorption and transmission characteristics are important. While the phosphor layer composition is known, the composition of the plastic and ferrite layers is not readily available, and somewhat vague and contradictory. Three sources of information were used to compile an estimate of the composition: information from the USA Fuji Life Sciences website, FAQs from the Fuji-Japan English website, and information supplied by Fuji sales representatives. This synthesis of the composition data is

analyzed and summarized in an internal LLNL memo attached as Appendix A.
The trapped electrons can also spontaneously escape from the F-center and therefore the image plate readout fades with time. Because of the thermal energy distribution, the fade rate is also temperature dependent. If the image plates are scanned at different times after a shot, the signal needs to be renormalized with a fade curve. This fade curve has been measured for Titan ambient temperature conditions and will be described in the following calibration subsection.
The image plate scanner model used in these experiments was a Fuji FLA-7000. There are three adjustable parameters on the scanner, the *sensitivity* (s1000, s4000, s10000), the *resolution* (25, 50, 100, 200 μm), and the *latitude* (L4, L5), which is related to the dynamic range of the photomultiplier tube. The scanner outputs readings in data units called "Quantum Levels" which are logarithmic units dependent on the sensitivity and latitude settings. The Quantum Levels need to be converted to PSLs using the Fuji supplied formula

$$\mathrm{PSL} = \left(\frac{\mathrm{Resolution}}{100}\right)^2 \times \frac{4000}{\mathrm{Sensitivity}} \times 10^{\mathrm{Latitude} \times \left(\frac{QL}{G} - \frac{1}{2}\right)}, \tag{3.1}$$

where G is the Gradiation which depends on the bit depth setting, and is G=255 for 8 bit output and G=65535 for 16 bit output. This calculated PSL level is linearly proportional to the deposited dose. One additional factor is that the scanner's HeNe laser spot is ≈70 μm and larger than some of the resolution step sizes and therefore erases signal as the plate is read. Scans at different resolutions need to be scaled for this effect. All scans in this work were done at 100 μm resolution.

3.3.4 Monte Carlo modeling w/ ITS sensitivity curves

The response of the filter stack, including the Teflon absorber, filters, Mylar spacers, and each image plate layer has been modeled with the 1-D Monte Carlo TIGER code from the ITS 3.0 package. The Delrin enclosure and the Pb shielding are not included in the model, as they do not contribute to the image plate signal. The set of filters used in the HXBS is shown in Table 3.1. The Teflon layer functions solely

Table 3.1: Filters used in the Bremsstrahlung Spectrometer.

Layer	Material	Thickness
0	Teflon	5 mm
1	Al	100 μm
2	Ti	100 μm
3	Fe	100 μm
4	Cu	100 μm
5	Mo	100 μm
6	Ag	150 μm
7	Sn	500 μm
8	Ta	500 μm
9	Au	1.58 mm
10	Pb	1.143 mm
11	Pb	2.272 mm
12	Pb	3.372 mm
13	Pb	4.473 mm

as an electron absorber and does not have an image plate behind it.

A Spectrometer Response Matrix (SRM) is built up from 150 simulations of narrow bin photon spectra launched into the filter stack. The 150 photon spectral bins are logarithmically spaced from 1 keV to 100 MeV, and the incident spectrum in each run is uniformly distributed between the two bin edges. Since the energy bins are narrow, this is equivalent to using monoenergetic photons. However, monoenergetic photon inputs can introduce error near the absorption peaks of the image plate phosphor, and using a spectral input averages over the changing absorption and is more representative of the expected spectrum. This calculated spectrometer response is shown in Figure 3-7.

Each of the 13 lines corresponds to the deposited dose in the image plate active layer behind the respective filters. Each channel starts to pick up signal at a different energy and the response edge is defined at 10^{-4} MeV/photon, which is $\approx \frac{1}{10}$ of the average response level. The filter thicknesses in the legend are the nominal filter thicknesses, compared to the actual measured thicknesses in Table 3.1. This thickness difference was initially a significant source of error when compared to the experimental calibration and has since been corrected.

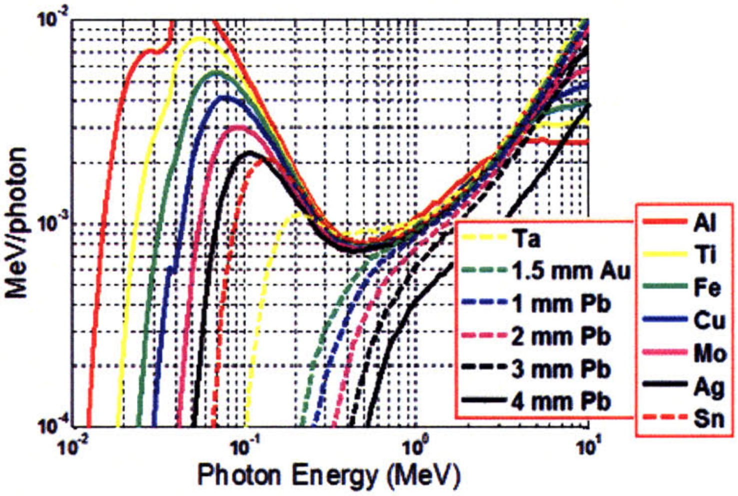

Figure 3-7: Spectrometer channel response calculated from ITS 3.0. Each curve represents the energy deposited in that layer by the photon spectrum. For the 13 channels this forms a 13×150 spectrometer response matrix (SRM).

3.3.5 Experimental Calibration

The HXBS was calibrated over the 15-85 keV energy range and at 662 keV. These calibrations were done at two facilities: the High Energy X-ray (HEX) facility at National Security Technologies, LLC (NSTec) in Livermore, CA, and the Radiation Calorimetry Laboratory (RCL) at Lawrence Livermore National Laboratory in Livermore, CA. The HEX facility produces k-shell line emission by photopumping fluorescent foils with a Yxlon x-ray source (160 kV onto a Tungsten target). For fluorescors from Cu to Pb this provides line emission in the 8 to 85 keV range. The RCL houses a 254 Ci Cs-137 source which emits a 662 keV photon. This section describes these two calibrations.

HEX calibration

The HXBS was exposed to 11 fluorescent foils from Zr to Pb, spanning the energy range of 15-85 keV. The fluorescors, filters, and line energies are summarized in Table 3.2. The emission spectrum was measured before and after each exposure with a Canberra high-purity germanium detector which had been previously calibrated with NIST traceable radioactive sources (Fe-55, Cd-105, Gd-153, and

Table 3.2: Fluorescors and line emission at HEX

Fluorescor	Filter	kα1 line (keV)	kβ line (keV)
Zr	Zr	15.7	17.7
Mo	Zr	17.5	19.6
Ag	none	22.2	24.9
BaO	Sm	32.2	36.4
Sm	Sm	40.1	45.4
Dy	Dy	46.0	52.1
Er	Dy	49.1	55.7
Ta	Ta	57.5	65.2
Pt	W	66.8	75.7
Au	Au	68.8	78.0
Pb	Pt	75.0	84.9

Am-241). The emission spectrum includes the kα1, kα2, and kβ lines on top of a Bremsstrahlung background, and is measured just behind the spectrometer housing with the housing removed but collimator still in place.

The HXBS exposures were limited to 60s in order to minimize fading effects. The image plates were scanned on the same Fuji FLA-7000 image plate scanner used in the experiments. The scanner was transported to the HEX facility and the scanner calibration checked with a C-14 source to ensure equivalent functionality. The scanner calibration parameters were a scan time exactly 30 minutes after the start of exposure, and scanner settings of 100 μm pixel size, s4000 sensitivity, and L5 dynamic range.

The spectrometer signals were compared to a Monte Carlo model of the spectrometer response, accounting for appropriate distance, air transmission, and Canberra quantum efficiency factors. Since the HEX spectrum is primarily line emission, a modified response matrix was calculated where the spectrometer response to monoenergetic photons is used for the line emission and the narrow bin spectral response described above used for the Bremsstrahlung background. The physical model is otherwise the same. The model predictions match up quite well with the calibration, as seen in Figure 3-8. In this figure the data points are the measured dose on the image plates and the solid lines represent the predictions of

Table 3.3: Calibration factors from HEX and RCL

Fluorescor	kα1 line (keV)	Calibration Factor (MeV/PSL)
Zr	15.7	2.0
Mo	17.5	1.6
Ag	22.2	1.6
BaO	32.2	1.6
Sm	40.1	2.1
Dy	46.0	2.0
Er	49.1	1.9
Ta	57.5	2.0
Pt	66.8	3.8
Au	68.8	1.8
Pb	75.0	2.0
Cs-137	662	2.1

the Monte Carlo model. The energies listed in the legend are the kα1 line energies. Some of the exposures include both kα and kβ and others are filtered for just the kα line. The 662 keV data point from the RCL Cs-137 exposure is also included. The response is scaled to show multiple lines on the same plot.

The model predictions are scaled to best fit the data and determine a PSL to energy calibration factor. For the measured PSL levels to be proportional to the calculated deposited dose, these calibration factors, in units of MeV/PSL, must be the same for every calibration point. These calibration factors are shown in Table 3.3.

The error bars on the calibration factors are ±0.3 MeV/PSL. Almost all of the calibration factors are about 2.0 MeV/PSL. The Pt line is high at 3.8 MeV/PSL but is most likely an outlier. There is no physical reason for the difference and the surrounding points are all lower. It is most likely due to an incorrect setting of the HEX fluence rate as it is exactly a factor of two off from the other points. The three points around 18-32 keV are all low at 1.6 MeV/PSL. These low points, however, are most likely due to issues with the Canberra calibration rather than a real difference in the spectrometer response. The quantum efficiency curve measured by NSTec for the Canberra detector has a large scatter around these energies and the fitted quantum efficiency used to calculate the input spectrum has a large discontinuity. The discontinuity in the quantum efficiency would bring these three

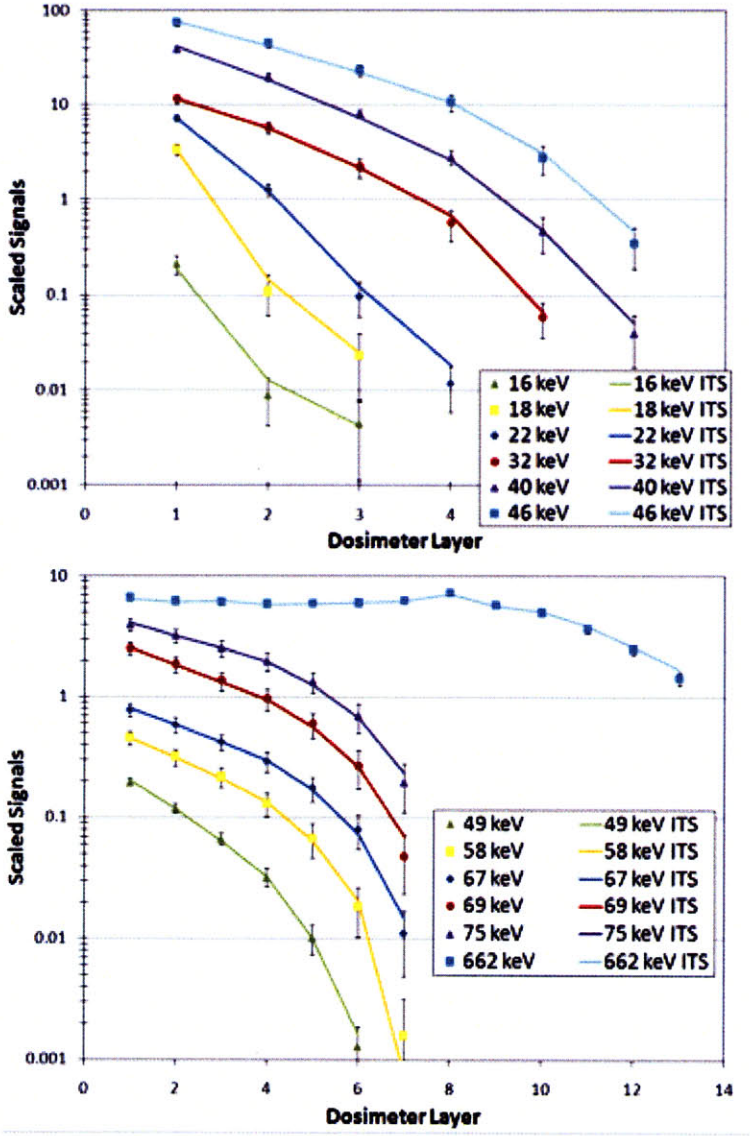

Figure 3-8: Calibration of the Hard X-ray Bremsstrahlung Spectrometer. The spectrometer was exposed to different fluorescent foils. The data points are the measured dose on the image plates. The solid lines represent the predictions of the Monte Carlo model. The energies listed are the kα1 line energies. Some of the exposures include both kα and kβ and others are filtered for just the kα line. The 662 keV data point represents the Cs-137 calibration at RCL. The response is scaled to show multiple lines on the same plot.

calibration factors back in line with the other data. On this basis these four calibration factors are excluded and the rest are averaged to obtain an absolute calibration of 2.0±0.1 MeV/PSL.

RCL calibration

The RCL houses a Shepherd model 81-12 beam irradiator which contains a 254 Ci Cs-137 source (calibrated Oct 2008). The Cs-137 source emits a 662 keV photon through beta decay, providing a high energy data point. There is also x-ray emission up to 30 keV and electron emission at 0.5 and 1.2 MeV. The front of the HXBS assembly was placed 374 cm away from the source housing. A 1/16" Pb sheet was placed halfway between the source and spectrometer in order to filter the low energy x-rays while minimizing fluorescence. Additionally, a 1/4" sheet of polycarbonate was placed in front of the source to range out the electron emission.

The HXBS was exposed about 15 times for 30s each and scanned between 20 minutes and 140 minutes (including the 30 minute reference) after the exposure in order to build up a fade curve for the image plates. The spectrometer response was also compared to a line emission Monte Carlo model of the HXBS. The model comparison was shown along with the HEX calibration in Figure 3-8. Figure 3-9 shows the fade curve for the image plates as a function of time, normalized to the 30 minute reference scan. Each data point is the average of the ratios of the 13 channels to the 30 minute reference (the averaged ratios were all consistent). The fade curve is also split in two portions, with an inflection point around 60 minutes. This fade curve was used to normalize the Titan experimental data to the 30 minute reference calibration when it was logistically infeasible to scan at exactly 30 minutes after a Titan shot.

3.3.6 HXBS analysis

The full analysis of the HXBS data is tightly coupled to modeling of the target and will therefore be discussed in the next chapter. This subsection describes the initial

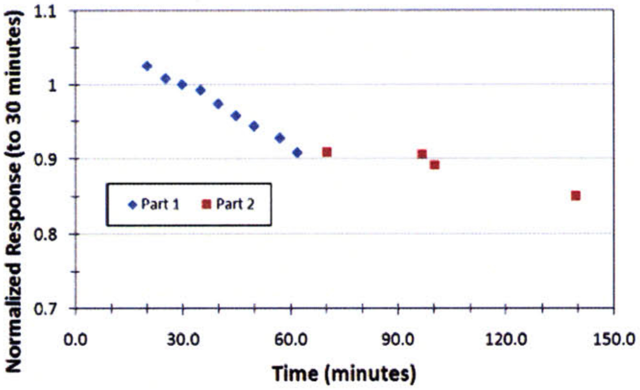

Figure 3-9: Image Plate fade curve. Each data point is the average of the ratio of the 13 spectrometer channels to the 30 minute reference. The fade curve is split in two parts with an inflection point around 60 minutes.

data processing of the spectrometer signals. After each shot, the image plate stack is disassembled in a dark room and scanned 30 minutes after exposure using the scanner settings: *s4000, 100 μm, L5.* Each spectrometer is scanned separately and scan times from a system synchronized clock are noted for the fade correction. This results in a scanned image of the 13 plates with a projection of the collimator hole on each one. Figure 3-10 shows a sample of six of these channels.

For each of the IP channels the mean PSL is taken as the signal level for that channel. The error in the signal level for each channel is quantified as the quadrature addition of 3 different parameters: the standard deviation in each channel, the gradient across the projection, and a standard 3% response variability in the image plate. The standard deviation about the mean in each channel is related to the uniformity of the dose and thus the statistics of the deposition. The gradient is taken as the difference in the mean across different parts of the image (away from the boundary) and is a measure of 3-D effects in the spectrometer modeling. The 3% image plate response variability is seen in shot to shot calibration exposures.

The signals and errors from each of the spectrometer channels, together with the Monte Carlo modeled SRM constitute a few channel spectrometer problem. The x-ray spectrum can be unfolded with a number of techniques, such as fitting test distributions, Maximum Entropy Methods, or Singular Value Decomposition. Some

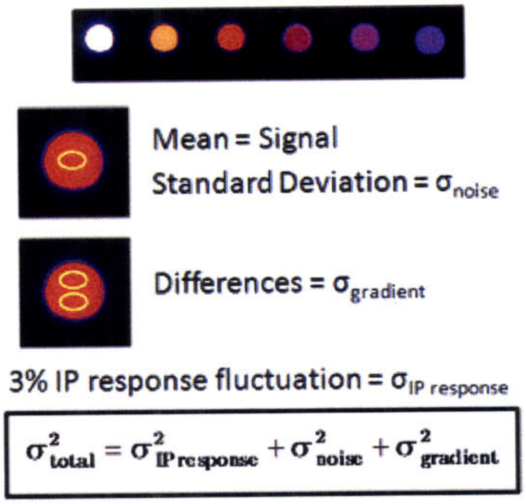

Figure 3-10: Data extraction from the HXBS channels. The mean signal in each channel is taken as the PSL signal value. The error bar on each channel is quadrature sums of the standard deviation in each channel, the gradient across the channel, and a 3% image plate response variation.

of these techniques have been explored in the analysis of other data using this instrument. For the purposes of this work the electron spectrum is more interesting than the exact Bremsstrahlung distribution. The electron to Bremsstrahlung mapping is derived from a series of Monte Carlo simulations of the target, generating multiple Target Response Matrices (TRM) for different simulation parameters. These simulations and the estimates of the electron spectra will be described in the next chapter.

3.4 Single Hit Spectrometer

Single photon counting is an established technique in short-pulse laser experiments for measuring absolute line emission from targets [4], [90], [91]. The Single Hit Spectrometer is simply a charged coupled device (CCD) camera facing the target operating in single photon counting mode. When appropriately filtered such that only a small percentage of the pixels are exposed to photons, a histogram of the pixel counts correlates linearly with the x-ray spectrum. This picture is a simplification; in practice, the deposited charge spreads into adjacent pixels, gamma emission from the target produces noise and fluorescence from within the camera, and crowding effects complicate the analysis and calibration of the detection efficiency. The spectrometer is described below, along with operational factors and data analysis procedures.

3.4.1 Spectrometer Description

The camera used in these experiments was a Spectral Instruments model 800 CCD (SI800-116) with a 2048x2048 EEV CCD chip (13.5 μm pixels, 16 μm thick, backilluminated). The spectrometer layout is shown in Figure 3-11. The camera is placed 541 cm away from the target and pointed by retroreflecting an alignment laser through the target and the center of a Pb collimator on the chamber port. Since the chamber radius is about 1 m, there is a 4.4 m air gap between the target and the CCD. For 8 keV Cu kα measurements, the attenuation length is 90 cm in air. A vacuum tube to displace the air gap is thus necessary to prevent a reduction in the signal to noise. A Cu filter is used to attenuate the signal into the single photon regime. The spectrometer is also contained in a 2" thick Pb housing to reduce background fluorescence from the rest of the room. Previous experiments [90] have shown that a 5 cm thick Pb housing can dramatically reduce the fluorescence from structures around the CCD. To minimize the dark current, the camera is cooled to $-40\,^{\circ}$C using a thermoelectric cooler and water chiller.

3.4.2 Analysis Algorithms and Calibration

X-rays that interact with the CCD can deposit their energy in one or more pixels, termed "single events" or "split events," respectively. Because of these split events, a direct histogram of the counts on the CCD does not reflect the incident x-ray spectrum. There have been many different algorithms developed to sum these split events through techniques such as pattern matching and boundary detection. The simplest and most established procedure, however, is to ignore the split events and

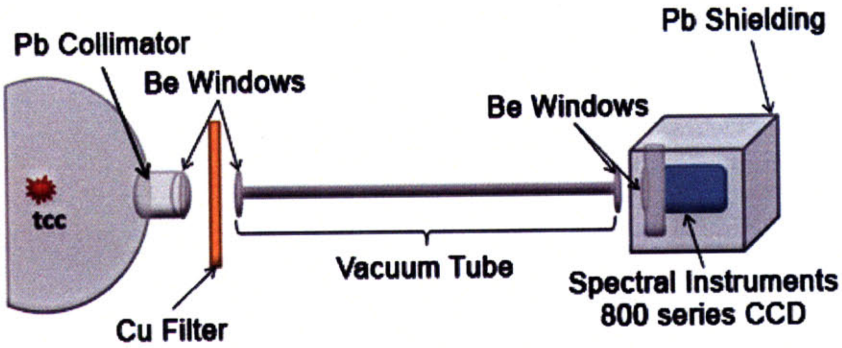

Figure 3-11: Layout of the Single Hit CCD spectrometer. The spectrometer is 541 cm from target chamber center (tcc) and looks through a steel vacuum tube, Cu filter, and a Pb collimator. The vacuum tube prevents attenuation of the Cu kα signal in air. The spectrometer is contained in a 2" thick Pb housing to reduce the background signal.

use a detection efficiency curve calibrated for single events. This "Single Event algorithm" scans through a background subtracted CCD image and finds pixels whose brightness is above the surrounding 8 pixels by some threshold level, taken here as 98% of the signal in the central pixel. Only these single events are included in the histogram. Figure 3-12 shows a sample subsection of a CCD image and the Single Event histogram derived from this image. The x-axis on the histogram has been scaled from counts (deposition counts vs histogram counts) to the energy of the incident photon. This scale factor depends on the camera gain and is empirically determined by scaling to known line energies. The Cu kα and kβ lines are seen in the histogram.

The calibration of the detection efficiency to translate the histogram into an absolute k-shell yield involves determining 3 factors: the quantum efficiency of the CCD, the single hit probability of a photon, and a crowding correction as the single event algorithm starts to reject single events with increasing CCD exposure. The calibration of this specific camera is described in further detail by Maddox [7] and is summarized here.

The camera was calibrated at 5.9 keV and 22 keV using Fe-55 and Cd-109 sources. The source activities were measured using an AmpTek XR100-CR Si detector and

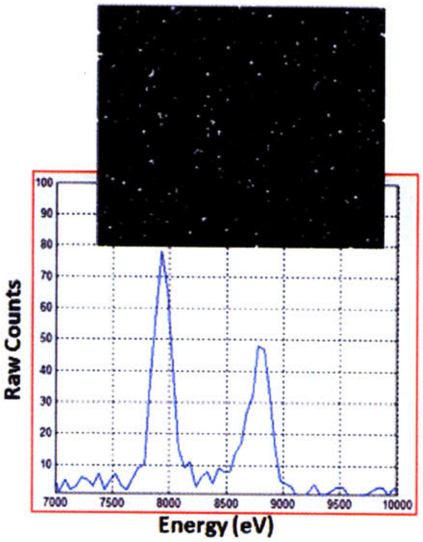

Figure 3-12: A sample subsection of a CCD image and the Single Event histogram from the image. The counts on the x-axis have been scaled to the energy of the incident photon. The Cu kα and kβ lines are seen in the histogram.

an AmpTek MCA8000A multichannel analyzer to within 10% of the specified activity. The dose was varied over 2 decades of CCD exposure levels by varying the exposure time and the distance of the CCD to the source. The images were then analyzed with the single event algorithm and the detected photons compared to the source fluence. Figure 3-13 shows the calibration curve from Maddox for the 5.9 keV photon exposure. The black squares and red triangles represent the detection efficiencies for 5.9 keV photons using a standard histogram and single event algorithms, respectively. The detection efficiencies are plotted against the chip exposure level. The exposure level is defined as the fraction of pixels above a background threshold, taken here as 3 times the half width at half maximum (HWHM) distribution of the dark image.

The detection efficiency is more stable for the standard histogram as the chip exposure level increases. However, the standard histogram does not reflect the actual x-ray spectrum, complicating the subtraction of the bremsstrahlung background to obtain a k-shell signal. In addition, the k-shell peaks are often indistinguishable among the split events of the higher energy background. The

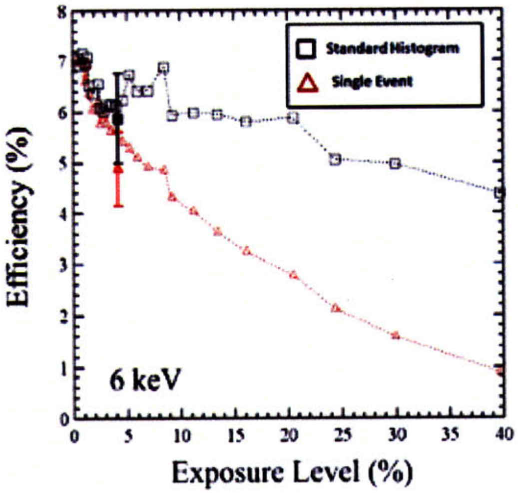

Figure 3-13: Detection efficiency calibration for 5.9 keV photons as a function of the chip exposure level. The standard histogram provides a stable detection efficiency but the single event algorithm needs to be corrected for chip crowding. Taken from Maddox RSI 2008 [7]. Reprinted with permission. Copyright (2008) by the American Institute of Physics.

single event algorithm can obtain a real spectrum but must be corrected for chip crowding as seen in the detection efficiency curve. One assumption in the crowding correction is that crowding due to monoenergetic photon exposure from the calibration is similar to crowding due to the spectrum of hard x-rays and fluorescence of surrounding material in a real high intensity laser experiment. This is a statistically reasonable assumption based on the algorithm but has not been experimentally verified.

The detection efficiency calibration shown is for 5.9 keV. To obtain the detection efficiency curve for 8 keV Cu kα, the quantum efficiency and single hit probability must be scaled from 5.9 keV. Since the range of 10 keV electrons (1.5 μm) in silicon is much smaller than the 16 μm pixel size, the single hit probability is assumed to be constant from 5.9 keV to 8 keV. The detection efficiency thus only needs to be scaled by the ratio of the absorption probabilities, which for these 2 energies is a 48% correction. From this calibration, the uncertainty in the detection efficiency is 15%. Coupled with a 10% uncertainty from the algorithm and background subtraction, this leads to a 20% error bar in the Kα measurement.

3.4.3 Sample Analysis

This subsection describes in detail the analysis procedure used to determine the k-shell yield from the CCD image. Figure 3-14 shows the raw CCD image from a experimental exposure. A background image consisting of the integrated dark current from the CCD is first subtracted from the raw CCD image using ImageJ [92]. The circular subsection of the single hit points represents the open path of the vacuum tube, whose diameter was just slightly smaller than required. Since the chip was not fully exposed, only a subsection of the image is used in the analysis. The yellow line traces out the subimage that is used. The rest of the image is blanked out and the number of pixels in the subimage is calculated to determine an effective chip area.

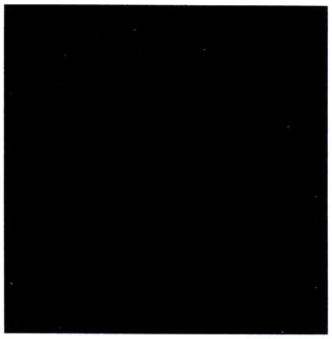

Figure 3-14: The raw image from the camera CCD. The circular subsection is the open path of the vacuum tube, whose diameter was just slightly smaller than required. The yellow line traces the subimage that is used in the analysis.

The subimage is processed with the single event algorithm and a histogram is taken of the result. This histogram was shown in Figure 3-12. An exponential is then fit to the background points around the peaks and subtracted from the histogram. An integration under the kα and kβ peaks provides the total detected k-shell counts. The total k-shell yield per steradian from the target is then obtained by factoring in the detection efficiency, solid angle (adjusted for the subimage), and filter/air/window transmissions using Equation 3.2.

$$N_{k\alpha}(\text{per SR}) = \frac{\text{Counts}_{k\alpha}}{\epsilon_{\text{det}} T_{\text{filters}} \Omega_{\text{subimage}}}, \tag{3.2}$$

where ϵ_{det} includes the quantum efficiency, single hit probability, and crowding correction as described above, T_{filters} includes the transmission of the Cu foil, beryllium windows, and air gap, and Ω_{subimage} is the solid angle of the chip, adjusted for the subimage area. This yield does not factor in the x-ray opacity of the target itself, which depends on the CCD view angle and the distribution of the source. For an absolute k-shell yield this is a necessary calculation. However, in the context of this work, the k-shell yield is compared to simulations where the calculated photons must also escape the target. The opacity correction is therefore already factored into the simulation and the measured yield can be directly compared. These comparisons will be discussed further in the following chapter.

Chapter 4

4.1 Experimental Overview

Experiments were conducted on the Titan laser at Lawrence Livermore National Laboratory to probe the spectrum and conversion efficiency of the laser generated hot electrons and test the intensity scaling laws. The targets were 1 mm × 1 mm planar foils, consisting of a 25 μm Cu fluor sandwiched between 10 μm Al at the front surface and 1 mm Al at the back. The 10 μm Al front layer prevents heating of the fluor and provides a consistent interaction surface across different types of targets. Previous spectroscopic studies [93] have shown that a Ni fluor buried under a few microns of Mo does not heat up appreciably, even when irradiated by lasers with higher energy and intensity (400 J, 5×10^{20} W/cm^2) than those used here. The 1 mm Al back layer ranges out electrons to prevent multiple passes through the fluor ("refluxing") due to buildup of the electrostatic potential as electrons escape. The target is shown in Figure 4-1.

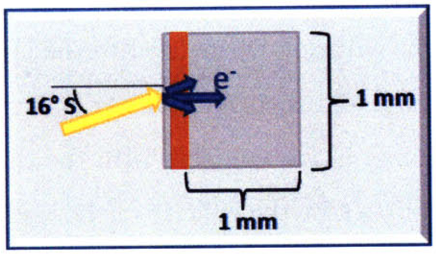

Figure 4-1: A 10 μm Al layer prevent heating of Cu fluor. The 25 μm Cu layer emits K-shell photons and serves as an electron counter. The 1 mm Al back layer ranges out electrons to prevent multiple passes through the fluor.

The targets were irradiated at 16° off-normal s-polarization with 5 to 150 J of laser energy for peak intensities of 3×10^{18}-8×10^{19} W/cm^2. Bremsstrahlung emission produced in the bulk was measured using two Hard X-ray Bremsstrahlung spectrometers at rear target normal and at 23° horizontal to rear target normal, about 80 cm from the target. A Spectral Instruments SI-800 CCD operating as a Single Hit Spectrometer was used to measure the K-shell emission from the buried Cu layer at 24° horizontal to the front target normal. Other ancillary diagnostics included a Kα Bragg crystal imager for imaging the fluorescence spot, vacuum electron spectrometers for measuring the escaping electron spectrum, and a Highly Oriented Pyrolytic Graphite (HOPG) mosaic crystal spectrometer for relative Cu spectroscopy. Laser diagnostics included a 16-bit CCD for measuring the focal spot, a fast diode prepulse monitor, and a 532 nm probe beam for inferring the preformed plasma. A schematic of the diagnostic layout for this experiment is shown in Figure 4-2.

4.2 Data Summary

There were ten shots on Al/Cu/Al targets in this data series. The raw data from the instruments and the data processing was described in Chapter 3. Table 4.1 lists the shot parameters for each of the ten shots. The data from the Bremsstrahlung spectrometer and Single Hit Spectrometer was processed as described in Chapter 3. The Kα data from the Single Hit Spectrometer is plotted in Figure 4-3. The absolute emission in photons/SR is represented by the blue diamonds and scales with the laser intensity. The emission normalized to the laser energy in units of photons/SR/J is shown in red and is constant across this intensity range. This shows that the primary scaling in Kα emission with the laser energy. (These numbers have not been adjusted for the opacity of the target.) Note that the right axis is on a linear scale. The measured Kα emission has a shot to shot variation of up to 30%, which is seen in all of the buried fluor experiments. The source of this variation is currently the subject of active research.

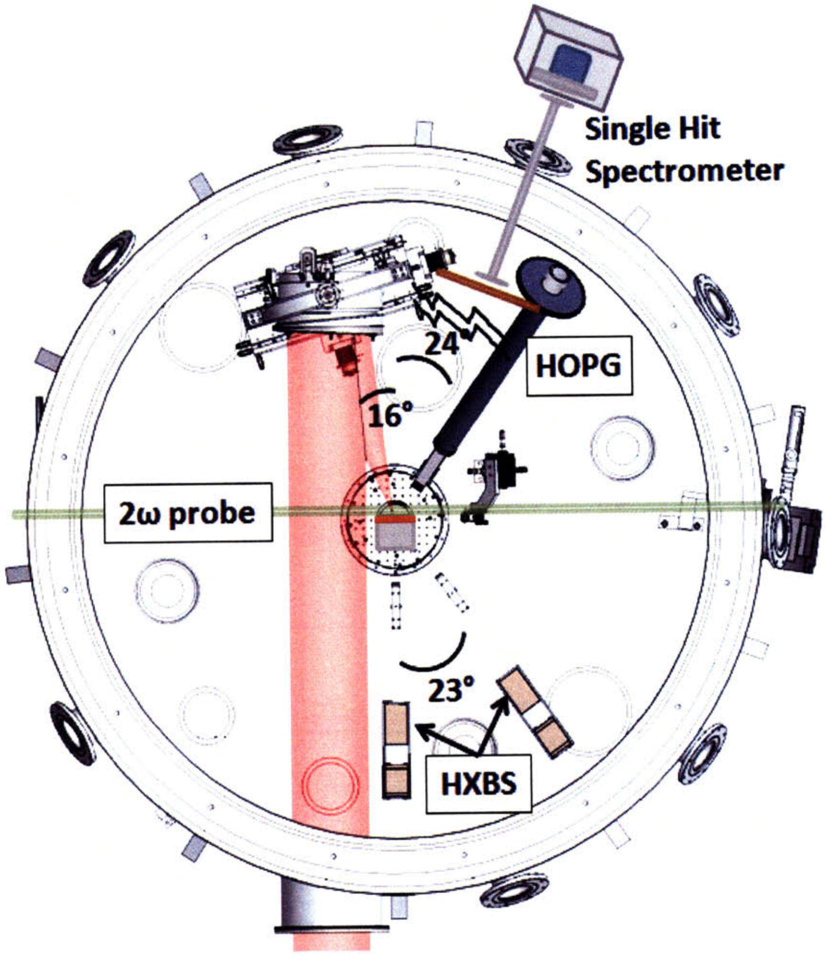

Figure 4-2: Schematic of the Diagnostic Layout

Table 4.1: Shot Parameters for Al/Cu/Al shots

ShotID	Laser Energy (J)	Intensity (W/cm^2)	LA Dist (mm)	TN Dist (mm)
20080122s01	121	6.7×10^{19}	821	764
20080122s02	81	4.5×10^{19}	821	764
20080122s03	36	2.0×10^{19}	821	764
20080124s02	18	1.0×10^{19}	821	764
20080129s07	120	6.7×10^{19}	750	N/A
20080130s04	123	6.9×10^{19}	750	850
20080131s04	143	8.0×10^{19}	750	850
20080131s05	13.5	7.5×10^{18}	750	N/A
20080131s06	4.7	2.6×10^{18}	750	850
20080131s07	57	3.2×10^{19}	750	N/A

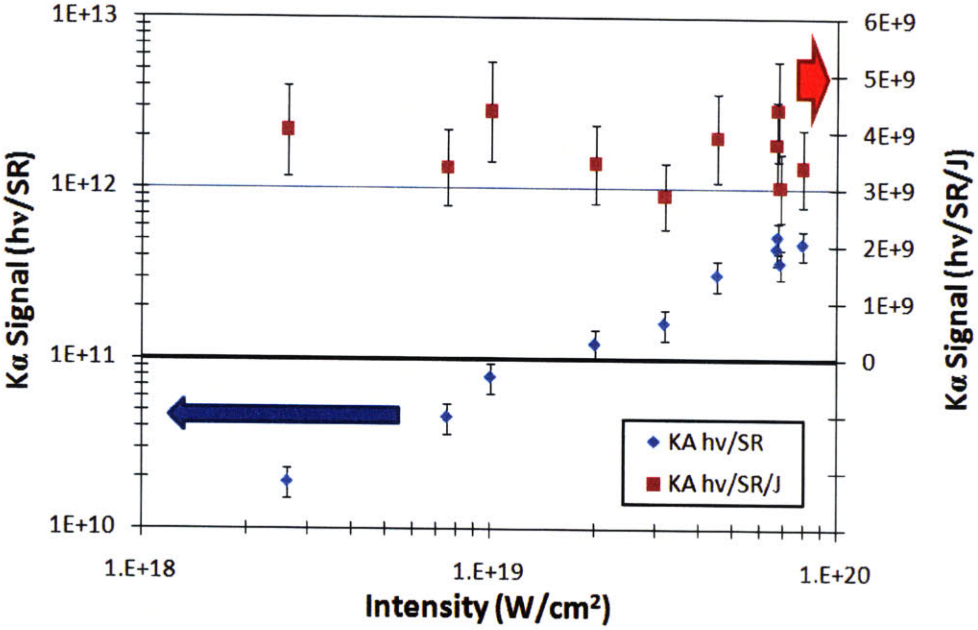

Figure 4-3: Kα data from the Single Hit Spectrometer. The emission in photons/SR is given by the blue diamonds and scales with the laser intensity. The emission normalized to the laser energy is shown in red and is constant across this range, which shows that the Kα signal primarily scales with the laser energy. These numbers have not been adjusted for the opacity of the target. Note that the left axis is logarithmic while the right axis is linear.

The raw dosimeter signals from the target normal Bremsstrahlung spectrometer are shown in Figure 4-4 for two shots of similar energy (121 J and 123 J). The signals and errors were extracted from the scans of the image plate dosimeters as discussed in Chapter 3. (This data has not been corrected for fade time, but for these two shots the difference is only on the order of a few percent.) The low energy component up to the 6th channel (response threshold = 70 keV) is almost exactly the same. The higher energy channels are lower for the 123 J shot. The impact of this shot to shot variation on the inferred electron spectrum will be discussed later.

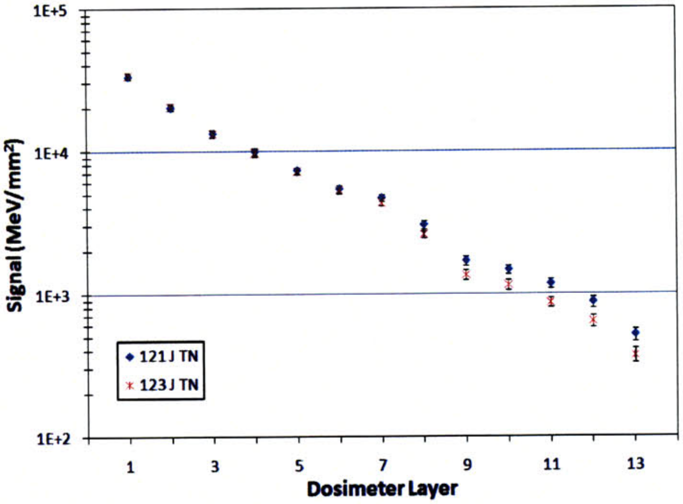

Figure 4-4: The raw image plate dosimeter signals are shown for the target normal Bremsstrahlung spectrometer for two shots of similar energy (121 J and 123 J). The low energy component up to the 6th channel is almost exactly the same but the higher energy channels diverge by up to 30%.

The slope of the Bremsstrahlung spectrum can be visualized through signal ratios of the different dosimeter channels. Figure 4-5 shows the signal ratio of channel 3 to channel 6 (S_3/S_6) and the signal ratio of channel 11 to channel 6 (S_{11}/S_6). The response threshold for channels 3, 6, and 11 are 25 keV, 50 keV, and 300 keV, respectively. S_3/S_6 is highest at low intensity and falls off, as expected for an increasing spectral temperature. S_{11}/S_6 is small at low intensity and increases with the laser intensity, also in accordance with an increasing spectral temperature. The S_{11}/S_6 ratio from the 123 J shot shown in Figure 4-4 is abnormally low when compared to the trend for the rest of the data shots and may be an outlier. The raw signal ratios for the rest of the data show a clear trend toward increasing spectral temperature for higher laser intensities. Unfolding the electron spectra from the dosimeter data, however, requires significant modeling effort to understand the Bremsstrahlung production and the spectrometer response to the Bremsstrahlung emission. This will be discussed in the following sections.

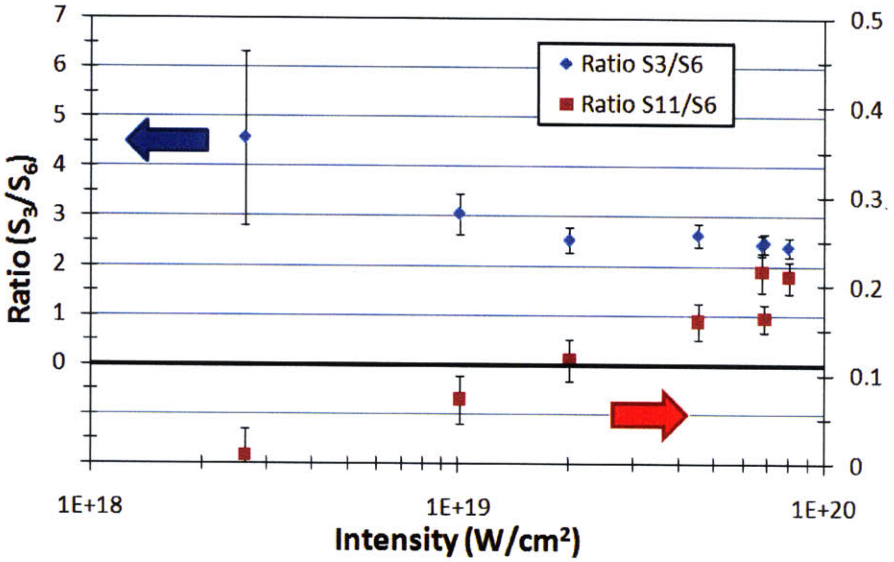

Figure 4-5: Ratios of the raw dosimeter data for different channels are plotted. The ratio of S_3/S_6 decreases with increasing laser intensity. The ratio of S_{11}/S_6 increases with laser intensity, as expected for higher spectral slope temperatures.

4.3 Target Simulation

The Bremsstrahlung and Kα emission from the target is modeled in 3-D using the ACCEPTP code from the ITS 3.0 package. Analogous to the modeling of the Bremsstrahlung spectrometer, 81 narrow spectral bins of electrons logarithmically spaced from 10 keV to 100 MeV are injected at the target surface in a 30 μm spot. The electron beam directionality and electron cone angle are variable parameters in the simulation. The beam direction is varied between 0° and 16°, consistent with experiments by Santala et al. [94] who found that the beam direction varied between target normal to along the laser axis depending on the preformed plasma scale length. The electron cone angle was assumed to have a distribution based on the classical electron ejection angle of electrons in a laser field [39] given by

$$\theta_{\text{half}} = \tan^{-1}\left[\left(\frac{2}{\gamma - 1}\right)^{1/2}\right], \tag{4.1}$$

where γ is the relativistic γ of the electron as discussed in Chapter 2. This assumption follows work by Stephens et al. [95], where images from buried fluorescent foils showed a broad 70-100 μm Kα spot up to 100 μm depth, followed by a 40° (full) divergence angle. From Monte Carlo simulations the assumption of the classical ejection angle was consistent with Kα spot sizes measured by Stephens. For reference a constant 40° full cone angle response was also simulated. Recent hybrid-PIC simulations by Honrubia and Meyer-ter-Vehn [96] have found that initial electron cone angles consistent with the classical ejection angle reproduced mean divergence angles of 30-40° seen in experiments due to magnetic collimation effects. The net propagation angle in Monte Carlo simulations is not collimated by field effects so the initial cone angle is expected to be bounded by these two parameter choices. This is a reasonable assumption based on the Stephens work.

For each combination of simulation parameters and spectrometer locations, a Target Response Matrix (TRM) is generated, representing the Bremsstrahlung emission from the target for injected electron energies. The Bremsstrahlung spectrum is averaged over 5° polar angular bins and 20° azimuthal bins for the off-axis directionality. The Kα emission detected by the Single Hit Spectrometer is also calculated, generating a Kα Response Matrix (KαRM) for each parameter combination.

Figure 4-6 shows the Bremsstrahlung emission for incident electrons with 200 keV, 1 MeV, 2 MeV, and 3 MeV energies to help visualize the TRM. Since the Bremsstrahlung spectrometer has differential sensitivity only up to 500 keV (photons above 500 keV deposit a uniform signal across the channels, as discussed in Chapter 3), it is useful to see what this means in terms of electron

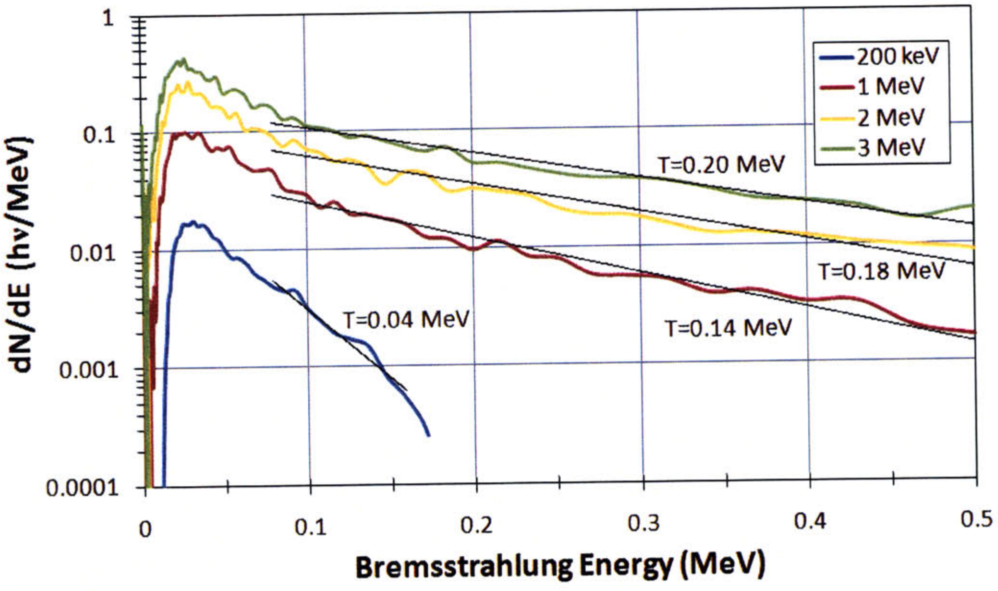

Figure 4-6: The Bremsstrahlung emission for incident electrons with 200 keV, 1 MeV, 2 MeV, and 3 MeV energies. An exponential fit to the photon spectrum from 80 keV to 500 keV shows that the Bremsstrahlung spectrometer can differentiate electrons up to 2-3 MeV.

differentiability. An exponential was fit to the different spectra between 80 keV and 500 keV. A photon slope was determined for each of the incident electron energies. These slopes start to coalesce for electron energies above 2 MeV. The maximum electron differential sensitivity is about 2-3 MeV. This makes this instrument suitable for looking at electron distributions in the 1-3 MeV range.

The SRM and TRM are multiplied together for the overall response matrix, representing the response of the dosimeter layers to electrons injected into the target. The deconvolution of the underconstrained electron spectrum constitutes a classic few channel spectrometer problem commonly found in unfolding neutron spectra from Bonner Spheres [97]. This is shown pictorially in Figure 4-7.

The electron spectrum can be unfolded using a number of techniques, such as fitting test distributions, maximum entropy methods, or singular value decomposition. In this work, one and two temperature distributions are used to parameterize the spectrum. These results will be discussed in the following sections.

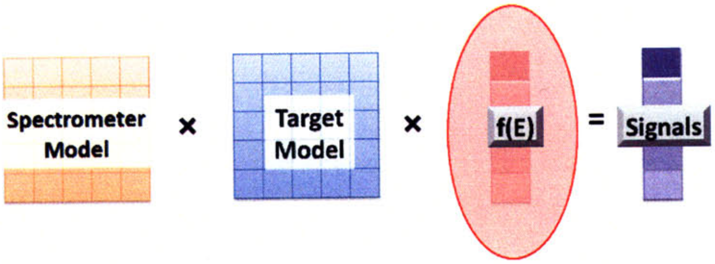

Figure 4-7: The Spectrometer Response Matrix is multiplied with the Target Response Matrix to represent the response of the dosimeters to injected electron distributions.

4.4 1-T Distributions

A single temperature electron distribution with an exponential or 1-D relativistic maxwellian functional form can be fit to the spectrometer data through the response models. The inferred electron temperature for each spectrometer location depends on the assumed electron beam directionality. If the injected electron beam is directed away from the spectrometer location, the spectrometer sees a softer spectrum from the thick-target Bremsstrahlung angular distribution. For a given set of measured data, the inferred electron temperature will be higher as the angle between the injected beam and the spectrometer location increases. Using two spectrometers provides information on the beam directionality. The directionality is estimated by simultaneously fitting the data from both spectrometers. As the beam directionality is varied from the target normal to along the laser axis, the slope temperature calculated for the spectrometer on the laser axis drops and that of the target normal spectrometer temperature rises. The angle at which the predicted temperatures are equal is taken as the beam direction. The coincident temperature is taken as the temperature of the electron distribution. The directionality determination is more important for higher intensities since the electron cone angle is more directional. For low intensities, electrons less than several hundred keV have a cone angle of almost 2π and the beam directionality does not matter. For these large cone angles the temperature inferred from the data does not depend on the directionality in the simulations used in this analysis. The calculated beam directionality varied from 6 to 16 degrees, consistent with the target normal to laser axis range previously discussed.

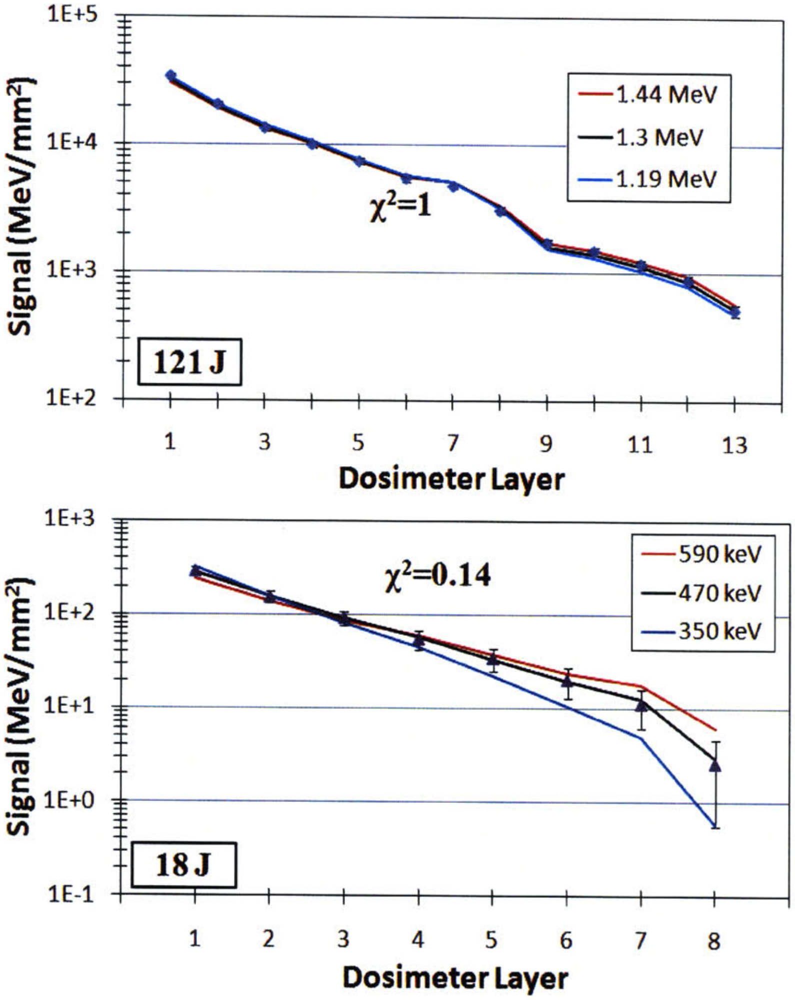

Figure 4-8: Single temperature exponential fits to target normal spectrometer data for a 121 J and a 18 J shot. The black lines represent the best fit temperature. The red and blue lines represent the fit for the maximum and minimum temperatures as determined by a χ^2 fitting parameter of the greater of 1 or 2× the minimum χ^2.

Figure 4-8 shows the fit of a single temperature exponential electron distribution to the dosimeter signals of the target normal Bremsstrahlung spectrometer for a 121 J and a 18 J shot. The black line in each graph represents the best fit exponential spectrum. The fitting parameter is characterized by the weighted, reduced χ^2 value, where a $\chi^2 \leq 1$ represents a curve that on average fits the data points within their error bars. For the 121 J shot, the best fit temperature is 1.3±0.15 MeV, with $\chi^2 = 1$. The 18 J shot has a best fit temperature of 470±120 keV, with $\chi^2 = 0.14$. The dosimeter error bars on the latter channels are larger for the 18 J shot due to lower signal statistics and result in relatively higher temperature errors. The error bar on the temperature is determined by the maximum and minimum temperatures for which χ^2 is the greater of 1 or $2\times$ the minimum χ^2. The red and blue lines on each plot represent the fit for the maximum and minimum temperatures. The error bars are typically on the order of 100-200 keV.

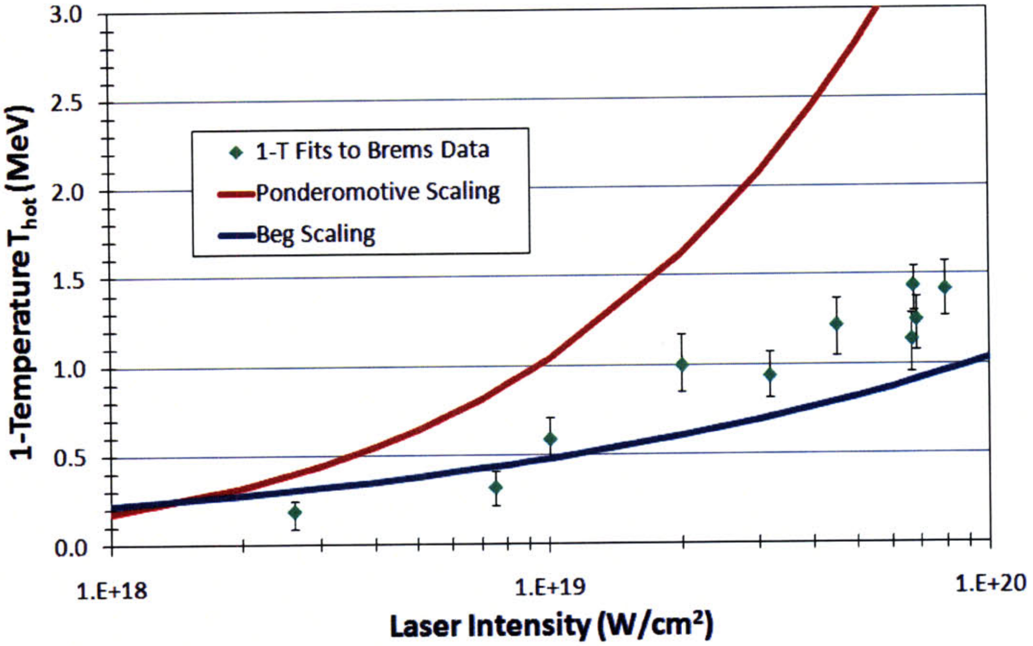

Figure 4-9: The temperatures from the Bremsstrahlung measurements are plotted against the ponderomotive and Beg scaling laws. The data is significantly colder than ponderomotive scaling with the peak laser intensity. The measured temperatures are also higher than Beg scaling for intensities greater than 2×10^{19} W/cm^2.

A single temperature distribution provides a very good fit to the measured data, with the $\chi^2 \leq 1$ for nearly all of the shots. These single temperature distributions are how the field has typically described these interactions until now [1], [36], [22]. The inferred electron slope temperatures (equivalently, the mean energy for an exponential) are compared to the ponderomotive and Beg scaling laws in Figure 4-9. Typically, the intensity used in the scaling laws is calculated from the power in the

FWHM laser spot, taken here as 15% of the laser energy in a 7 μm diameter spot in 0.7 ps, as derived from measurements described in Chapter 3. This FWHM peak intensity is the primary definition found in the literature, although other definitions such as the peak intensity tip of the intensity profile or an intensity containing 50% of the energy are also used, complicating comparisons to standard scaling laws.

The shot to shot variations of the Bremsstrahlung spectrum described in Figure 4-4 is seen in the cluster of three shots around 7×10^{19} W/cm^2. For these three shots, the maximum difference in T$_{hot}$ is 300 keV, just outside the 100-200 keV error bars, making this variation a relatively small effect. This variation is likely due to a degradation in the laser focal spot over the course of a day from thermal effects in the amplifier chain, which results in somewhat lower peak intensities and slightly colder electron temperatures.

From Figure 4-9 it is clear that the Bremsstrahlung measurements are not consistent with a ponderomotive scaling law using the peak vacuum intensity. At intensities of 5×10^{19}-10^{20} W/cm^2, the measurements are a factor of 2-3 lower than the ponderomotive potentials (with intensities defined the same way). The measured temperatures are, however, closer to Beg scaling, but still higher for intensities greater than 2×10^{19} W/cm^2. The Beg scaling was empirically determined [2] for intensities up to 10^{19} W/cm^2 using p-polarized light at 30° to normal laser incidence angle. The data here diverges slightly from Beg scaling at intensities above the original empirical measurements. This data is also significantly colder than the ponderomotive potential of the laser. However, scaling the electron temperature with a single peak intensity is not the right application of ponderomotive theory because of the widely varying intensity profile in space and time over a real laser focal spot. Despite this, single temperature comparisons to ponderomotive scaling are still typically found in the literature. This issue will be further discussed later in this chapter.

4.5 2-T Spectrum Unfolding

While the 1-T distributions provide a very good fit to the Bremsstrahlung measurements, other electron distributions are also consistent with the data. Since the laser intensity varies in space and time, there is inherently a range of intensities present, which can result in more complex electron spectra. For example, this can be seen in Figure 4-11, where for a synthetic ponderomotive spectrum the slope temperature is higher if measured at higher energies. This spectrum will be discussed further in the following section. The spectral space can be expanded by unfolding the electrons with 2-T distributions, of the type seen in previous experimental and computational work [36], [2], [78]. These distributions are parameterized by hot and cold temperatures and the ratio between the two components, and can be represented by a function of the form

$$f(E) \propto R\varphi(E \mid T_c) + \varphi(E \mid T_h), \tag{4.2}$$

where T_c and T_h are varied from 10 keV to 10 MeV, the ratio R ranges from 0.1 to 1000, and φ is a normalized Boltzmann or 1-D relativistic Maxwellian distribution. The electron spectrum is again unfolded by calculating the χ^2 fitting parameter for each distribution parameterized by the two temperatures. The matrix response model simplifies testing of the entire parameter space. The fitting parameter is calculated for 16 million distributions per shot, providing highly resolved variances of the distribution. The electron distributions that simultaneously fit both of the spectrometers within one χ^2 are selected as valid fits.

Figure 4-10a shows a sample subset of allowed distributions for the 121 J shot discussed in the previous section. These sample spectra are represented by the color lines. A broad range of electron distributions are consistent with the data, with almost an order of magnitude difference in the number of electrons at any given energy. The straight dotted black line in 4-10a represents the single temperature distribution with a 1.3 MeV slope temperature. The other sample distributions demonstrate that this single temperature is not unique and depends on the energy

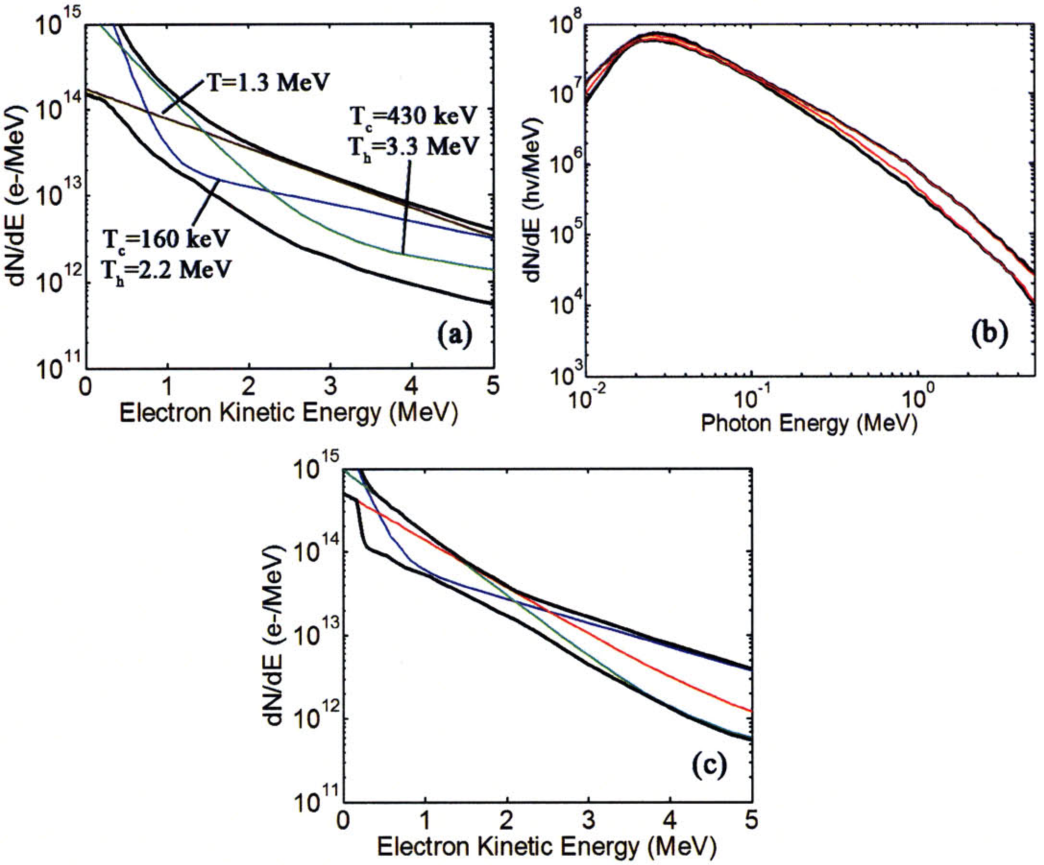

Figure 4-10: (a) Various 2-T electron spectra are consistent with the spectrometer data. The colored lines represent a selected subset of different electron distributions that fit the spectrometer data within one χ^2. The black lines represent the envelope bounding the electron distributions. This envelope bounds the space of the electron distributions but not every distribution within the envelope is a solution within the error bars of the data. (b) The black lines represent the envelope of Bremsstrahlung spectra consistent with the various electron spectra in 4-10a. The Bremsstrahlung is spectrum is degenerate, with the different electron spectra in 4-10a producing the same Bremsstrahlung emission. The red lines represent the Bremsstrahlung envelope consistent with the Bremsstrahlung spectrometer data and Kα emission data. As expected, the Kα emission does not influence the photon spectrum, which is independently measured. (c) 2-T electron spectra consistent with both the Bremsstrahlung data and the K-shell emission. The colored lines again represent a sample subset of electron distributions, this time consistent with both the Bremsstrahlung data and the Kα emission data. The K-shell emission acts as an electron counter that further constrains the electron spectrum. The black lines represent the envelope bounding these electron distributions.

range in which the slope is measured. The envelope surrounding all of the 2-T distributions consistent with the Bremsstrahlung data is represented by the solid black lines. This envelope represents the boundary of the space within which the solutions are found. However, not every distribution that can be drawn in the envelope will be a solution consistent with the data. For example, other straight lines can be drawn within the space representing 1-T fits with widely varying slope temperatures. As shown in Section 4.4, however, the 1-T solutions consistent with the data have slope temperatures within the 1.3±0.15 MeV.

The wide range of electron distributions consistent with the data is the result of two issues. The first is that the electron spectrum is only constrained up to a couple of MeV due to the 500 keV photon differential sensitivity of the spectrometer. The second is that a number of these electron distributions without higher energy constraints can generate similar photon spectra, as seen in Figure 4-10b. The solid black lines represent the envelope of Bremsstrahlung distributions generated by the different electron spectra. This envelope is significantly narrower; similar Bremsstrahlung spectra can be generated with larger numbers of colder electrons or smaller numbers of hotter electrons. As expected, the Bremsstrahlung envelope starts to broaden above the energies where the spectrometer no longer has good differential sensitivity. The only constraint on the Bremsstrahlung spectrum above those energies is the incorporation of the prior assumption that the electron distribution has a 2-T exponential form. The exponential falloff with slopes up to 10 MeV is a physically reasonable assumption based on the ponderomotive potential and the intensities in this experiment.

The envelope of unfolded electron spectra was reduced by using the independent measurement of the Cu Kα emission from the fluorescence layer. This measurement is used as an additional constraint on the electron number. The Kα emission is measured on each shot, thereby accounting for the 30% shot to shot variation. For this 121 J shot the measured Kα yield was $5.3 \times 10^{11} \pm 20\%$ photons/SR. (Note that this yield does not need an opacity correction since the opacity is already calculated into the KαRM through the Monte Carlo simulation.) The Kα signal effectively acts as a counter of electrons above 50 keV; these have sufficient energy to reach the copper layer and efficiently stimulate fluorescence. With the Kα constraint, the range of possible electron distributions is significantly narrowed, as shown in Figure 4-10c. The photon spectrum is not affected, as seen in the solid red lines Figure 4-10b. This is expected since the photon spectrum is an independent measurement. This is the first time this analysis has been applied to characterizing the electrons produced in short-pulse laser plasma interactions.

4.6 Comparison to Synthetic Spectra from Scaling Laws

Experimental comparisons to ponderomotive scaling typically use a single-temperature electron distribution with a T_{hot} from the peak laser intensity [1], [3], [36]. As shown above, the Bremsstrahlung data is colder than the ponderomotive potential characterized by a single peak intensity. For the 121 J shot, this results in a 3.3 MeV ponderomotive temperature, which is well outside the error bars ($\chi^2 \approx 70$) of the 1.3 ± 0.15 MeV single-temperature fit ($\chi^2 \approx 1$).

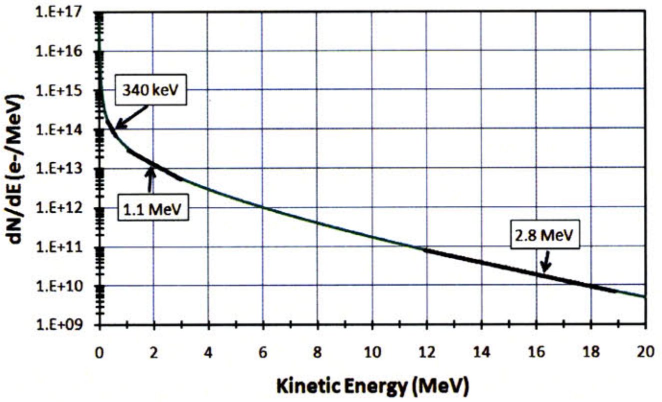

Figure 4-11: The synthetic electron spectrum derive from ponderomotive scaling applied to the focal spot intensity distribution. There is no single temperature, and the slope temperature is higher when measured at higher energies.

The ponderomotive acceleration mechanism is a local effect, and a proper comparison to ponderomotive scaling can only be made by accounting for the actual intensity distribution, instead of just a single number. The intensity distribution from the focal spot image can be used to generate a synthetic electron spectrum. The intensity distribution is binned in time and space using the laser focal spot and a 0.7 ps Gaussian temporal profile as measured from the autocorrelator trace discussed in Chapter 3. The intensity distribution using the focal spot and a 0.7 ps flat top temporal profile is shown in Figure 4-12. A conversion efficiency and electron energy spectrum is then assigned to each intensity element in space and time using an exponential distribution with a slope temperature equal to the ponderomotive potential and a conversion efficiency model. Here a flat coupling model described by Myatt [74] and Nilson [5] is used, with the coupling efficiency scaled to the measured data (alternatively Yasuike's 10-50% coupling efficiency [4] would make the hot tail of the electron distribution slightly hotter and would increase the discrepancy shown here between the measured data and the ponderomotive model for temperature). The synthetic distribution is then generated by integrating these electron distributions in space and time. This synthetic spectrum is shown in Figure 4-11. This spectrum does not have a single temperature, and the slope temperature is higher when measured at higher energies. As expected, the slope temperature at very high energies is consistent with the peak intensity ponderomotive potential since the high energy electrons are prescribed from the peak intensities of the laser profile.

A comparison of the synthetic ponderomotive spectrum to the data for the 121 J shot is given by the red line in Figure 4-13. The spectrum is still slightly hotter than the data with a $\chi^2 = 8$. This spectrum is a much better fit than the 1-T spectrum with the 3.3 MeV peak intensity ponderomotive potential temperature. To characterize how well this synthetic ponderomotive spectrum fits the data, it is useful to compare it to a 1-T distribution with the same $\chi^2 = 8$ fitting parameter. The equivalent 1-T distribution has a 1.7 MeV temperature, somewhat higher than the 1.3 MeV best fit, but significantly less than 3.3 MeV.

Recent simulations by Chrisman, Sentoku, and Kemp [8], and Kemp et al. [24] show a reduction in the slope temperature due to light pressure induced steepening of the

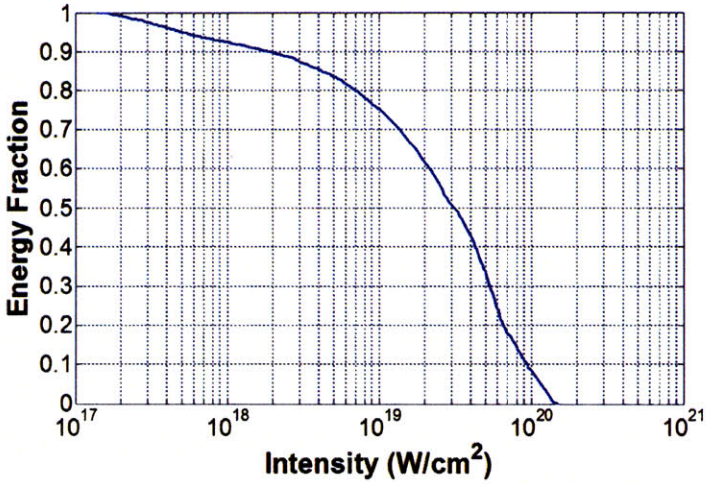

Figure 4-12: The intensity distribution of the laser focal spot assuming 150 J and a 0.7 ps flat top temporal profile. The focal spot was measured with a 16-bit CCD and with 0.45 μm spatial resolution and is the same focal spot shown in Chapter 3.

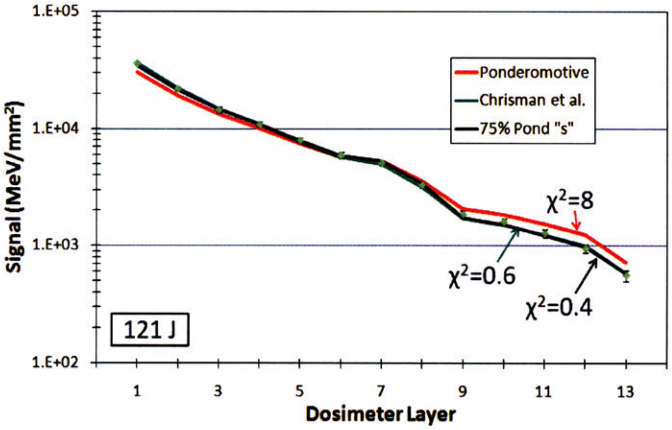

Figure 4-13: The fits from the synthetic ponderomotive distribution, the Chrisman distribution, and the 75% synthetic ponderomotive distribution are plotted against the target normal spectrometer data for the 121 J shot. The synthetic ponderomotive spectrum is slightly hotter with a χ^2=8. The Chrisman and 75% synthetic ponderomotive distributions fit well to the data.

density gradient. This arises from shortening of the jxB acceleration distance by a factor $\sqrt{\frac{\gamma n_c}{n_s}}$, where n_s is the upper shelf density (as described in Chapter 2.1 as n_p, the plasma density). The energy spectrum is parameterized by splitting the hot electrons into two components, one with a slope temperature equal to the ponderomotive potential and the other reduced by the factor $\sqrt{\frac{\gamma n_c}{n_s}}$. Each component contains half of the energy. This analytic parameterization of the electron spectrum was applied to the focal spot intensity distribution in the same way. This spectrum fits the data very well, with a $\chi^2 = 0.6$, and is represented by the green line in Figure 4-13.

Wilks' 1992 PIC simulations [23] show electron temperatures 25% higher than the ponderomotive potential for p-polarization and 25% lower for s-polarization. If the ponderomotive temperature applied to the focal spot intensity distribution is reduced by a scale factor, i.e. $T_h = fT_{POND}$, temperatures where f=70-80% produce a spectrum that fits the data with $\chi^2 \leq 1$. The data thus fall within the "error bar" of ponderomotive scaling if the lower s-polarization temperatures are taken from the PIC simulations. This synthetic spectrum is the best fit to the data with a $\chi^2 = 0.4$, represented by the black line in Figure 4-13. Since the laser in this experiment is s-polarized (with small p components due to the focusing optics and the 3-D plasma profile), this most accurately represents ponderomotive scaling in this experiment.

Figure 4-14 shows these three spectra plotted against the envelope of Kα constrained fits from Figure 4-10c. The ponderomotive and 75% ponderomotive synthetic spectra fall within the envelope of constrained fits. Even though the ponderomotive spectrum falls within the envelope, it does not fit the data within the error bars (it falls within the boundaries of the solution space but is not itself a solution). The 75% ponderomotive spectrum is consistent with the data, as shown in Figure 4-13. At lower energies, the Chrisman spectrum deviates outside the Kα constrained envelope. This spectrum is consistent with the Bremsstrahlung data but the low energy electrons generate too much Kα emission. It is possible that the Kα emission from the fluor is affected by resistive transport effects, where Ohmic fields prevent low energy electrons from reaching the fluor and generating Kα. The

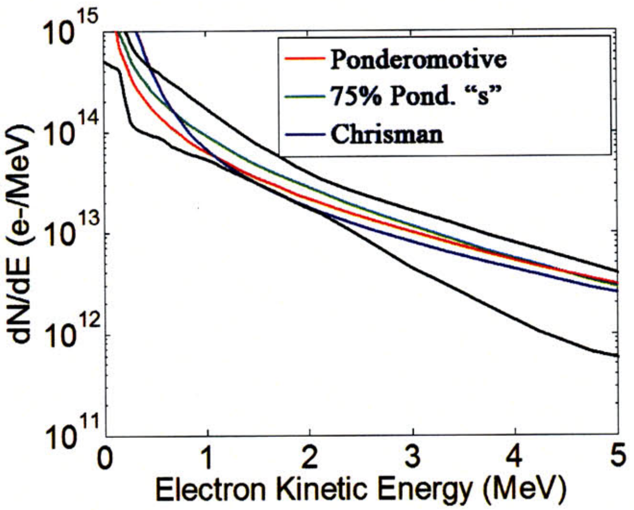

Figure 4-14: The synthetic spectra derived from different T_{hot} scalings using the focal spot intensity distribution are plotted against the electron spectral envelopes from Fig 4-10c. The solid black lines are the envelope constrained by the Bremsstrahlung and Kα. Both the ponderomotive and 75% ponderomotive scaling fit within the Kα constrained envelope. Even though the ponderomotive spectrum falls within the envelope, it does not fit the data within the error bars. The 75% ponderomotive scaling does fit the data. The Chrisman parameterization [8] ranges slightly outside the Kα envelope at the low end. This spectrum is consistent with the Bremsstrahlung data but generates too much Kα from the low energy electrons. Resistive transport effects may reduce the production of Kα by low energy electrons, altering the constraint boundaries at low energy.

impact of resistive fields will be discussed later in this chapter.

The Beg scaling law [2] was discussed above, with the hot electron temperature scaling as $T_{hot} = 215(I_{18}\lambda^2)^{1/3}$ keV. Since Beg scaling is empirically determined from experimental data, it is more appropriate to use a single peak intensity number rather than the composite intensity distribution. It was shown previously that for intensities above 2×10^{19} W/cm^2 the measured data is slightly hotter than Beg scaling. For this 121 J shot, Beg scaling gives a T_{hot} of 0.9 MeV, which is colder than the 1.3 MeV 1-T fit. For a 0.9 MeV distribution exponential distribution, the χ^2=10, which is outside the lower boundary of the error bars.

Accounting for the focal spot intensity distribution is important in obtaining a realistic comparison to the intensity scaling laws. Ponderomotive scaling using the distribution is still slightly hotter than the data, but fits far better than scaling using a single peak intensity number. The Chrisman parameterization of density gradient steepening fits the Bremsstrahlung data quite well, and deviates slightly outside the measured Kα signal. This high Kα signal may be due to the neglect of resistive transport effects which could reduce the number of lower energy electrons reaching the Cu fluor. The fit from the Chrisman parameterization is better than that of the ponderomotive model but has essentially the same energy fraction of 1 to 3 MeV electrons. At higher intensities required for ignition more of the low energy component of the spectrum would fall in the energy range of interest so the useful fraction would increase. In addition, some PIC models have shown that the density profile steepening is more fully developed for higher intensities with an onset threshold close to the conditions of this experiment [37]. It is clear from this analysis that a single temperature distribution is not appropriate for realistic laser pulses.

Scaling the focal spot intensity distribution with 75% of the ponderomotive potential also provides an excellent fit to the data. This lower scaling was also seen in PIC simulations using “s” polarized light, and is considered as an error bar for the ponderomotive theory. The measured data is also consistent with ponderomotive scaling within this error bar. Since both the 75% ponderomotive potential and the Chrisman parameterization are both consistent with the data, it is not possible at this time to distinguish between the two models. This would require measurements to higher Bremsstrahlung energies where the high energy tail can be tested. Resistive transport effects may also shift affect the Bremsstrahlung emission and upshift the ponderomotive spectrum. This issue is addressed in the Discussion section later in this chapter.

4.7 Conversion Efficiency Scalings with Intensity

Since 1-3 MeV electrons have the appropriate range to couple efficiently to the compressed core, the coupling of the laser into electrons of these energies is one of the critical parameters for evaluating the success of fast ignition. This 1-3 MeV conversion efficiency allows the electron spectrum and conversion efficiency to be parameterized in a coupled way. Despite the broad range of 2-T electron distributions, the total conversion efficiency ($\eta_{L \rightarrow e^-}$) and the conversion efficiency into 1-3 MeV ($\eta_{L \rightarrow 1-3MeVe^-}$) electrons are more tightly constrained. For each of the fitted electron distributions, the conversion efficiencies can be determined by integrating the moment of the distribution function across the corresponding energy range. This is depicted in Figure 4-15, which shows the energy weighted distribution function from the synthetic ponderomotive spectrum. The blue shaded area represents the energy in 1-3 MeV electrons and the yellow shaded area (including the blue) represents the total energy in all electrons.

For the 121 J shot, the predicted conversion efficiencies for the different models and parameterizations are given in Table 4.2. The conversion efficiency range predicted from the 2-T parameterization is significantly narrowed with Kα data. The different scaling laws all give conversion efficiencies within or very close to the bands predicted by the 2-T parameterizations. The Chrisman spectrum total conversion efficiency is much higher than the synthetic ponderomotive spectrum conversion efficiency but has a similar number of 1-3 MeV electrons. This higher total conversion efficiency is due to the larger number of prescribed colder electrons which contribute to the total energy but do not produce significant levels of

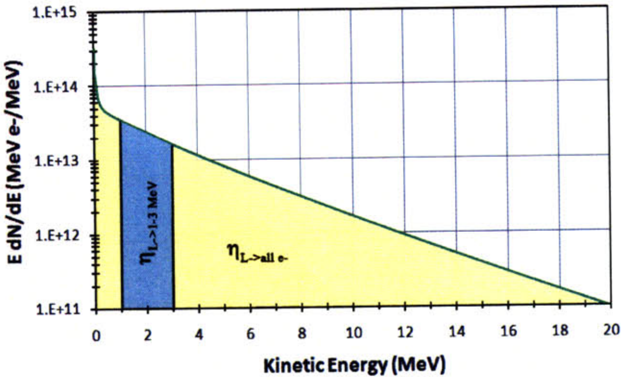

Figure 4-15: The energy weighted distribution function for the synthetic ponderomotive spectrum. The blue shaded area represents the energy in 1-3 MeV electrons and the yellow shaded area (including the blue) represents the total energy in all electrons.

Table 4.2: Inferred conversion efficiencies for the 121 J shot.

Model	$\eta_{L\rightarrow e^-}$	$\eta_{L\rightarrow 1-3MeVe^-}$
2-T parameterization (Brems only)	36-71%	5-23%
2-T parameterization (Brems+Kα)	39-57%	12-22%
Ponderomotive (focal spot distribution)	37%	12%
75% Ponderomotive	46%	16%
Chrisman parameterization	59%	11%

Bremsstrahlung. The 75% ponderomotive spectrum has more energy in 1-3 MeV electrons because of the lower temperature scaling for the hot electrons.

Figure 4-16 shows the scaling of $\eta_{L\rightarrow 1-3MeVe^-}$ with the laser intensity. The solid gray bars represent the predicted conversion efficiencies for the spectra that fit the Bremsstrahlung data within the error bars; the orange bars also fit the Kα constraint within its 20% error bars, as described earlier. $\eta_{L\rightarrow 1-3MeVe^-}$ peaks around 2x10^{19} W/cm^2 and then falls off. The conversion efficiency into 1-3 MeV electrons is banded between 12-28%. For reference, the black line represents the conversion efficiency into 1-3 MeV electrons assuming a Boltzmann distribution with ponderomotive scaling using the peak intensity and a 50% conversion efficiency. With standard ponderomotive scaling using the peak intensity, $\eta_{L\rightarrow 1-3MeVe^-}$ peaks at too low an intensity compared to the data, confirming that the calculated spectrum needs to take into account both the focal spot distribution and a possible reduction in the scaling temperature. The total conversion efficiencies are shown in Figure 4-17. These are banded between 35-60% and are consistent with the 10-50% Yasuike conversion efficiencies but slightly higher than the 10-30% minimum conversion efficiencies measured by Theobald, Myatt, and Nilson.

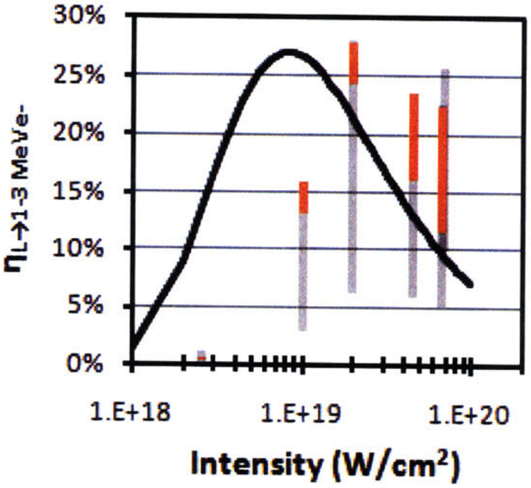

Figure 4-16: The conversion efficiency into 1-3 MeV electrons is plotted vs. laser intensity. The grey bars represent the predicted conversion efficiencies from the Bremsstrahlung data. The orange bars represent the conversion efficiencies also consistent with the Kα fluorescence measurement. Above 10^{19} W/cm^2, about 12-28% of the laser energy goes into 1-3 MeV electrons. For reference, the black line represents conversion efficiency into 1-3 MeV electrons given ponderomotive scaling with the peak intensity and a 50% total conversion efficiency.

4.8 Discussion

The actual number of useful electrons for fast ignition is complicated by the cone angle and transport effects. For example, in an analytic study of integrated fast ignition models, Atzeni [22] assumes a 25% total conversion efficiency and a hot electron temperature consistent with ponderomotive scaling, resulting in electrons with a non-optimal range for coupling to the hot spot. The total conversion efficiency measured here is up to a factor of two higher, with electron temperatures that predict a more optimal range. The cone angle assumed here, however, ranges from 90-60° for 1-3 MeV electrons, resulting in deposition radius significantly worse

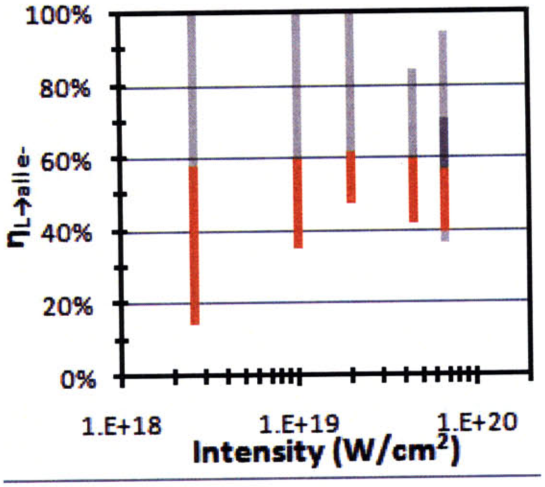

Figure 4-17: Laser conversion efficiencies into all electrons range from 35-60% for intensities above 10^{19} W/cm^2.

than the collimated beams in analytic models. Whether these electron beams undergo magnetic collimation at ignition scale conditions is a subject of ongoing study [26], [28]. If they are collimated, this would significantly improve the coupling efficiency to the core.

4.8.1 Systematic Uncertainties

There are two primary sources of potential uncertainty that may systematically bias this analysis: (1) the assumption of the electron cone angle and (2) the neglect of resistive transport effects. These two issues are discussed in this subsection.

Angle Effects

In contrast to the classical ejection angle assumption, if all the electrons are launched into a 40° cone angle, the calculated conversion efficiencies would be lower. The conversion efficiencies for the two angular distributions are shown in Table 4.3. The full conversion efficiency is 25% lower and the 1-3 MeV conversion efficiency 40% lower in the 40° model. The angular distribution of the electrons is the main uncertainty in unfolding the electron conversion efficiency from the Bremsstrahlung measurements. A full spectral and angular measurement, similar to work by

Table 4.3: Inferred conversion efficiencies for the 121 J shot for different angular distributions

Angular Distribution	$\eta_{L\rightarrow e^-}$	$\eta_{L\rightarrow 1-3MeVe^-}$
Classical Ejection Angle	39-57%	12-22%
40° Fixed Full Angle	31-43%	7-14%

Schwoerer [98], or imaging of multiple fluorescent layers buried in the target would help provide additional constraints on the angular distribution. Proposals for improved angular measurements are discussed in the Future Work section in Chapter 5.

Field Effects

The other source of error is the neglect of collective electric and magnetic effects in the transport model. While collective fields are not present in a basic Monte Carlo model, the impact has been estimated using an analytic [99], [79] model where an Ohmic potential drives a return current of thermal electrons. The magnitude of the potential in these experiments was estimated using an initial electron spectrum from ponderomotive scaling using the intensity distribution and a 37% conversion efficiency, as described above. The electrons are binned into energy groups and are launched from a 30 μm diameter spot into a cone angle given by the classical ejection angle. The electric field is given by

$$E(z) = \eta(z)\, j(z) = \eta(z) \sum_i \frac{N_i e}{\pi\tau} \frac{1}{(r_0 + z\, tan\theta_i)^2} H(R_i - z), \tag{4.3}$$

where η is the resistivity of the material, N_i is the number of electrons in each energy group, r_0 the initial spot size, θ_i the divergence angle of each energy group, H the Heaviside step function, and R_i the range of the electrons in each energy group. The electric field is calculated as a function of depth with a cutoff at the electron range. The electrons lose energy through collisional, radiative, and resistive effects. The collisional and radiative losses are taken from tabulated values for cold matter [42]. Scattering is included by taking the electron path length as two times greater than the linear penetration depth, which has been shown for energies from 10 keV to several MeV [100], [101]. The electron range is thus approximated by integrating the energy loss against the potential into the target along with twice the collisional and radiative losses. The electric field is calculated and summed for all energy groups and integrated for a potential across the target. This procedure is then iterated to converge upon a self-consistent solution of the potential and electron penetration depth.

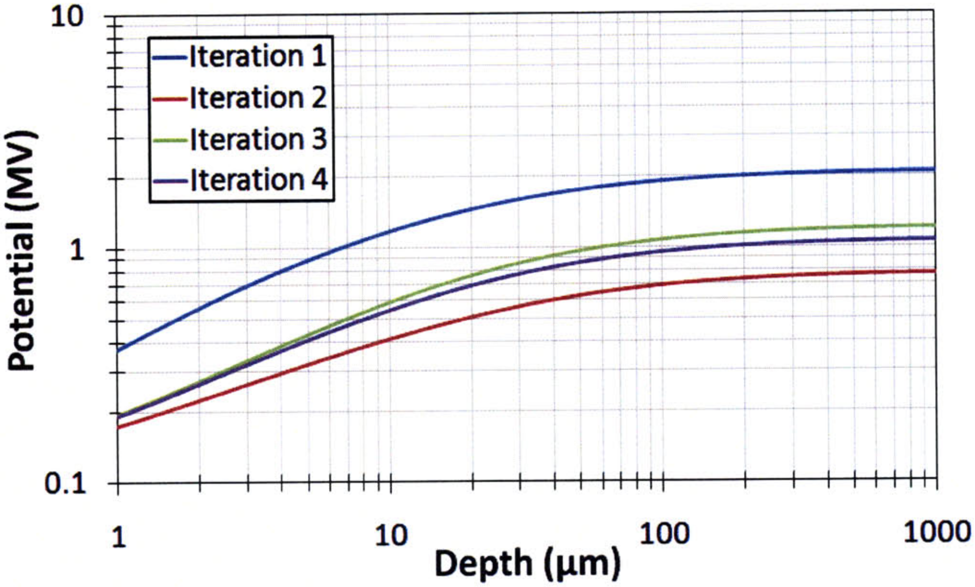

Figure 4-18: Laser conversion efficiencies into all electrons range from 35-60% for intensities above 10^{19} W/cm^2.

This calculation is shown in Figure 4-18. The first iteration has no resistive fields so the electrons have a longer range; the electric field drops only from the angular divergence of the electrons. In the second iteration, the resistive field is overestimated from the long range of the electrons and results in an underestimate of the potential. The calculated potential converges at the 4th iteration. Using this formulation, the potential across the target is calculated at 1.1 MV using a peak aluminum resistivity of about $1.5 \times 10^{-6}\Omega - m$ for the entire bulk, assuming that most of the interaction occurs at temperatures between 10 eV and 100 eV for which the resistivity of Al is close to the peak value. Half of the potential is in the first 10

μm, and 3/4 is in the first 30 μm, before the electrons have had a chance to spread. The calculated potential is temperature dependent because the the resistivity decreases with increasing and decreasing temperature (the peak resistivity is used here). The potential will be lower when the actual temperature distribution in the target is taken into account. 3-D currents may also serve to partially lower the front surface charge buildup and thus reduce the potential felt by the hot electrons. Regardless, given the electron currents in these experiments, the potential is likely to be at least a few hundred kV.

Neglecting this potential in a Monte Carlo analysis will influence the interpretation of the conversion efficiencies. Since the majority of the potential is in the first few tens of microns and the Bremsstrahlung is produced throughout the bulk, all of the electrons producing Bremsstrahlung in the target pass through this potential. The electron spectrum is essentially downshifted by this potential before it produces Bremsstrahlung. Conversely, the electron spectrum inferred from the measured Bremsstrahlung emission is therefore upshifted by the potential. In terms of a simple 1-T treatment, if the mean energy is taken to be 1.3 MeV, a shift of a few hundred kV would only slightly perturb the inferred conversion efficiencies. At the upper bound of a 1 MV potential, this might be a significant effect, but still leaves the mean energy lower than the 3.3 MeV predicted from ponderomotive scaling with a single peak intensity. Transport simulations similar to those by Davies [79] and Honrubia [96] are necessary to quantify the shift in the spectrum. The Kα emission is strongly influenced by the Ohmic potentials, as previously discussed by Davies. With the Monte Carlo analysis, the fluor acts as a counter of electrons above 50 keV. If there is a potential of a few hundred kV in the first ten microns before the fluor, those electrons are ranged out due to resistive losses before their reach the fluor to produce Kα. Only higher energy electrons will reach the Cu layer. The energy at which this counter acts is therefore upshifted to a few hundred keV.

The impact of the Ohmic potentials on the Kα constraint is mixed. The electron spectra in the envelope of Figure 4-10a with larger numbers of electrons in the hundreds of keV range produce too much Kα in the Monte Carlo model to be consistent with measured Kα emission. With an Ohmic model, the low energy electrons would not reach the fluor, resulting in a lower Kα emission. These distributions would then be consistent with the Kα measurements. This would result in an upward revision of the total conversion efficiency since there would be larger numbers of low energy electrons. The conversion efficiency into 1-3 MeV electrons would drop since fewer high energy electrons would be needed to produce the measured Bremsstrahlung emission. In Figure 4-17, $\eta_{L \to e^-}$ consistent with the measured Kα is at the lower range of the band consistent with the Bremsstrahlung. In Figure 4-16, $\eta_{L \to 1-3MeVe^-}$ consistent with the Kα is at the upper range of the band consistent with the Bremsstrahlung. The total conversion efficiency goes up and the conversion efficiency into 1-3 MeV goes down when resistive effects are taken into account.

Magnetic fields would also enhance the energy loss near the front surface of the target and reduce the penetration lengths by increasing the curvature of the electron path [79]. The impact of magnetic fields on the conversion efficiency would thus be analogous to that of the Ohmic potential.

The Ohmic potentials will also have an impact on comparisons to the intensity scaling laws. Since the mean energy of the distribution will be upshifted, Beg scaling will remain colder than the data. Ponderomotive scaling with the peak intensity will likewise remain too hot, since at 7×10^{19} W/cm^2 intensities, it is still 2 MeV hotter than the data. The focal spot ponderomotive spectrum, however, is within range of the potential Ohmic correction. This spectral comparison needs to be examined more carefully with hybrid-transport modeling in order to fully assess these issues. This will be the subject of future work.

4.9 Conclusions

The Bremsstrahlung spectrum and Kα emission of a fluorescent layer have been measured in non-refluxing targets. The laser produced electron spectrum is inferred through Monte Carlo modeling of the target interaction. One and two temperature distributions were used to unfold the electron spectra. 1-T distributions provide a good fit to the Bremsstrahlung measurements. Comparisons to intensity scaling laws showed that scaling the ponderomotive potential with a single peak intensity resulted in temperatures that were significantly higher than the measurements. At intensities above 2×10^{19} W/cm^2, the inferred electron temperatures are also higher than the empirical Beg scaling.

2-T unfolding of the electron distributions showed that the 1-T fits are not unique, and that a broad range of electron spectra can generated the same Bremsstrahlung spectra and were thus consistent with the Bremsstrahlung measurements. Kα emission from the Cu fluor was used as an electron counter to help break this degeneracy.

Realistic comparisons to intensity scaling laws require taking into account the spatial and temporal distribution of the laser intensity. A synthetic electron spectrum was derived by applying ponderomotive scaling to a measured focal spot spatial intensity distribution and to a measured autocorrelator trace temporal distribution. This synthetic ponderomotive spectrum was still slightly hotter than the data. A parameterization of density gradient steepening by Chrisman, Sentoku, and Kemp was used to generate a similar spectrum. This spectrum was consistent with the Bremsstrahlung data, but overestimated the Kα emission, most likely because of the neglect of resistive transport effects in the analysis. A synthetic spectrum generated from 75% of ponderomotive scaling as seen in PIC simulations by Wilks of an s-polarized jxB interaction provided the best fit to the Bremsstrahlung and Kα data.

This range of 2-T spectra was used to calculate the total laser conversion efficiencies and the conversion efficiencies into 1-3 MeV electrons of most interest to fast ignition. Conversion efficiencies into 1-3 MeV electrons of 12-28% have been inferred. This represents a total conversion efficiency of 35-60%.

Systematic uncertainties include the assumption of the angular distribution model and the neglect of resistive transport effects. An assumption of a 40° cone angle, rather than the classical ejection angle used in the analysis, would reduce the total conversion efficiency by 25% and the 1-3 MeV conversion efficiency by 40%. Resistive transport effects were estimated using an analytic model which predicts potentials of up to 1 MV, primarily in the first few tens of microns in the target. This potential was calculated using the peak aluminum resistivity across the target, and is likely lower, but still on the order of several hundred kV. This would result in higher total conversion efficiencies than inferred from Monte Carlo modeling but lower conversion efficiencies into the 1-3 MeV energy band.

Chapter 5

5.1 Summary and Conclusions

Bremsstrahlung emission measurements are useful for inferring the hot electron spectrum and conversion efficiency generated by the laser-plasma interaction in short-pulse laser experiments. In this work the Bremsstrahlung emission was measured using a filter stack spectrometer with differential sensitivity up to 500 keV. The spectrometer was developed and absolutely calibrated using radiological and fluorescence sources for energies from 15 keV to 662 keV. Bremsstrahlung measurements were performed on the TITAN laser for laser intensities from 3×10^{18} up to 8×10^{19} W/cm^2. The emission was analyzed using cold matter Monte Carlo simulations with the coupled electron-photon transport code `Integrated Tiger Series 3.0`. The electron spectrum was unfolded from the Bremsstrahlung distribution by using one and two temperature test functions.

Comparisons of the Bremsstrahlung data to intensity scaling laws showed that scaling the ponderomotive potential with a single peak intensity resulted in temperatures that were significantly higher than the measurements. A more realistic comparison to the scaling models was performed using the spatial and temporal intensity distribution from a measured focal spot and an autocorrelator trace. A synthetic electron spectrum generated by applying ponderomotive scaling to the intensity distribution was slightly hotter than the data, but within the range of a potential correction due to the neglect of collective effects. A synthetic spectrum generated from a parameterization of density gradient steepening by

Chrisman was found to be consistent with the Bremsstrahlung data. The Chrisman parameterization, however, predicts too much Kα emission. This discrepancy may be due to the neglect of Ohmic effects which range out the low energy electrons before they reach the Cu fluor. In these intensity regimes, however, it serves only to add a cold electron component that is not of use to fast ignition. A synthetic spectrum scaling with 75% of the ponderomotive potential provided the best fit to the Bremsstrahlung and Kα data. This reduction in the temperature spectrum was consistent with particle-in-cell simulations by Wilks of the jxB acceleration mechanism in an s-polarized light wave, which did not invoke the steepening of the density gradient. The mechanism for the colder electron spectrum is thus inconclusive, but the colder spectrum does provide for better coupling of the electrons to the hot spot in the fast ignition concept.

The unfolding of the electron spectrum from 2-T distributions showed that there is a degeneracy in the Bremsstrahlung measurements, whereby dramatically different electron spectra can produce the same Bremsstrahlung emission. The electron spectrum was further constrained by measuring the K-shell emission from a buried Cu fluor layer in the target. This was done in a non-refluxing target, such that incident electrons only make one pass through the fluor. This allows the fluor to effectively act as an electron counter, breaking the degeneracy in the Bremsstrahlung measurements. With these two constraints, the total inferred laser to hot electron conversion efficiency ranged from 35-60%, with 12-28% of the laser energy going into 1-3 MeV electrons of most use to fast ignition.

The two primary uncertainties in the analysis were the assumption of the electron cone angle in the Monte Carlo modeling and the neglect of resistive transport effects. The electron cone angle was not measured on these experiments. In the Monte Carlo modeling, the cone angle was assumed to vary with the electron energy, consistent with the classical ejection angle of an electron in a laser field, which can be analytically derived from constants of the motion in Maxwell's equations. Prior experimental work by Stephens et al. imaged Kα emission from Cu fluors buried within varying depths of Al. They found a constant 100 μm diameter spot size in the first 100 μm, followed by a constant 40° divergence (full) cone angle. Monte Carlo simulations found that the classical ejection angle assumption was consistent with the measured Kα spot sizes. For reference, in our experiments a 40° cone angle was also used in the Monte Carlo modeling, which resulted in 40% drops in the total conversion efficiency and 25% drops in the conversion efficiency into 1-3 MeV electrons.

Resistive transport effects also influence the unfolding of the electron spectrum from the Bremsstrahlung and Kα data. An analytic model [99], [79] was used to estimate the impact of resistive effects. The model takes into account the collisional and resisitive losses of the electrons and self-consistently solves for the potential across the target. Using the peak aluminum resistivity, the potential across the target is calculated at 1 MV, primarily within the first few tens of microns. The actual potential is likely to be lower, on the order of a few hundred kV due to resistivity differences from temperature gradients and 3-D current effects. This potential upshifts the electron spectrum inferred from the Bremsstrahlung emission and ranges out low energy electrons before the reach the Cu fluor, causing the Kα emission to act as a counter of higher energy electrons. This effect increases the total inferred conversion efficiency but decreases the conversion efficiency into 1-3 MeV electrons

5.2 Future Experiments and Modeling

A number of advancements in modeling and experiments will further constrain the electron spectrum and conversion efficiency. Better quantitative modeling of the experimental data using hybrid particle-in-cell codes like LSP [102], [103] are computationally expensive, but are able to quantify the collective field effects on the inferred electron distributions. Simpler hybrid transport codes such as Zuma [104] are faster and contain the majority of the Ohmic potentials and magnetic field physics. These codes can be used to improve the accuracy of the inferred distributions.

Shot to shot measurements of the angular distribution of Bremsstrahlung can reduce the errors associated with the uncertainty in the cone angle. This can be done by using an array of Bremsstrahlung spectrometers, such as the 10 spectrometers fielded by Schwoerer in lower intensity experiments. Imaging of a fluor buried at deeper depths would also help constrain the angular distribution of electrons. The current set of imaging diagnostics is only able to image Ti and Cu Kα lines, representing 4.5 and 8 keV x-rays. Opacity effects in Al preclude imaging of Cu fluors beyond a couple hundred microns, and less for Ti fluors. A crystal imager for 15.7 keV Zr Kα line emission is currently being developed but has yet to be successfully tested. A working Zr imager would allow for target designs with deeply buried Zr fluor layers, providing information on the divergence angle. The Zr fluor would also allow electrons to be counted deeper in the target, correlating with higher energy electrons. In recent TITAN experiments a Ag fluor has been buried at depths up to 500 μm in Al, in addition to the front Cu fluor. Absolute measurements of the 22 keV Kα emission, without imaging, can also be used as an electron counter. The analysis of the data is still ongoing and will be closely coupled to improvements in the modeling capability.

Measurements to higher Bremsstrahlung energies would also be extremely useful in further constraining the electron source. The Bremsstrahlung spectrometer has recently been extended with additional thick Pb filters and now has differential sensitivity up to 800 keV. This spectrometer has already been used in the TITAN buried Cu/Ag experiments and has also been fielded on OMEGA EP as a Bremsstrahlung spectrometer for measuring x-ray emission in diffraction experiments to test material strength and lattice dynamics. Measurements of even higher photon energies can be done using nuclear activation techniques, which have sensitivity above 8 MeV. These are usually done using solid Au, Cu, or Ni activation targets. Signal to noise issues necessitate the activation material be part of the target, which may hinder the ability to use buried fluor techniques.

5.3 Proposed X-ray Measurements between 1-5 MeV

Measurements of the Bremsstrahlung spectrum in the 1-5 MeV range will better constrain the electron spectrum, providing more accurate comparisons to scaling models and tighter estimates on the number of 1-3 MeV electrons. Figure 5-1 plots the ratio of 2 MeV photons to 1 MeV photons against the conversion efficiency into 1-3 MeV electrons for the electron spectra consistent with the Bremsstrahlung data in the previous chapter. Measurements of even a single ratio in the 1-3 MeV regime will significantly reduce the uncertainty in the electron spectrum. However, while filter stack spectrometers can measure photons up to an MeV and nuclear activation can measure photons greater than 8 MeV, it is extremely difficult to measure the photon spectrum between these two energies. One possible technique is to make use of the Compton effect, where high energy x-rays inelastically scatter free electrons in a target. If the Bremsstrahlung interacts with a low Z scattering target, the electron emission spectrum can be correlated with the incident photon spectrum. The unpolarized Compton differential cross section for scattered photons is given by

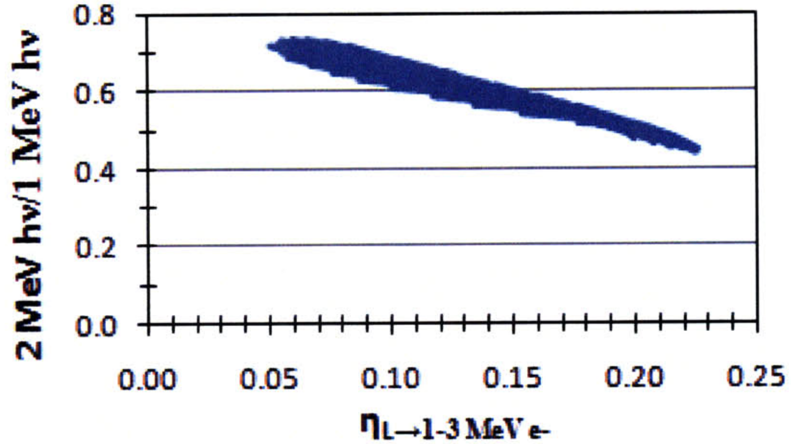

Figure 5-1: The ratio of 2 MeV photons to 1 MeV photons is plotted against the conversion efficiency into 1-3 MeV electrons for the electron spectra consistent with the Bremsstrahlung spectrometer data in the previous chapter.

the Klein-Nishina cross section [68]

$$\frac{d\sigma}{d\Omega} = \frac{r_0^2}{2}\left(\frac{\nu'}{\nu_0}\right)^3\left(\frac{\nu_0}{\nu'} + \frac{\nu'}{\nu_0} - sin^2\theta\right), \tag{5.1}$$

where ν_0 is the initial photon energy, ν' is the final photon energy, and θ is the angle between between the incident and final photon momentum vectors. By energy and momentum conservation θ is given by

$$\frac{1}{h\nu'} - \frac{1}{h\nu_0} = \frac{1}{mc^2}\left(1 - cos\theta\right). \tag{5.2}$$

From conservation laws the differential cross section for the electron can be written as

$$\frac{d\sigma}{dT} = \frac{d\sigma}{d\Omega}\frac{2\pi}{\alpha^2 mc^2}\left[\frac{(1+\alpha)^2 - \alpha^2 cos^2\phi}{(1+\alpha)^2 - \alpha\,(2+\alpha)\,cos^2\phi}\right]^2, \tag{5.3}$$

where $\alpha = h\nu_0/mc^2$ and cot $\phi = (1+\alpha)\,tan\frac{\theta}{2}$. Since Compton scattering is a 2-body problem, the scattering angle can be uniquely correlated with the energy of the electron. The electron spectrum in a narrow forward viewing angle can then be correlated with the incident photon spectrum, provided the scattering of the Compton electron in the target is small. The primary parameters are the viewing angle and the thickness of the scattering target. For thick targets and large viewing angles the signal level is larger, but the energy resolution is reduced due to electron scattering and broader electron energy distributions. The tradeoff is therefore between the signal level and the energy resolution of the spectrometer.

A conceptual simulation has been performed to study the feasibility of the instrument. A beam of photons incident on a small, cylindrical graphite scattering target 7.5 mm thick and 3 mm in radius is modeled with `ITS 3.0`. The output electron spectrum in a narrow 5° cone angle is tabulated for different input photon energies to generate a response matrix for the Compton target. The output electron spectrum is coupled to an electron spectrometer currently in use [105], with known energy resolution and sensitivity threshold characteristics. The input photon spectrum is taken from measured photon distributions described in this current work. The absolute intensity of the photon spectrum is set by placing the graphite scattering target at rear surface normal 30 cm from the laser target to provide sufficient space to magnetically deflect escaping laser electrons. The graphite target is placed close to the front aperture of the electron spectrometer such that a 20° full cone angle of electrons enters the spectrometer. This larger acceptance angle degrades the energy resolution but increases the signal to noise level, reflecting the primary tradeoff in the Compton spectrometer design.

Simulated Compton electron data is shown in Figure 5-2. Four curves are plotted, representing the Compton electron spectrum detected in the spectrometer from the Bremsstrahlung emission produced by different input laser electron spectra into the Al/Cu/Al target. The blue line labeled POND100 represents the synthetic spectrum from ponderomotive scaling using the intensity distribution, the red line labeled POND75 represents the synthetic spectrum using 75% of ponderomotive scaling with the intensity distribution. These are the distributions described in Chapter 4. The other two colored lines, labeled "15% and 23% 1-3 MeV e-" represent best fit two temperature spectra with the corresponding 1-3 MeV conversion efficiencies. These lines are detectable above the 1e4 electrons/MeV noise floor of the instrument for Compton electron energies up to 3-5 MeV. The noise floor ranges between 1e3 and 1e4 electrons/MeV and is due to the background levels on the electron spectrometer on a full intensity Titan shot. This noise floor can be reduced with better instrument shielding. The 1e2 electrons/MeV detection threshold is the minimum detection threshold of the spectrometer in a low noise environment, such as on a low intensity shot. The solid black line represents the energy resolution of the electron spectrometer for a 20° full cone angle of electrons entering the spectrometer. The resolution up to 5 MeV Compton electron energy is better than 1 MeV.

The energy resolution shown here is not yet convolved with the energy resolution from the Compton scattering process. Additionally, the simulation currently takes the electron spectrum from a 10° full angle output and scales with solid angle for the larger entrance angles. This would also somewhat degrade the energy resolution

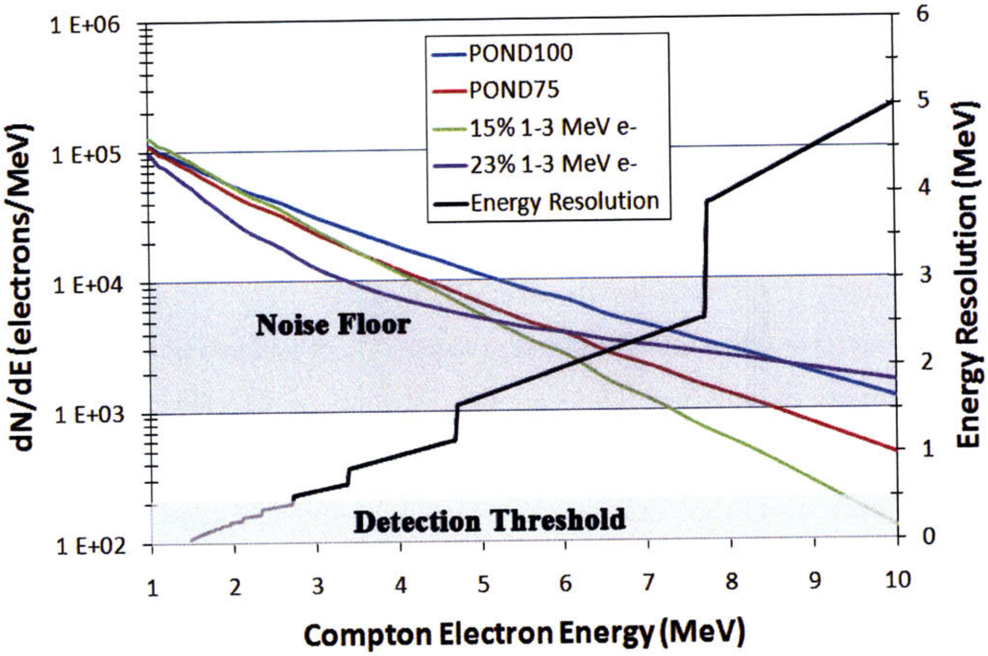

Figure 5-2: The colored lines represent the Compton electron distributions detected by the spectrometer for the Bremsstrahlung emission from different laser electron distributions. The graphite scattering target is 30 cm from the laser target and a 20° full cone angle of electrons enters the electron spectrometer. The black line represents the energy resolution from the electron spectrometer. The noise floor is due to the high noise environment on a full energy Titan shot, and can be reduced with better shielding.

beyond what is shown here. A full design for this diagnostic would require a detailed simulation of the entire system, coupling the scattering target to the magnetic field map of the electron spectrometer. These designs are work for the future.

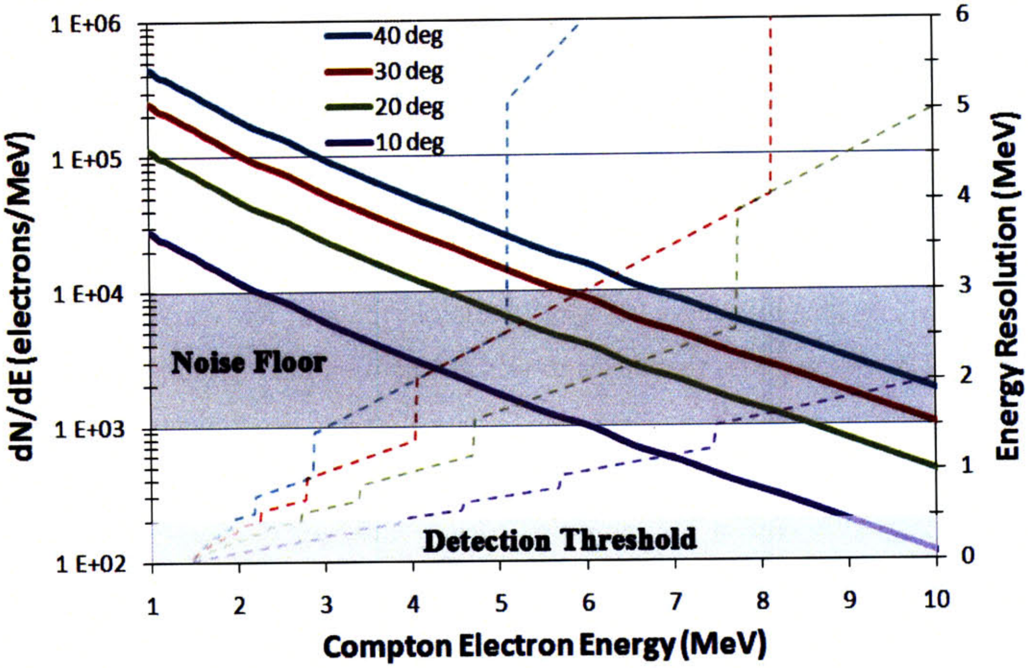

Figure 5-3: The tradeoff in energy resolution versus signal level is shown in this Figure. As the distance between the scattering target and the electron spectrometer is reduced, the signal level increases but the cone angle of electrons entering the spectrometer also increases, degrading the energy resolution of the spectrometer. The dashed color lines represent the electron spectrometer energy resolutions corresponding with the solid color lines for the simulated spectra.

The tradeoff in energy resolution versus signal to noise is shown in Figure 5-3, where the spectrum for the 75% ponderomotive scaling is plotted for various acceptance angles into the spectrometer. Again, the energy resolution shown here involves only the degradation in resolution due to the larger acceptance angle for the magnetic spectrometer, and does not yet couple in the degradation from the Compton scattering process. The dashed lines of the same color represent the corresponding energy resolutions. For smaller acceptance angles, the signal level drops but the energy resolution increases. A 20° full angle gives reasonable parameters for an instrument design on Titan. This design space for the spectrometer is improved for the OMEGA EP and NIF ARC lasers, as their higher energies provide better Bremsstrahlung signal levels for the spectrometer. These higher energy Bremsstrahlung measurements would help confirm the intensity scaling laws and provide shot to shot information on the full laser electron spectrum.

5.4 Concluding Remarks

The recent completion of both the OMEGA EP laser and the National Ignition Facility makes this an exciting time for ICF and fast ignition research. It is hopeful that ICF will be able to achieve hot spot ignition in the next few years. The OMEGA EP laser provides the means to test fast ignition interaction physics at far higher energies than have been achievable to date. In these experiments, conversion efficiencies of 12-28% into 1-3 MeV electrons were measured, representing 35-60% total coupling. This provides an optimistic view for fast ignition. Analytic ignition models typically use a total coupling efficiency of 25%, with a single intensity ponderomotive spectrum for the electrons. For 10^{20} W/cm^2 intensities, this represents about 7.5% in the 1-3 MeV band. Thus, the 12-28% coupling is almost a factor of two higher, but was measured at a somewhat lower intensity. Additionally, with modeling that accounts for resistive transport effects, the inferred spectrum may be closer to ponderomotive and the amount of energy in 1-3 MeV electrons will be lower. Significant work remains to be done on reducing the error bars on the conversion efficiency and electron spectrum. The impact of the preformed plasma profile on the electron spectrum in a confined cone geometry is also an important subject of ongoing research. Additionally, the transport physics under fast ignition relevant plasma conditions is only starting to be experimentally tested. Fast ignition integrated experiments combining both the implosion driver and the igniter driver have recently started on OMEGA EP at near-ignition experimental conditions. If successful, fast ignition could provide a significantly broader path towards inertial fusion energy.

Appendix A

An Estimation of the Composition of FujiFilm Image Plates

An Estimation of the Composition of FujiFilm Image Plates

C.D. Chen
Plasma Science Fusion Center, MIT, Cambridge, MA 02139
P.K. Patel
Lawrence Livermore National Laboratory, Livermore, CA 94550

Introduction

Image plates (IP) are frequently used as x-ray and charged particle detectors in a variety of diagnostics due to their resolution, resistance to EMP, dynamic range, and reusability. While their response curves have been measured, it is useful to have an idea of the composition of the image plates in order to model their response and transmission curves in codes. There has been some confusion over the composition details provided by FujiFilm and this note serves to provide a best estimate for the BAS-SR, BAS-TR, and BAS-MS image plates.

Composition Information

Total Thickness

Details regarding image plate composition were obtained from two sources, a Fuji Medical Systems sales representative and through the Fuji Life Sciences website. The sales representative provided a document that described the thicknesses and densities of the various layers of the image plates, along with the barium weight % and the density of the phosphor for the different IPs. This document is attached at the end of this note. The FAQ section of the Fuji Life sciences website contains some information on the composition of the BAS-MS image plate (shown in Table 1). Between the two documents, there seem to be inconsistencies with regard to the total thickness of the image plate and the thicknesses of the back layers. Additionally, even within the attachment, there is an inconsistency in the thickness of the BAS-MS image

Table 1

MS-IP			
Layer	Thickness (μm)	Density (g/cm^3)	Material
Back protective layer	25	1.4	polyethyleneterephthalate (PET)
Ferrite layer	80	3.0	MnO, ZnO, Fe203 + plastic
Base layer	190	1.4	polyethyleneterephthalate (PET)
Back layer	12	1.4	plastic
Phosphor layer	115	3.3	phosphor*:urethane = 25:1 *$BaFBr_{0.85}I_{0.15}$ density 5.2 g/cm^3
Surface layer	9	1.4	polyethyleneterephthalate (PET)

plate. When one sums the thicknesses of the layers, it sums to 458 μm instead of the 486 μm quoted as the total thickness. To resolve this discrepancy, we measured the thickness of two of our BAS-MS image plates, and the weight of one of them. The thickness of the image plate came out to 476-480 μm in one case and 465-469 μm in the other. The weight of the 465-469 μm IP was 1049 g/m^2. The manufacture error is thus probably around 2-3% in the layer thicknesses.

Phosphor Layer

Between the attachment and the website, we know the following about BAS-MS:

- $\rho_{phosphor}$ = 5.2 g/cm^3, composed of $BaFBr_{0.85}I_{0.15}$
- $\rho_{phosphor\ layer}$≈3.307 g/cm^3 (phosphor mixed with urethane in 25:1 ratio)
- $\rho_{phosphor}$ in that layer = 3.18 g/cm^3
- % Barium weight = 19%

The urethane can be assumed to be some polyurethane resin with density ~1.2 and a Z_{eff} of ~6.6[i]. The polyurethane binder is a small percentage of the phosphor layer composition. The phosphor density within the phosphor layer is 3.18 g/cm^3, with the polyurethane binder making up the rest of the 3.307 g/cm^3. This provides for the 25:1 mass ratio and a calculated volume fill factor of ~72%. This is also consistent with the % barium weight, which we note is the % weight of the entire image plate. Along the same lines, the phosphor:urethane ratio of the BAS-SR and BAS-TR is calculated to be 20:1.

Ferrite and Other Layers

The thicknesses of the protective coat and undercoat are consistent between the attachment and the website. These thicknesses are assumed to be correct and composed of 1.37 g/cm^3 PET (Mylar). The rest of the image plate, the Base and Back layers, are assumed to be divided between additional PET and the 3.0 g/cm^3 ferrite layer. The ferrite layer is composed of MnO, ZnO, and Fe_2O_3 with a binding plastic (density assumed ~1.2 g/cm^3). The densities[ii] of the three oxides are 5.37 g/cm^3, 5.6 g/cm^3, and 5.25 g/cm^3, respectively. While the relative mixture ratios are unknown, the elements are all close in Z, and assuming a 1:1:1 mass ratio should not introduce much error. The average density of the ferrite compounds is thus 5.41 g/cm^3. Since there is no stated mass ratio for the ferrite layer, there are two possible assumptions that one can make. The first is that there is a 100% volume fill factor, which leads to a ferrite composition of 77% by mass (if we assume a 1.2 g/cm^3 polyurethane binder). The second assumption is that the layer is primarily ferrite with just enough resin to hold the layer together, and that this resin can be neglected. This assumption requires a 55% volume fill factor. Either way, using the measured values for thickness (470 μm) and weight (1049 g/m^2), the thicknesses of the PET and ferrite layers on the back are calculated to be 222.3 μm and 111.7 μm, respectively.

Summary

The image plate is primary composed of the phosphor and resin layer, coast and support made of PET, and a ferrite/resin layer for the magnetic backing. The phosphor:urethane mixture is different for the BAS-MS (25:1) vs the BAS-SR and BAS-TR (20:1). The phosphor layer thicknesses and weights in the attachment are most likely accurate, given that this is the sensitive region of the image plate. If the ferrite layer is assumed to be consistent across the different image plates, the ratio of the ferrite layer thickness to PET film/support thickness can be easily calculated by measuring the total thickness and weight of the image plate. For BAS-MS, this works out to:

MS-IP			
Layer	Thickness (µm)	Density (g/cm^3)	Material
Ferrite layer	112	3.0	MnO, ZnO, Fe203 (1:1:1)+plastic, ferrite 77% by mass
Base layer	222	1.37	polyethyleneterephthalate (PET)
Back layer	12	1.37	polyethyleneterephthalate (PET)
Phosphor layer	115	3.3	phosphor*:urethane = 25:1 (3.18 g/cc phosphor) *$BaFBr_{0.85}I_{0.15}$ density 5.2 g/cm^3
Surface layer	9	1.37	polyethyleneterephthalate (PET)

---

[i] M. Thoms, Nucl. Instrum. Methods Phys. Res. A **378**, 598-611 (1996)

[ii] Webelements.com

	Layer	Weight (g/m^2)	Depth (microns)	BaFBrI	Phosphor Density	Barium Weight (%)
BAS-III	Back	27.3	28			
	Base	443.9	319			
	Undercoat	25.2	20			
	Phosphor	445.6	139	$BaFBr_{0.85}I_{0.15}$	3.05	26
	Protective Coat	16.3	11			
	Total	958.3	517			
BAS-IIIS	Back	671.5	290			
	Base	443.9	319			
	Undercoat	25.2	20			
	Phosphor	445.6	139	$BaFBr_{0.85}I_{0.15}$	3.05	26
	Protective Coat	16.3	11			
	Total	1602.5	779			
BAS-MP 2040	Back	27.3	28			
	Base	443.9	319			
	Undercoat	18.5	12			
	Phosphor	573.5	178	$BaFBr_{0.85}I_{0.15}$	3.07	31
	Protective Coat	16.3	11			
	Total	1079.5	548			

	Layer	Weight (g/m^2)	Depth (microns)	BaFBrI	Phosphor Density	Barium Weight (%)
BAS-MP 2040 S	Back	671.5	290			
	Base	443.9	319			
	Undercoat	18.5	12			
	Phosphor	573.5	178	$BaFBr_{0.85}I_{0.15}$	3.07	19
	Protective Coat	16.3	11			
	Total	1723.7	810			
BAS-SR 2040	Back	443.7	160			
	Base	266.7	190			
	Undercoat	18.5	12			
	Phosphor	389.8	121	$BaFBr_{0.85}I_{0.15}$	3.07	20
	Protective Coat	10.4	7			
	Total	1129.1	490			
BAS-TR 2040	Back					
	Base	346.6	247			
	Undercoat	13.9	11			
	Phosphor	142.6	52	$BaFBr_{0.85}I_{0.15}$	2.61	16
	Protective Coat					
	Total	503.1	310			

	Layer	Weight (g/m^2)	Depth (microns)	BaFBrI	Phosphor Density	Barium Weight (%)
BAS-TR 2040S	Back	671.5	290			
	Base	346.6	247			
	Undercoat	13.9	11			
	Phosphor	142.6	52	$BaFBr_{0.85}I_{0.15}$	2.61	7
	Protective Coat					
	Total	1174.6	600			
BAS-MS 2040	Back	443.7	120			
	Base	266.7	202			
	Undercoat	16.5	12			
	Phosphor	380.3	115	$BaFBr_{0.85}I_{0.15}$	3.18	19
	Protective Coat	14.8	9			
	Total	1122	486			

Bibliography

[1] G. Malka and JL Miquel. Experimental confirmation of ponderomotive-force electrons produced by an ultrarelativistic laser pulse on a solid target. *Physical Review Letters*, 77(1):75–78, 1996.

[2] F. N. Beg, A. R. Bell, A. E. Dangor, C. N. Danson, A. P. Fews, M. E. Glinsky, B. A. Hammel, P. Lee, P. A. Norreys, and M. Tatarakis. A study of picosecond laser–solid interactions up to 10^{19} w/cm^2. *Physics of Plasmas*, 4(2):447–457, 1997.

[3] M. A. Stoyer, T. C. Sangster, E. A. Henry, M. D. Cable, T. E. Cowan, S. P. Hatchett, M.H. Key, M. J. Moran, D. M. Pennington, M. D. Perry, T. W. Phillips, M. S. Singh, R. A. Snavely, M. Tabak, and S. C. Wilks. Nuclear diagnostics for petawatt experiments (invited). *Review of Scientific Instruments*, 72(1):767–772, 2001.

[4] K. Yasuike, M. H. Key, S. P. Hatchett, R. A. Snavely, and K. B. Wharton. Hot electron diagnostic in a solid laser target by k-shell lines measurement from ultraintense laser–plasma interactions (3 x 10^{20} w/cm^2,$\leq$ 400 j). *Review of Scientific Instruments*, 72(1):1236–1240, 2001.

[5] P. M. Nilson, W. Theobald, J. Myatt, C. Stoeckl, M. Storm, O. V. Gotchev, J. D. Zuegel, R. Betti, D. D. Meyerhofer, and T. C. Sangster. High-intensity laser-plasma interactions in the refluxing limit. *Physics of Plasmas*, 15(5):056308, 2008.

[6] A. G. MacPhee, K. U. Akli, F. N. Beg, C. D. Chen, H. Chen, R. Clarke, D. S. Hey, R. R. Freeman, A. J. Kemp, M. H. Key, J. A. King, S. Le Pape, A. Link, T. Y. Ma, H. Nakamura, D. T. Offermann, V. M. Ovchinnikov, P. K. Patel, T. W. Phillips, R. B. Stephens, R. Town, Y. Y. Tsui, M. S. Wei, L. D. Van Woerkom, and A. J. Mackinnon. Diagnostics for fast ignition science (invited). *Review of Scientific Instruments*, 79(10):10F302, 2008.

[7] B. R. Maddox, H. S. Park, B. A. Remington, and M. McKernan. Calibration and characterization of single photon counting cameras for short-pulse laser experiments. *Review of Scientific Instruments*, 79(10):10E924, 2008.

[8] B. Chrisman, Y. Sentoku, and A. J. Kemp. Intensity scaling of hot electron energy coupling in cone-guided fast ignition. *Physics of Plasmas*, 15(5):056309, 2008.

[9] G. Gamow. Zur quantentheorie des atomkerns. *Zeitschrift fuer Physik*, 51:204–212, 1928.

[10] A.A. Harms, K.F. Schoepf, G.H. Miley, and D.R. Kingdon. *Principles of Fusion Energy.* World Scientific, 2000.

[11] J.R. McNally Jr., K.E. Rothe, and R.D. Sharp. Fusion reactivity graphs and tables for charge and particle reactions, ornl/tm-6914. Technical report, Oak Ridge National Laboratory, 1979.

[12] J D Lawson. Some criteria for a power producing thermonuclear reactor. *Proceedings of the Physical Society. Section B*, 70(1):6–10, 1957.

[13] S. Atzeni and J. Meyer ter vehn. *The Physics of Inertial Fusion.* Oxford University Press Inc., New York, 2004.

[14] J. Nuckolls, L. Wood, A. Thiessen, and G. Zimmerman. Laser compression of matter to super-high densities: Thermonuclear (ctr) applications. *Nature*, 239:139 - 142, 1972.

[15] C. BIbeau, P.J. Wegner, E.I . Moses, and B.E. Warner. Generating powerful ultraviolet beams with the worlds largest laser. *Laser Focus World*, 42:113–117, 2006.

[16] Max Tabak, James Hammer, Michael E. Glinsky, William L. Kruer, Scott C. Wilks, John Woodworth, E. Michael Campbell, Michael D. Perry, and Rodney J. Mason. Ignition and high gain with ultrapowerful lasers. *Physics of Plasmas*, 1(5):1626–1634, 1994.

[17] D Strickland and G Mourou. Compression of amplified chirped optical pulses. *Optics Communications*, 55(6):447–449, 1985.

[18] Stephen P. Hatchett and Max Tabak. Cone focus geometry for fast ignition. 2000.

[19] R. Kodama, P. A. Norreys, K. Mima, A. E. Dangor, R. G. Evans, H. Fujita, Y. Kitagawa, K. Krushelnick, T. Miyakoshi, N. Miyanaga, T. Norimatsu, S. J. Rose, T. Shozaki, K. Shigemori, A. Sunahara, M. Tampo, K. A. Tanaka, Y. Toyama, T. Yamanaka, and M. Zepf. Fast heating of ultrahigh-density plasma as a step towards laser fusion ignition. *Nature*, 412(6849):798–802, August 2001.

[20] R. Kodama, H. Shiraga, K. Shigemori, Y. Toyama, S. Fujioka, H. Azechi, H. Fujita, H. Habara, T. Hall, Y. Izawa, T. Jitsuno, Y. Kitagawa, K. M. Krushelnick, K. L. Lancaster, K. Mima, K. Nagai, M. Nakai, H. Nishimura,

T. Norimatsu, P. A. Norreys, S. Sakabe, K. A. Tanaka, A. Youssef, M. Zepf, and T. Yamanaka. Nuclear fusion: Fast heating scalable to laser fusion ignition. *Nature*, 418(6901):933–934, August 2002.

[21] M. Roth, T. E. Cowan, M. H. Key, S. P. Hatchett, C. Brown, W. Fountain, J. Johnson, D. M. Pennington, R. A. Snavely, S. C. Wilks, K. Yasuike, H. Ruhl, F. Pegoraro, S. V. Bulanov, E. M. Campbell, M. D. Perry, and H. Powell. Fast ignition by intense laser-accelerated proton beams. *Phys. Rev. Lett.*, 86(3):436–439, Jan 2001.

[22] Stefano Atzeni, Angelo Schiavi, and Claudio Bellei. Targets for direct-drive fast ignition at total laser energy of 200–400 kj. *Physics of Plasmas*, 14(5):052702, 2007.

[23] S. C. Wilks, W. L. Kruer, M. Tabak, and A. B. Langdon. Absorption of ultra-intense laser pulses. *Phys. Rev. Lett.*, 69(9):1383–1386, Aug 1992.

[24] A. J. Kemp, Y. Sentoku, and M. Tabak. Hot-electron energy coupling in ultraintense laser-matter interaction. *Physical Review Letters*, 101(7):075004, 2008.

[25] M. G. Haines, M. S. Wei, F. N. Beg, and R. B. Stephens. Hot-electron temperature and laser-light absorption in fast ignition. *Physical Review Letters*, 102(4):045008, 2009.

[26] A. P. L. Robinson and M. Sherlock. Magnetic collimation of fast electrons produced by ultraintense laser irradiation by structuring the target composition. *Physics of Plasmas*, 14(8):083105, 2007.

[27] A. P. L. Robinson, M. Sherlock, and P. A. Norreys. Artificial collimation of fast-electron beams with two laser pulses. *Physical Review Letters*, 100(2):025002, 2008.

[28] S. Kar, A. P. L. Robinson, D. C Carroll, O Lundh, K. Markey, P. McKenna, P. Norreys, and M. Zepf. Guiding of relativistic electron beams in solid targets by resistively controlled magnetic fields. *Physical Review Letters*, 102(5):055001, 2009.

[29] C. Deutsch, H. Furukawa, K. Mima, M. Murakami, and K. Nishihara. Interaction physics of the fast ignitor concept. *Phys. Rev. Lett.*, 77(12):2483–2486, Sep 1996.

[30] C. K. Li and R. D. Petrasso. Stopping of directed energetic electrons in high-temperature hydrogenic plasmas. *Phys. Rev. E*, 70(6):067401, Dec 2004.

[31] A. A. Solodov and R. Betti. Stopping power and range of energetic electrons in dense plasmas of fast-ignition fusion targets. *Physics of Plasmas*, 15(4):042707, 2008.

[32] Jerry A Britten John A Caird Rick Cross Chris A Ebbers Mark J Eckart Al C Erlandson William A Molander Andrew Ng Prav K Patel Dwight F Pierce Brent C Stuart, Jim D Bonlie. The titan laser at llnl. 2006.

[33] J.A. Halbleib, R.P. Kensek, G.D. Valdez, S.M. Seltzer, and M.J. Berger. Its: the integrated tiger series of electron/photon transport codes-version 3.0. *Nuclear Science, IEEE Transactions on*, 39(4):1025–1030, Aug 1992.

[34] S.C. Wilks and W.L. Kruer. Absorption of ultrashort, ultra-intense laser light by solids and overdense plasmas. *Quantum Electronics, IEEE Journal of*, 33(11):1954–1968, Nov 1997.

[35] William Kruer. *The Physics of Laser Plasma Interactions.* Westview Press, 2001.

[36] P. A. Norreys, M. Santala, E. Clark, M. Zepf, I. Watts, F. N. Beg, K. Krushelnick, M. Tatarakis, A. E. Dangor, X. Fang, P. Graham, T. McCanny, R. P. Singhal, K. W. D. Ledingham, A. Creswell, D. C. W. Sanderson, J. Magill, A. Machacek, J. S. Wark, R. Allott, B. Kennedy, and D. Neely. Observation of a highly directional gamma-ray beam from ultrashort, ultraintense laser pulse interactions with solids. volume 6, pages 2150–2156. AIP, 1999.

[37] A.J. Kemp, Y. Sentoku, and M. Tabak. Hot electron energy coupling in ultra-intense laser matter interaction. *submitted to Phys. Rev. E*, 2009.

[38] J. Meyer ter Vehn. *Atoms, Solids, and Plasmas in Super-Intense Laser Fields, Proceedings of the 30th Course of the International School of Quantum Electronics.* Kluwer Academic/Plenum Publishers, New York, 2001.

[39] C. I. Moore, J. P. Knauer, and D. D. Meyerhofer. Observation of the transition from thomson to compton scattering in multiphoton interactions with low-energy electrons. *Phys. Rev. Lett.*, 74(13):2439–2442, Mar 1995.

[40] M. J. Berger and S. M. Seltzer. Etran monte carlo code system for electron and photon transport through extended media. Technical Report CCC-107, Radiation Shielding Information Center, Computer Code Collection, Oak Ridge National Laboratory, 1968.

[41] Stephen M. Seltzer. Electron-photon monte carlo calculations: The etran code. *International Journal of Radiation Applications and Instrumentation. Part A. Applied Radiation and Isotopes*, 42(10):917 – 941, 1991.

[42] ICRU. Stopping powers for electrons and positrons. Technical Report 37, International Commission on Radiation Units and Measurements, Bethesda, MD, 1984.

[43] H. A. Bethe. Theory of passage of swift corpuscular rays through matter. *Ann. Physik*, 5:325, 1930.

[44] H. A. Bethe. Scattering of electrons. *Z. fur Physik*, 76:293, 1932.

[45] F. Rohrlich and B. C. Carlson. Positron-electron differences in energy loss and multiple scattering. *Phys. Rev.*, 93(1):38–44, Jan 1954.

[46] Hans A. Bethe and Roman W. Jackiw. *Intermediate Quantum Mechanics.* W.A. Benjamin, Inc., 1973.

[47] J.J. Sakurai. *Modern Quantum Mechanics.* Cummings Publishing Company, Inc., 1985.

[48] C. Møller. Passage of hard beta rays through matter. *Ann. Physik (Leipzig)*, 14:531, 1932.

[49] R. M. Sternheimer, S. M. Seltzer, and M. J. Berger. Density effect for the ionization loss of charged particles in various substances. *Phys. Rev. B*, 26(11):6067–6076, Dec 1982.

[50] John David Jackson. *Classical Electrodynamics, 2nd Edition.* John Wiley & Sons, Inc., 1975.

[51] H.A. Bethe and W. Heitler. On the stopping of fast particles and on the creation of positive electrons. *Proc. Roy. Soc. (London)*, A146:83, 1934.

[52] H. W. KOCH and J. W. MOTZ. Bremsstrahlung cross-section formulas and related data. *Rev. Mod. Phys.*, 31(4):920–955, Oct 1959.

[53] H. K. Tseng and R. H. Pratt. Exact screened calculations of atomic-field bremsstrahlung. *Phys. Rev. A*, 3(1):100–115, Jan 1971.

[54] R. H. Pratt, H. K. Tseng, C. M. Lee, Lynn Kissel, Crawford MacCallum, and Merle Riley. Bremsstrahlung energy spectra from electrons of kinetic energy 1 kev $\leq$ t1 $\leq$ 2000 kev incident on neutral atoms 2 $\leq$ z $\leq$ 92. *Atomic Data and Nuclear Data Tables*, 20(2):175 - 209, 1977.

[55] R. H. Pratt, H. K. Tseng, C. M. Lee, C. MacCALLUM, and M. RILEY. Bremsstrahlung energy spectra from electrons of kinetic energy 1 kev $\leq$ t1 $\leq$ 2000 kev incident on neutral atoms 2 $\leq$ z $\leq$ 92. *Atomic Data and Nuclear Data Tables*, 26(5):477 - 481, 1981.

[56] Handel Davies, H. A. Bethe, and L. C. Maximon. Theory of bremsstrahlung and pair production. ii. integral cross section for pair production. *Phys. Rev.*, 93(4):788–795, Feb 1954.

[57] Haakon Olsen. Outgoing and ingoing waves in final states and bremsstrahlung. *Phys. Rev.*, 99(4):1335–1336, Aug 1955.

[58] E. Haug. Bremsstrahlung and pair production in the field of free electrons. *Z. Naturforsch*, 30a:1099, 1975.

[59] Stephen M. Seltzer and Martin J. Berger. Bremsstrahlung energy spectra from electrons with kinetic energy 1 kev-10 gev incident on screened nuclei and orbital electrons of neutral atoms with z = 1-100. *Atomic Data and Nuclear Data Tables*, 35(3):345 – 418, 1986.

[60] S.T. Perkins, D.E. Cullen, M.H. Chen, J.H. Hubbell, J. Rathkopf, and J. Scofield. Tables and graphs of atomic subshell and relaxation data derived from the llnl evaluated atomic data library (eadl), z=1-100, ucrl-50400. Technical report, Lawrence Livermore National Laboratory, 1991.

[61] R.D. Evans. *The Atomic Nucleus.* Robert E. Krieger Publishing Company, 1955.

[62] H.-K. Chung, M.H. Chen, W.L. Morgan, Y. Ralchenko, and R.W. Lee. Flychk: Generalized population kinetics and spectral model for rapid spectroscopic analysis for all elements. *High Energy Density Physics*, 1(1):3 – 12, 2005.

[63] H. Kolbenstvedt. Simple theory for k-ionization by relativistic electrons. *Journal of Applied Physics*, 38(12):4785–4787, 1967.

[64] W. Bambynek. A new evaluation of k-shell fluorescence yields. In *Post-Deadline Abstracts of X84: X-Ray and Inner-Shell Processes in Atoms, Moledules and Solids, p. 1, 20-24 August, Leipzig*, 1984.

[65] H. Deutsch, K. Becker, S. Matt, and T.D. Mark. Theoretical determination of absolute electron-impact ionization cross sections of molecules. *International Journal of Mass Spectrometry*, 197:3769, 2000.

[66] H. Deutsch, K. Becker, B. Gstir, and T.D. Mark. Calculated electron impact cross sections for the k-shell ionization of fe, co, mn, ti, zn, nb, and mo atoms using the dm formalism. *International Journal of Mass Spectrometry*, 213:5–8, 2002.

[67] H. Deutsch, P. Scheier, K. Becker, and T.D. Mrk. Revised high energy behavior of the deutsch-mrk (dm) formula for the calculation of electron impact ionization cross sections of atoms. *International Journal of Mass Spectrometry*, 233:1317, 2004.

[68] O. Klein and Y. Nishina. *Z. Physik*, 52:853, 1929.

[69] K. A. Tanaka, R. Kodama, H. Fujita, M. Heya, N. Izumi, Y. Kato, Y. Kitagawa, K. Mima, N. Miyanaga, T. Norimatsu, A. Pukhov, A. Sunahara, K. Takahashi, M. Allen, H. Habara, T. Iwatani, T. Matusita, T. Miyakosi, M. Mori, H. Setoguchi, T. Sonomoto, M. Tanpo, S. Tohyama, H. Azuma, T. Kawasaki, T. Komeno, O. Maekawa, S. Matsuo, T. Shozaki, Ka Suzuki, H. Yoshida, T. Yamanaka, Y. Sentoku, F. Weber, Jr. T. W. Barbee, and L. DaSilva. Studies of ultra-intense laser plasma interactions for fast ignition. *Physics of Plasmas*, 7(5):2014–2022, 2000.

[70] Stephen P. Hatchett, Curtis G. Brown, Thomas E. Cowan, Eugene A. Henry, Joy S. Johnson, Michael H. Key, Jeffrey A. Koch, A. Bruce Langdon, Barbara F. Lasinski, Richard W. Lee, Andrew J. Mackinnon, Deanna M. Pennington, Michael D. Perry, Thomas W. Phillips, Markus Roth, T. Craig Sangster, Mike S. Singh, Richard A. Snavely, Mark A. Stoyer, Scott C. Wilks, and Kazuhito Yasuike. Electron, photon, and ion beams from the relativistic interaction of petawatt laser pulses with solid targets. volume 7, pages 2076–2082. AIP, 2000.

[71] KB Wharton, SP Hatchett, SC Wilks, MH Key, JD Moody, V. Yanovsky, AA Offenberger, BA Hammel, MD Perry, and C. Joshi. Experimental measurements of hot electrons generated by ultraintense ($> 10^{19}$ w/cm^2) laser-plasma interactions on solid-density targets. *Physical Review Letters*, 81(4):822–825, 1998.

[72] M. Storm, I. A. Begishev, R. J. Brown, C. Guo, D. D. Meyerhofer, C. Mileham, J. F. Myatt, P. M. Nilson, T. C. Sangster, C. Stoeckl, W. Theobald, and J. D. Zuegel. A high-resolution coherent transition radiation diagnostic for laser-produced electron transport studies (invited). *Review of Scientific Instruments*, 79(10):10F503, 2008.

[73] W. Theobald, K. Akli, R. Clarke, J. A. Delettrez, R. R. Freeman, S. Glenzer, J. Green, G. Gregori, R. Heathcote, N. Izumi, J. A. King, J. A. Koch, J. Kuba, K. Lancaster, A. J. MacKinnon, M. Key, C. Mileham, J. Myatt, D. Neely, P. A. Norreys, H.-S. Park, J. Pasley, P. Patel, S. P. Regan, H. Sawada, R. Shepherd, R. Snavely, R. B. Stephens, C. Stoeckl, M. Storm, B. Zhang, and T. C. Sangster. Hot surface ionic line emission and cold k-inner shell emission from petawatt-laser-irradiated cu foil targets. *Physics of Plasmas*, 13(4):043102, 2006.

[74] J. Myatt, W. Theobald, J. A. Delettrez, C. Stoeckl, M. Storm, T. C. Sangster, A. V. Maximov, and R. W. Short. High-intensity laser interactions with mass-limited solid targets and implications for fast-ignition experiments on omega ep. *Physics of Plasmas*, 14(5):056301, 2007.

[75] A.Peter Fews and Denis L. Henshaw. High resolution alpha particle spectroscopy using cr-39 plastic track detector. *Nuclear Instruments and Methods in Physics Research*, 197(2-3):517 – 529, 1982.

[76] T. W. Phillips, M. D. Cable, D. G. Hicks, C. K. Li, R. D. Petrasso, and F. H. Seguin. A study of cr-39 track response to charged particles from nova implosions. *Review of Scientific Instruments*, 68(1):596–598, 1997.

[77] T. H. Tan, G. H. McCall, and A. H. Williams. Determination of laser intensity and hot-electron temperature from fastest ion velocity measurement on laser-produced plasma. *Physics of Fluids*, 27(1):296–301, 1984.

[78] M. H. Key, M. D. Cable, T. E. Cowan, K. G. Estabrook, B. A. Hammel, S. P. Hatchett, E. A. Henry, D. E. Hinkel, J. D. Kilkenny, J. A. Koch, W. L. Kruer, A. B. Langdon, B. F. Lasinski, R. W. Lee, B. J. MacGowan, A. MacKinnon, J. D. Moody, M. J. Moran, A. A. Offenberger, D. M. Pennington, M. D. Perry, T. J. Phillips, T. C. Sangster, M. S. Singh, M. A. Stoyer, M. Tabak, G. L. Tietbohl, M. Tsukamoto, K. Wharton, and S. C. Wilks. Hot electron production and heating by hot electrons in fast ignitor research. *Physics of Plasmas*, 5(5):1966–1972, 1998.

[79] J. R. Davies. How wrong is collisional monte carlo modeling of fast electron transport in high-intensity laser-solid interactions? *Phys. Rev. E*, 65(2):026407, Jan 2002.

[80] R. A. Snavely, M. H. Key, S. P. Hatchett, T. E. Cowan, M. Roth, T. W. Phillips, M. A. Stoyer, E. A. Henry, T. C. Sangster, M. S. Singh, S. C. Wilks, A. MacKinnon, A. Offenberger, D. M. Pennington, K. Yasuike, A. B. Langdon, B. F. Lasinski, J. Johnson, M. D. Perry, and E. M. Campbell. Intense high-energy proton beams from petawatt-laser irradiation of solids. *Phys. Rev. Lett.*, 85(14):2945–2948, Oct 2000.

[81] P.m. nilson, private communication, march 2009.

[82] R. Baumgartner and R. Byer. Optical parametric amplification. *Quantum Electronics, IEEE Journal of*, 15(6):432–444, Jun 1979.

[83] G. Cheriaux, P. Rousseau, F. Salin, J. P. Chambaret, Barry Walker, and L. F. Dimauro. Aberration-free stretcher design for ultrashort-pulse amplification. *Opt. Lett.*, 21(6):414–416, 1996.

[84] S. Le Pape. manuscript in preparation.

[85] Kenji Takahashi. Progress in science and technology on photostimulable bafx:eu2+ (x=cl, br, i) and imaging plates. *Journal of Luminescence*, 100(1-4):307 - 315, 2002.

[86] C. D. Chen, J. A. King, M. H. Key, K. U. Akli, F. N. Beg, H. Chen, R. R. Freeman, A. Link, A. J. Mackinnon, A. G. MacPhee, P. K. Patel, M. Porkolab, R. B. Stephens, and L. D. Van Woerkom. A bremsstrahlung spectrometer using k-edge and differential filters with image plate dosimeters. *Review of Scientific Instruments*, 79(10):10E305, 2008.

[87] R. Nolte, R. Behrens, M. Schnrer, A. Rousse, and P. Ambrosi. A tld-based few-channel spectrometer for x ray fields with high fluence rates. *Radiat Prot Dosimetry*, 84(1-4):367–370, 1999.

[88] Junji Miyahara, Kenji Takahashi, Yoshiyuki Amemiya, Nobuo Kamiya, and Yoshinori Satow. A new type of x-ray area detector utilizing laser stimulated luminescence. *Nuclear Instruments and Methods in Physics Research Section*

A: Accelerators, Spectrometers, Detectors and Associated Equipment, 246(1-3):572 – 578, 1986.

[89] M. Thoms. The quantum efficiency of radiographic imaging with image plates. *Nuclear Instruments and Methods in Physics Research Section A: Accelerators, Spectrometers, Detectors and Associated Equipment*, 378(3):598 – 611, 1996.

[90] C. Stoeckl, W. Theobald, T. C. Sangster, M. H. Key, P. Patel, B. B. Zhang, R. Clarke, S. Karsch, and P. Norreys. Operation of a single-photon–counting x-ray charge-coupled device camera spectrometer in a petawatt environment. *Review of Scientific Instruments*, 75(10):3705–3707, 2004.

[91] H.-S. Park, D. M. Chambers, H.-K. Chung, R. J. Clarke, R. Eagleton, E. Giraldez, T. Goldsack, R. Heathcote, N. Izumi, M. H. Key, J. A. King, J. A. Koch, O. L. Landen, A. Nikroo, P. K. Patel, D. F. Price, B. A. Remington, H. F. Robey, R. A. Snavely, D. A. Steinman, R. B. Stephens, C. Stoeckl, M. Storm, M. Tabak, W. Theobald, R. P. J. Town, J. E. Wickersham, and B. B. Zhang. High-energy k alpha radiography using high-intensity, short-pulse lasers. *Physics of Plasmas*, 13(5):056309, 2006.

[92] M.D. Abramoff, P.J. Magelhaes, and S.J. Ram. Image processing with imagej. *Biophotonics International*, 11(7):36–42, 2004.

[93] K. U. Akli, S. B. Hansen, A. J. Kemp, R. R. Freeman, F. N. Beg, D. C. Clark, S. D. Chen, D. Hey, S. P. Hatchett, K. Highbarger, E. Giraldez, J. S. Green, G. Gregori, K. L. Lancaster, T. Ma, A. J. MacKinnon, P. Norreys, N. Patel, J. Pasley, C. Shearer, R. B. Stephens, C. Stoeckl, M. Storm, W. Theobald, L. D. Van Woerkom, R. Weber, and M. H. Key. Laser heating of solid matter by light-pressure-driven shocks at ultrarelativistic intensities. *Physical Review Letters*, 100(16):165002, 2008.

[94] M. I. K. Santala, M. Zepf, I. Watts, F. N. Beg, E. Clark, M. Tatarakis, K. Krushelnick, A. E. Dangor, T. McCanny, I. Spencer, R. P. Singhal, K. W. D. Ledingham, S. C. Wilks, A. C. Machacek, J. S. Wark, R. Allott, R. J. Clarke, and P. A. Norreys. Effect of the plasma density scale length on the direction of fast electrons in relativistic laser-solid interactions. *Phys. Rev. Lett.*, 84(7):1459–1462, Feb 2000.

[95] R. B. Stephens, R. A. Snavely, Y. Aglitskiy, F. Amiranoff, C. Andersen, D. Batani, S. D. Baton, T. Cowan, R. R. Freeman, T. Hall, S. P. Hatchett, J. M. Hill, M. H. Key, J. A. King, J. A. Koch, M. Koenig, A. J. MacKinnon, K. L. Lancaster, E. Martinolli, P. Norreys, E. Perelli-Cippo, M. Rabec Le Gloahec, C. Rousseaux, J. J. Santos, and F. Scianitti. $k\alpha$ fluorescence measurement of relativistic electron transport in the context of fast ignition. *Phys. Rev. E*, 69(6):066414, Jun 2004.

[96] J J Honrubia and J Meyer ter Vehn. Fast ignition of fusion targets by laser-driven electrons. *Plasma Physics and Controlled Fusion*, 51(1):014008 (12pp), 2009.

[97] Adolfo Esposito and Maitreyee Nandy. Measurement and unfolding of neutron spectra using bonner spheres. *Radiat Prot Dosimetry*, 110(1-4):555–558, 2004.

[98] H Schwoerer, P Gibbon, S Dusterer, R Behrens, C Ziener, C Reich, and R Sauerbrey. Mev x rays and photoneutrons from femtosecond laser-produced plasmas. *Phys. Rev. Lett.*, 86(11):2317–2320, MAR 12 2001.

[99] A R Bell, J R Davies, S Guerin, and H Ruhl. Fast-electron transport in high-intensity short-pulse laser - solid experiments. *Plasma Physics and Controlled Fusion*, 39(5):653–659, 1997.

[100] B. F. J. Schonland. The passage of cathode rays through matter. *Proc. Roy. Soc. Lond.*, 108:187–210, 1925.

[101] R. W. Varder. *Phil. Mag.*, 29:725, 1915.

[102] D.R. Welch, D.V. Rose, R.E. Clark, T.C. Genoni, and T.P. Hughes. Implementation of an non-iterative implicit electromagnetic field solver for dense plasma simulation. *Computer Physics Communications*, 164:183188, 2004.

[103] D. R. Welch, D. V. Rose, M. E. Cuneo, R. B. Campbell, and T. A. Mehlhorn. Integrated simulation of the generation and transport of proton beams from laser-target interaction. *Physics of Plasmas*, 13:063105, 2006.

[104] private communication, dave larson, lawrence livermore national laboratory (2009).

[105] Hui Chen, Anthony J. Link, Roger van Maren, Pravesh K. Patel, Ronnie Shepherd, Scott C. Wilks, and Peter Beiersdorfer. High performance compact magnetic spectrometers for energetic ion and electron measurement in ultraintense short pulse laser solid interactions. *Review of Scientific Instruments*, 79(10):10E533, 2008.